To the Graduate Council:

I am submitting herewith a thesis written by Ronald Bryce Gray III entitled "The Effects of Gamma Radiation on JFET and Bipolar Transistors with Application to the SSC." I have examined the final copy of this thesis for form and content and recommend that it be accepted in partial fulfillment of the requirements for the degree of Master of Engineering, with a major in Electrical Engineering.

E. J. Kennedy

E. J. Kennedy, Major Professor

We have read this thesis and recommend its acceptance:

T. Vaughn Blalock

J. M. Rochelle

Accepted for the Council:

Lew Minkel

Vice Provost
and Dean of The Graduate School

THE EFFECTS OF GAMMA RADIATION ON JFET AND BIPOLAR TRANSISTORS WITH APPLICATION TO THE SSC

A Thesis

Presented for the

Master of Engineering

Degree

The University of Tennessee, Knoxville

Ronald Bryce Gray III

December 1990

ACKNOWLEDGMENTS

I am grateful to those who made this thesis possible. First, I express my conviction that without a personal relationship with the Lord Jesus Christ, my efforts would have no meaning. I also thank the many secretaries and engineers in the Instrumentation and Controls Division at Oak Ridge National Laboratory who were very giving of their time. Special acknowledgement goes to Dr. T. V. Blalock, Charles Britton, Jr., Nance Ericson, Dr. E. J. Kennedy, and Dr. J. M. Rochelle, whose knowledge and efforts were a major contribution to this thesis. I also express my gratitude to family and friends who have been a mainstream of encouragement throughout my life.

This research was performed at Oak Ridge National Laboratory, operated for the U. S. Department of Energy under contract DE-AC05-84OR21400 with Martin Marietta Energy Systems, Inc.

ABSTRACT

Design of a low-noise, low-power, high-speed, and radiation-hardened charge sensitive preamplifier for the Superconducting Super Collider (SSC) has prompted an investigation of front-end devices. Several state-of-the-art JFET and bipolar transistors along with devices from a semi-custom analog integrated circuit process were characterized in both a normal and low-current operation region. In these regions the JFETs were characterized for noise, ac, and dc parameters before and after exposure to gamma radiation. The bipolar devices were characterized for ac and dc parameters before and after exposure to gamma radiation. Analysis of the transistors and data from these regions are presented along with a highlight of radiation effects on these devices. Also presented is the design and implementation of a noise measurement system for JFET devices.

TABLE OF CONTENTS

CHAPTER PAGE

1. THESIS DEFINITION 1

1.1 Introduction 1

1.2 Thesis Objective and Study 1

1.3 Related Work 2

2. RADIATION EFFECTS ON SI JUNCTIONS 4

2.1 Gamma Radiation Effects 4

2.1.1 Ionization Damage 4

2.1.2 Displacement Damage 6

2.2 Neutron Damage 6

2.3 Radiation Source Used in the Thesis 7

3. JUNCTION FIELD EFFECT TRANSISTORS (JFETs) 8

3.1 Introduction 8

3.2 DC Characteristics 8

3.2.1 Transconductance (g_m) 12

3.2.1.1 Measurement Theory 13

3.2.1.2 Radiation Effects 14

3.2.1.3 Measurement Results 14

3.2.2 Lambda 16

3.2.2.1 Measurement Theory 17

3.2.2.2 Radiation Effects 18

3.2.2.3 Measurement Results 19

3.2.3 NP (Square law relationship) 19

CHAPTER PAGE

3.2.3.1 Measurement Theory 20
3.2.3.2 Radiation Effects 22
3.2.3.3 Measurements 23
3.2.4 VTO, I_{DSS}, and Beta 23
3.2.4.1 Measurement Theory 24
3.2.4.2 Radiation Effects 26
3.2.4.3 Measurements 27
3.2.5 NS 28
3.2.5.1 Measurement Theory 29
3.2.5.2 Radiation Effects 31
3.2.5.3 Measurements 31
3.2.6 IO (threshold current) 32
3.2.6.1 Measurement Theory 33
3.2.6.2 Radiation Effects 35
3.2.6.3 Measurements 35
3.2.7 Gate Leakage Current 35
3.2.7.1 Measurement Theory 37
3.2.7.2 Radiation Effects 38
3.2.7.3 Measurements 38
3.3 Capacitance 40
3.3.1 Radiation Effects 41
3.3.2 Measurement Techniques 42
3.3.3 Measurements 43
3.4 Noise 53

CHAPTER PAGE

3.4.1 Definition 53
3.4.2 Radiation Effects 60
3.4.3 Measurements 61
4. BIPOLAR TRANSISTORS 74
4.1 Introduction 74
4.2 DC Characteristics 74
4.2.1 Beta 77
4.2.1.1 Measurement Theory 82
4.2.1.2 Radiation Effects 82
4.2.1.3 Measurement Results 82
4.2.2 Early Voltage 88
4.2.2.1 Measurement Theory 89
4.2.2.2 Radiation Effects 89
4.2.2.3 Measurement Results 90
4.2.3 Gummel Plots 90
4.2.3.1 Measurement Theory 91
4.2.3.2 Radiation Effects 91
4.2.3.3 Measurement Results 91
4.3 Capacitance 102
4.3.1 Measurement Theory 102
4.3.2 Radiation Effects 104
4.3.3 Measurement Results 104
5. CONCLUSIONS AND SUGGESTIONS FOR FURTHER STUDY 110
5.1 JFET Devices 110

CHAPTER PAGE

5.2 Bipolar Devices 111

5.3 Suggestions for Further Study 111

BIBLIOGRAPHY **114**

APPENDIXES **118**

A. NOISE MEASUREMENT SYSTEM **119**

A.1 Pre-amplifier 120

A.1.1 Characteristics 122

A.1.1.1 DC 126

A.1.1.2 AC 127

A.1.1.3 Noise 131

A.1.1.4 Power Supply Noise 132

A.1.2 Physical Considerations 132

A.2 Gain Stages 137

A.3 Filter System 139

A.4 Data Acquisition 140

A.5 System Overview 140

A.6 PSpice Simulation File 142

B. DEVICES TESTED **147**

VITA **149**

LIST OF TABLES

TABLE **PAGE**

3.1. g_m (S) for I_D = 1mA, V_{DS} = 2.5V 15

3.2. g_m (S) for I_D = 100uA, V_{DS} = 2.5V 15

3.3. g_m (S) for I_D = 10uA, V_{DS} = 2.5V. 16

3.4. Summary of 1/lambda (V) measurements 19

3.5. Summary of NP measurements 23

3.6. Summary of VTO (V) measurements. 27

3.7. Summary of I_{DSS} (mA) measurements. 28

3.8. Summary of NS measurements 32

3.9. Summary of IO (A) measurements. 36

3.10. I_G (A) for I_D = 100uA and V_{DS} = 2.5V 39

3.11. I_G (A) for I_D = 100uA and V_{DS} = 5V. 39

3.12. Summary of noise measurements. 70

3.13. Summary of noise components for I_D = 1mA 71

3.14. Summary of noise components for I_D = 100uA 72

3.15. Summary of noise components for I_D = 10uA. 73

4.1. Summary of Early voltage measurements 90

5.1. Summary of critical JFET parameters. 112

A.1. CC1 values. 134

A.2. CC2 values. 134

A.3. CC3 values. 135

A.4. Set-up for I_D = 1mA. 135

A.5. Set-up for I_D = 100uA. 136

TABLE PAGE

A.6. Set-up for I_D = 10uA 136

A.7. Twin-T filter parameters. 139

B.1. N-channel JFET devices tested. 147

B.2. Bipolar devices tested. 148

LIST OF FIGURES

FIGURE **PAGE**

3.1. JFET small-signal model.....9

3.2. Log (g_m) vs log (I_D).....13

3.3. Measurement of lambda graph.....18

3.4. Measurement of NP graph.....22

3.5. VTO, I_{DSS}, and Beta measurement.....26

3.6. Measurement of NS.....31

3.7. Definition of IO.....34

3.8. Gate current versus drain to source voltage.....38

3.9. Small signal JFET model.....40

3.10. Capacitance of junction vs reverse voltage.....41

3.11. C_{ISS} measurement connections.....42

3.12. C_{RSS} measurement connections.....43

3.13. NJ3600L a) C_{ISS} vs V_R and C_{RSS} vs V_R.....44

3.14. NJ903L a) C_{ISS} vs V_R and C_{RSS} vs V_R.....45

3.15. NJ1800DL a) C_{ISS} vs V_R and C_{RSS} vs V_R.....46

3.16. 2N6451 a) C_{ISS} vs V_R and C_{RSS} vs V_R.....47

3.17. 2SK152A a) C_{ISS} vs V_R and C_{RSS} vs V_R.....48

3.18. 2N4858 a) C_{ISS} vs V_R and C_{RSS} vs V_R.....49

3.19. 2N4416A a) C_{ISS} vs V_R and C_{RSS} vs V_R.....50

3.20. IMF5912 a) C_{ISS} vs V_R and C_{RSS} vs V_R.....51

3.21. 2N5432 a) C_{ISS} vs V_R and C_{RSS} vs V_R.....52

3.22. JFET noise model.....53

FIGURE PAGE

3.23. Thermal and flicker noise components of S_{ID}. 55

3.24. Burst noise component of S_{ID}. 57

3.25. Modified JFET noise model. 58

3.26. Plot of equation 3.55 vs frequency. 59

3.27. NJ3600L R_n vs frequency for I_D equal a) 1mA, b) 100uA, and c) 10uA. 62

3.28. NJ903L R_n vs frequency for I_D equal a) 1mA, b) 100uA, and c) 10uA. 63

3.29. NJ1800DL R_n vs frequency for I_D equal a) 1mA, b) 100uA, and c) 10uA. 64

3.30. 2N6451 R_n vs frequency for I_D equal a) 1mA, b) 100uA, and c) 10uA. 65

3.31. 2SK152A R_n vs frequency for I_D equal a) 1mA, b) 100uA, and c) 10uA. 66

3.32. 2N4858 R_n vs frequency for I_D equal a) 1mA, b) 100uA, and c) 10uA. 67

3.33. 2N4416A R_n vs frequency for I_D equal a) 1mA, b) 100uA, and c) 10uA. 68

3.34. IMF5912 R_n vs frequency for I_D equal a) 1mA, b) 100uA, and c) 10uA. 69

4.1. Gummel model for the bipolar transistor. 74

4.2. Beta vs log (I_C). 78

4.3. Beta vs I_C for a) MPSH10 and b) A401. 83

4.4. Beta vs I_C for a) CA3127 and b) MRF951. 84

FIGURE PAGE

4.5. Beta vs I_C for a) TLN1 and b) T6NW. 85

4.6. Beta vs I_C for a) MPSH81 and b) A441 86

4.7. Beta vs I_C for TVPA35 87

4.8. Early voltage graph. 89

4.9. Gummel curves 92

4.10. Gummel curves for MPSH10, V_{CE} = 2.5V 93

4.11. Gummel curves for A401, V_{CE} = 2.5V 94

4.12. Gummel curves for CA3127, V_{CE} = 3V 95

4.13. Gummel curves for MRF951, V_{CE} = 2.5V. 96

4.14. Gummel curves for TLN1, V_{CE} = 2.5V 97

4.15. Gummel curves for T6NW, V_{CE} = 2.5V 98

4.16. Gummel curves for MPSH81, V_{CE} = 2.5V 99

4.17. Gummel curves for A441, V_{CE} = 2.5V 100

4.18. Gummel curves for TVPA35, V_{CE} = 2.5V 101

4.19. Connections for COB measurement ($V_R \geq 0$). 102

4.20. Connections for CCS measurement ($V_R \geq 0$). 103

4.21. Connections for CEB measurement ($V_R \geq 0$). 103

4.22. TLN1 a) COB vs V_R and b) CCS vs V_R. 105

4.23. TLN1 CEB vs V_R. 106

4.24. T6NW a) COB vs V_R and b) CCS vs V_R. 107

4.25. TVPA35 a) COB vs V_R and b) CCS vs V_R. 108

4.26. TVPA35 CEB vs V_R. 109

A.1. Noise measurement system. 119

A.2. Complete preamplifier schematic. 121

FIGURE PAGE

A.3. Preamplifier system schematic. 123

A.4. Simplified preamplifier schematic..... 128

A.5. Loop transmission versus frequency a) Magnitude b) Phase..... 129

A.6. Noise gain versus frequency..... 130

A.7. Noise resistance (R_n) versus frequency. 133

A.8. K2 Gain stage..... 138

A.9. Noise measurement system gain diagram..... 140

A.10. Error in noise resistance measurement due to signal location..... 142

CHAPTER 1

THESIS DEFINITION

1.1 Introduction

Conflicting requirements for designing a charge-sensitive preamplifier (CSP) for large-device silicon calorimetry in the Superconducting Super Collider (SSC) have prompted a study of front-end devices. The environment of the SSC and the nature of the events to be amplified place serious constraints on the speed, noise, and radiation hardness of the CSP. Also, a power constraint on the preamplifier is introduced by the proposed SSC calorimeter, which is to be composed of thousands of channels. This low-power criteria requires the front end device to be operated in a low-current region (on the order of 100uA) for which there is little data available on the newest devices. The importance of the front-end device is clearly magnified by these requirements.

1.2 Thesis Objective and Study

This thesis will concentrate on the use of JFET and bipolar transistor processes as front end devices. MOSFETs are also suitable, but require an expensive radiation-hardened process, as MOS devices are very sensitive to ionizing radiation. The thesis by Wu [1] investigated some of the radiation properties of standard MOS devices.

State-of-the-art discrete JFET's having different manufacturers, processes, and geometries were used in this study. The dc characteristics were defined in both the subthreshold and quadratic regions of operation. Harris Semiconductor's JFET Level 2 Model of the circuit simulator SLICE which simulates both regions mentioned was chosen for the definition of dc parameters. The reverse bias junction capacitances C_{ISS} and C_{RSS} were measured for a voltage range of 0 to 5V. Also, the series noise resistance due to the drain current of the JFET's was measured from frequencies of 10Hz to 460KHz at drain current levels of 10uA, 100uA, and 1mA. All of these properties were remeasured after the devices were subjected to 5M rad of gamma radiation.

Dc parameters were measured for several discrete bipolar transistors and a bipolar IC process (VTC Incorporated). The bipolar IC process was also characterized for capacitance. All of these properties were remeasured after the devices were subjected to 5Mrad of gamma radiation.

Also discussed are the theory and results of radiation effects on all parameters, the methods of device characterization, the design and implementation of a noise measurement system, and a highlight of those processes that would prove best in the design of a CSP for the SSC.

1.3 Related Work

There is literature relating to most every topic covered in this paper. For example, there have been several studies on both the design and testing

of amplifiers for radiation hardness. Recently, the mentioned VTC bipolar process was used at Oak Ridge National Laboratories in the design of a low-noise, low-power, and radiation hardened CSP [2]. Another example is a JFET-CMOS radiation-tolerant CSP that was presented in the August 1990 edition of the IEEE Journal of Solid State Circuits [3]. Related work has also been presented by E. Gatti [4] in a paper that makes a comparison of the advantages of the use of JFET vs bipolar processes for fast pulse processing. Similar studies to those presented in this paper on radiation effects in JFETs have been performed at Harwell Laboratory [5] where an automated transistor device noise measurement system has been developed. Radiation effects on several different processes have also been investigated by Alice Wu [1] and H. P. Orrick [6]. One area where the literature is scarce, is the specific characterization of state-of-the-art JFETs and the newer IC process that are studied in this thesis. This thesis presents data from the subthreshold region of operation of JFETs which has recently gained more attention due to the increased interest in subthreshold operation of MOS devices [7,8,9,10,11]. There are several other related works that are referenced throughout this paper.

CHAPTER 2

RADIATION EFFECTS ON SI JUNCTIONS

2.1 Gamma Radiation Effects

Gamma rays is a term for the classification of photons (electromagnetic radiation) that have wavelengths ranging from 0.005 to 1.40 Angstroms [12]. The wavelength of the gamma rays defines their energy via the relationship

$$E = h \cdot v$$

where

h = Planck's constant = 6.626×10^{-34} (J·sec)
v = frequency of radiation (1/sec) .

Depending on the energy of the incident gamma rays, they can interact with semiconductor to produce ionization and crystal lattice displacement damage.

2.1.1 Ionization Damage

Ionization damage can occur in the form of photoelectric absorption, Compton scattering, and pair production [13]. Some of the effects of

ionization due to these process occur only with the gamma source present (temporal effects) while others are more permanent. The dominate temporal effect is the generation of photoelectric currents due to the interaction of gamma rays with the valance electrons of the of the semiconductors atoms. Permanent effects appear in the form of ionized atoms which when located in silicon dioxide layers can remain for long periods of time [14].

Photoelectric absorption, for low-energy gamma rays (x rays), is the main form of interaction between the incoming photons from the gamma source and the atoms of the semiconductor. For this process, the incoming photon ejects an electron from one of the inner shells of the involved atom and the photon's energy is completely absorbed, thus it no longer exists. This leaves the atom in an ionized state with a net positive charge. The vacancy left by the collision is soon filled by an upper shell electron which transitions to this empty state and in the process releases energy in the form of a lower energy photon emission. This photon emission is referred to as fluorescence radiation [15].

In Compton scattering the incoming photons impart a portion of their energy to the outer shell elections of the involved atom. This energy transfer shifts the frequency of the photon and can strip off the electron, which is referred to as a recoil electron [13]. The atom is again left in an ionized state. The Compton scattering effect occurs for higher energy photons.

Pair production is a phenomena that occurs if the gamma ray energy is greater than twice the rest-mass of an electron (1.02 MeV) [13]. For this

process the photon is annihilated as it interacts with the atoms nucleus to produce an electron and a positron both having kinetic energy. These particles can ionize neighboring atoms, cause lattice displacements, combine to produce photons, or become part of the conduction band of the semiconductor.

2.1.2 Displacement Damage

Gamma rays can also interact with semiconductors to produce displacement damage. Displacement damage damage is a secondary effect of the ionization processes mentioned [16]. If the electrons that are generated or displaced from the ionization processes have enough energy (on the order of 0.56 Mev), they have the ability to cause displacements in the lattice structure of the semiconductor [17].

2.2 Neutron Damage

Another very important form of radiation damage is induced by heavy particles such as neutrons. Neutrons have a mass 1840 times the rest mass of an electron and also have no charge. They can damage the semiconductor material through lattice displacements, induced ionization, and transmutation of the atoms [15,18]. Most damage is in the form of lattice displacements which are much greater than the displacements caused by a gamma source.

2.3 Radiation Source Used in the Thesis

The devices tested were irradiated using the Gammacell 200 [19] which was located in the Chemistry Department at the University of Tennessee, Knoxville. The Gammacell 200 uses a cobalt 60 source which provides gamma rays with energies of 1.173 MeV and 1.332 MeV [13]. These energy levels make all of the described gamma radiation interactions possible. Also of importance, cobalt 60 provides only gamma and beta (which is blocked) radiation thus all damage to the irradiated devices could be attributed to gamma radiation. No neutron radiation damage was introduced to the devices for this thesis, although neutrons were used in a similar thesis study by Su [20].

CHAPTER 3

JUNCTION FIELD EFFECT TRANSISTORS (JFETs)

3.1 Introduction

Junction field effect transistors (JFETs) are on the whole are less sensitive to ionization damage than bipolar transistors in that they are majority carrier devices [15]. In comparison to MOSFET devices the JFET (unlike the MOSFET) has no gate oxide layer, thus making it the more radiation resistant of the two.

All JFETs were tested for their dc characteristics, capacitance, and noise characteristics.

3.2 DC Characteristics

The dc characteristics of the JFET devices tested were defined mainly in terms of the JFET's modeling parameters as presented in the SLICE simulation manual [21]. The JFET's small-signal characteristics can be modeled as shown in Figure 3.1. The drain current (I_D) as defined in Figure 3.1 can be written as the sum of a quadratic term and a subthreshold term [21]:

$$I_D = I_{QAD} + I_{SUB} . \tag{3.1}$$

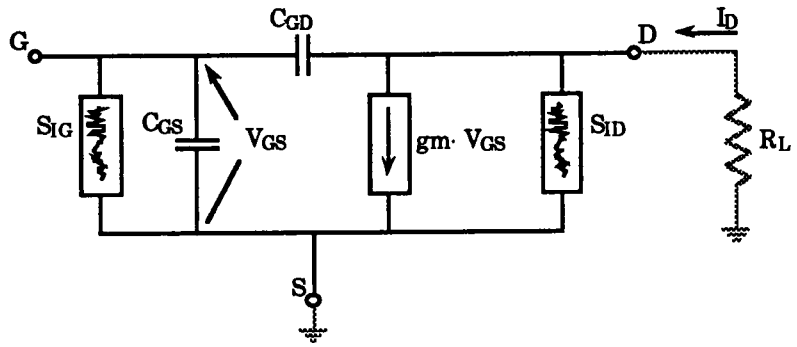


Figure 3.1. JFET small-signal model.

The quadratic term describes the region where I_D is proportional to the square of the gate-to-source voltage (V_{GS}), and is defined as [21]

$$I_{QAD} = \begin{cases} I_{DSS}\left(1 - \frac{V_{GS}}{VTO}\right)^{NP} \left|\tanh\left(\frac{\alpha \cdot V_{DS}}{VTO - V_{GS}}\right)\right| (1 + \lambda \cdot V_{DS}), & |V_{GS}| < |VTO| \\ 0, & \text{elsewhere} \end{cases} \tag{3.2}$$

where:

$$I_{DSS} = Beta\,|VTO|^{NP} \tag{3.3}$$

Beta = Transconductance parameter
VTO = Threshold voltage (Pinch-off voltage)
NP = Power-law characteristic
α = Linear to saturation region transition parameter
V_{DS} = Drain to source voltage
λ = Channel length modulation parameter .

Equation 3.2 is not the classical form for I_D, but is a better representation of the actual data for short channel JFETs because of the included hyperbolic tangent term. This hyperbolic tangent term also provides a more accurate simulation of I_D between the linear and saturation regions then does the classical equations of Shockley [22]. For all the dc measurements that follow, the device will be operated in the saturation region for which the hyperbolic tangent term approaches unity and its effect is negligible. Given this situation equation 3.2 can be simplified to the standard quadratic equation

$$I_{QAD} = \begin{cases} I_{DSS}\left(1 - \frac{V_{GS}}{VTO}\right)^{NP}\left(1 + \lambda \cdot V_{DS}\right), & |V_{GS}| < |VTO| \\ 0, & \text{elsewhere} \end{cases} \tag{3.4}$$

where NP ≈ 2 for most JFETs.

The subthreshold term is defined as [21]

$$I_{SUB} = \begin{cases} \frac{I_{DIF} \cdot I_{LIM}}{I_{DIF} + I_{LIM}}, & |V_{GS}| \geq |VTO| \\ 0, & \text{elsewhere .} \end{cases} \tag{3.5}$$

The form shown in equation 3.5 for the modeling of the subthreshold current was presented in a paper by Sheu [23] which addresses the modeling of short-channel MOS devices. The diffusion current term (I_{DIF}) is defined as [21]

$$I_{DIF} = IO \left\{ \exp\left(\frac{V_{GS} - VTO}{NS \cdot V_T} \right) \left[1 - \exp\left(\frac{-V_{DS}}{V_T} \right) \right] \right\} \tag{3.6}$$

where

IO = Post-pinchoff drain saturation current
NS = Subthreshold exponential shaping parameter
$V_T = \frac{k \cdot T}{q}$ = Thermal voltage
k = Boltzmann's constant = $1.38 \times 10^{-23} \left(\frac{J}{K}\right)$
T = Temperature = 300 (K) = room temperature
q = electron charge = 1.602×10^{-19} (C).

The limit current (I_{LIM}) of equation 3.5 is defined as

$$I_{LIM} = 2 \, Beta \, (V_T)^2. \tag{3.7}$$

Since I_{QAD} in equation 3.2 is equal to zero for $|V_{GS}| \geq |VTO|$, I_{SUB} defines the drain current for both the subthreshold region and the transition region between the subthreshold and quadratic regions. I_{SUB} is by definition dominated by the smaller of the two terms I_{DIF} and I_{LIM}.

I_{DIF} defines subthreshold operation of the JFET and starts to dominate for $|V_{GS}|$ slightly greater than $|VTO|$. As $|V_{GS}|$ increases the effect of I_{LIM} is negligible and I_D is essentially modeled by I_{DIF}. For the region where I_{DIF} dominates, the channel is totally depleted of carriers due to the depletion region produced by the gate to source potential. Any voltage differential between the drain and the source causes a diffusion current to

flow, which is basically independent of V_{DS} for $V_{DS} > V_T$ [10]. Included in equation 3.6 is the parameter NS which controls the shape of the exponential. Although NS theoretically has a value of one it was included for the purpose of verification. I_{LIM} is a constant current that dominates when V_{GS} is close to VTO and makes the transition point V_{GS} = VTO continuous.

The HP4145B Semiconductor Parameter Analyzer was used for all of the dc characterization of the JFETs.

3.2.1 Transconductance (g_m)

The transconductance (g_m) of a JFET is the relationship between the change in drain current relative to the change in gate to source voltage and is expressed as

$$g_m = \frac{\partial I_D}{\partial V_{GS}} . \tag{3.8}$$

From equation 3.4 with $|V_{GS}| < |VTO|$, I_D can be written as

$$I_D = I_{DSS}\left(1 - \frac{V_{GS}}{VTO}\right)^{NP}\left(1 + \lambda \cdot V_{DS}\right) . \tag{3.9}$$

Applying equation 3.8 to equation 3.9 yields

$$g_m = -\frac{NP \cdot I_{DSS}}{VTO}\left(1 - \frac{V_{GS}}{VTO}\right)^{NP-1}\left(1 + \lambda \cdot V_{DS}\right) . \tag{3.10}$$

3.2.1.1 Measurement Theory

The semiconductor parameter analyzer is a really excellent tool for evaluating device models. It provides a function that calculates the change in a measured parameter which was used to measure the dc value of g_m. The transconductance in terms of this function and equation 3.8 can be expressed as

$$g_m = \frac{\Delta I_D}{\Delta V_{GS}}. \tag{3.11}$$

A typical curve for the log (g_m) versus the log (I_D) is shown in Figure 3.2 where VTO is the threshold (pinch-off) voltage.

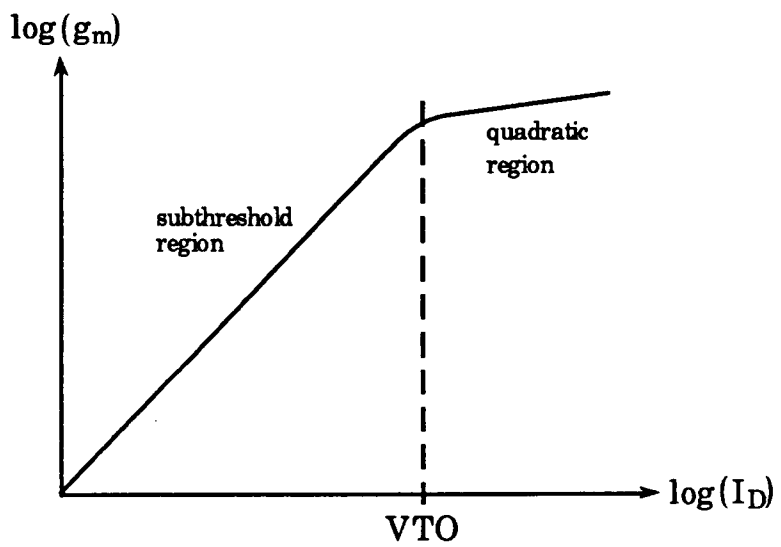


Figure 3.2. Log (g_m) vs log (I_D).

3.2.1.2 Radiation Effects

The transconductance of a JFET will indicate the most change if neutron damage occurs, with a resulting decrease in value. This is most likely a result of the reduction in carrier mobility due to crystal lattice damage. Gamma radiation can produce similar damage, but on a much smaller scale. Thus, g_m will shift very little for a true gamma source. It has been observed that g_m remains essentially unchanged after 1M rad from a gamma source [16].

3.2.1.3 Measurement Results

For all the devices tested (except the NJ903L) g_m either had no change or decreased slightly which agrees well with theory. The increase in g_m for the NJ903L device could be accounted for in that there were only two devices tested and a difference in temperature between the times tested may have occurred.

The measurement results for the transconductance are presented in tables 3.1, 3.2, and 3.3, where the value of g_m is in units of mhos, or the more correct unit of Siemens (S). The data is in the form: **average** (maximum, minimum).

Table 3.1. g_m (S) for I_D = 1mA, V_{DS} = 2.5V.

Part	Pre-radiation	Post-radiation	% Difference between Avg.
NJ3600L	**23.2m** (26.3m, 17.1m)	**22.6m** (25.8m, 16.7m)	**-2.59**
NJ903L	**15.0m** (15.2m, 14.8m)	**15.6m** (16.3m, 14.9m)	**4.00**
NJ1800DL	**16.2m** (17.2m, 15.3m)	**16.1m** (17.2m, 15.1m)	**-.617**
2N6451	**9.38m** (9.62m, 9.16m)	**9.28m** (9.50m, 9.07m)	**-1.07**
2SK152A	**7.96m** (8.06m, 7.86m)	**7.92m** (8.04m, 7.75m)	**-.503**
2N4858	**6.69m** (6.92m, 6.45m)	**6.61m** (6.89m, 6.33m)	**-1.20**
2N4416A	**2.50m** (2.54m, 2.43m)	**2.48m** (2.60m, 2.41m)	**-.800**
IMF5912	**3.12m** (3.23m, 3.00m)	**3.09m** (3.20m, 2.90m)	**-.962**
2N5432	**6.88m** (9.21m, 3.96m)	**6.85m** (9.23m, 3.91m)	**-.436**

Table 3.2. g_m (S) for I_D = 100uA, V_{DS} = 2.5V.

Part	Pre-radiation	Post-radiation	% Difference between Avg.
NJ3600L	**3.22m** (3.42m, 2.72m)	**3.15m** (3.39m, 2.74m)	**-2.17**
NJ903L	**2.11m** (2.12m, 2.10m)	**2.16m** (2.20m, 2.12m)	**2.37**
NJ1800DL	**2.00m** (2.09m, 1.91m)	**1.96m** (2.08m, 1.92m)	**-2.00**
2N6451	**2.15m** (2.24m, 2.10m)	**2.13m** (2.17m, 2.07m)	**-.930**
2SK152A	**1.90m** (1.91m, 1.88m)	**1.88m** (1.90m, 1.86m)	**-1.05**
2N4858	**1.72m** (1.79m, 1.65m)	**1.72m** (1.79m, 1.65m)	**0**
2N4416A	**.859m** (.893m, .844m)	**.850m** (.881m, .835m)	**-1.05**
IMF5912	**.726m** (.913m, .521m)	**.725m** (.913m, .521m)	**-.138**
2N5432	**.879m** (1.28m, .458m)	**.876m** (1.28m, .459m)	**-.341**

Table 3.3. g_m (S) for I_D = 10uA, V_{DS} = 2.5V.

Part	Pre-radiation		Post-radiation		% Difference between Avg.
NJ3600L	**363u**	(374u, 343u)	**358u**	(378u, 330u)	**-1.38**
NJ903L	**282u**	(282u, 281u)	**283u**	(288u, 277u)	**.355**
NJ1800DL	**279u**	(297u, 249u)	**274u**	(292u, 246u)	**-1.79**
2N6451	**318u**	(323u, 312u)	**315u**	(320u, 306u)	**-.943**
2SK152A	**277u**	(282u, 272u)	**275u**	(280u, 268u)	**-.722**
2N4858	**288u**	(298u, 278u)	**288u**	(298u, 278u)	**0**
2N4416A	**176u**	(184u, 172u)	**176u**	(183u, 172u)	**0**
IMF5912	**93.8u**	(105u, 82.9u)	**93.0u**	(105u, 83.1u)	**-.853**
2N5432	**111u**	(155u, 64.6u)	**111u**	(154u, 64.3u)	**0**

3.2.2 Lambda

Another dc modeling parameter is lambda. Lambda quantitatively describes the amount of change in drain current as a function of change in V_{DS} when the device is operating in the saturation region. The drain current can saturate as a result of the channel being pinched off, drift velocity saturation or a combination of the two [24]. The channel, being pinched off on the drain side for a n-channel JFET, is depleted of majority carriers in this region and any change in the drain potential varies this depletion region slightly. It is this slight change in the size of the depletion

region that varies the effective length of the channel thus changing the conductivity slightly. This effect is called channel length modulation.

3.2.2.1 Measurement Theory

The drain current can be written as

$$I_D = I_{DSS}\left(1 - \frac{V_{GS}}{VTO}\right)^{NP}\left(1 + \lambda \cdot V_{DS}\right). \tag{3.9}$$

This can be placed in a linear form by letting $y = I_D$, $x = V_{DS}$, and V_{GS} be constant.

$$y = C_1\left(\lambda \cdot x + 1\right) \tag{3.12}$$

where

$$C_1 = I_{DSS}\left(1 - \frac{V_{GS}}{VTO}\right)^{NP}. \tag{3.13}$$

At the x-axis intercept (y = 0) equation 3.12 becomes

$$x = -\frac{1}{\lambda}. \tag{3.14}$$

Thus

$$\lambda = -\left.\frac{1}{V_{DS}}\right|_{I_D = 0}. \tag{3.15}$$

Lambda is graphically illustrated in Figure 3.3 below.

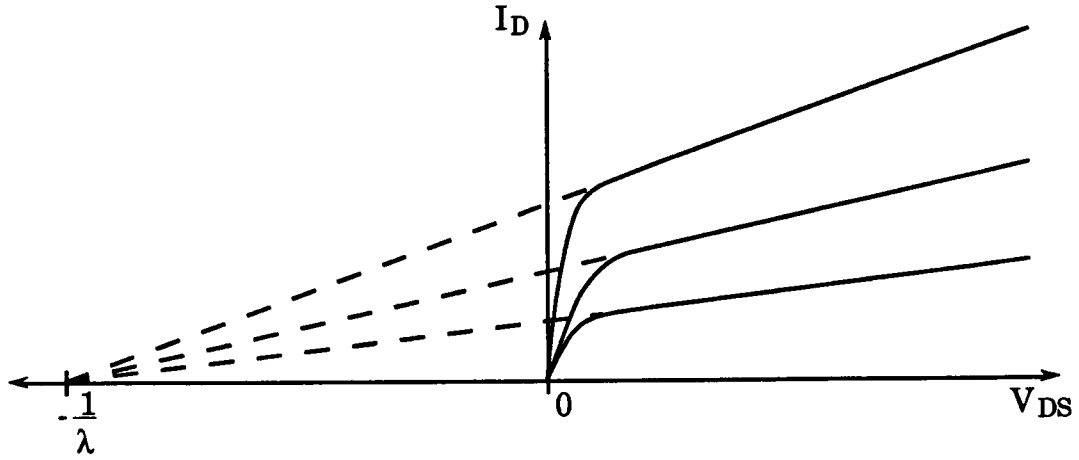


Figure 3.3. Measurement of lambda graph.

3.2.2.2 Radiation Effects

The value of the x-axis intercept was found to increase significantly after the devices were irradiated. Since lambda is based on some very complex mechanisms that occur in the depletion region, no explanation of this shift due to radiation was made. It is interesting to note that for devices having larger pre-radiation values of 1/lambda, there was less percentage change after radiation.

3.2.2.3 Measurement Results

The x-axis intercept, 1/lambda, was evaluated with $I_D \approx 5mA$ and $V_{DS} \approx 2.5V$ as shown in Table 3.4.

Table 3.4. Summary of 1/lambda (V) measurements.

Part	Pre-radiation		Post-radiation		% Difference between Avg.
NJ3600L	**62.7**	(90.1, 35.4)	**73.9**	(90.4, 52.5)	**17.9**
NJ903L	**48.6**	(51.8, 45.3)	**70.4**	(73.0, 67.8)	**44.9**
NJ1800DL	**52.9**	(66.3, 32.8)	**71.1**	(79.2, 51.6)	**34.4**
2N6451	**48.8**	(61.4, 40.4)	**77.0**	(94.9, 64.5)	**57.8**
2SK152A	**13.1**	(14.1, 12.1)	**18.8**	(20.3, 17.4)	**43.5**
2N4858	**40.9**	(50.2, 31.5)	**74.0**	(89.5, 58.4)	**80.9**
2N4416A	**11.9**	(14.0, 10.4)	**30.9**	(37.6, 26.3)	**160**
IMF5912	**14.7**	(15.0, 14.4)	**37.5**	(39.8, 36.3)	**155**
2N5432	**9.08**	(10.2, 6.89)	**20.2**	(30.4, 11.3)	**123**

3.2.3 NP (Square law relationship)

For operation in the saturation region, NP is the exponent that describes the drain current as a function of applied gate to source voltage. NP is a modeling parameter and is most directly related to the doping

profile of gate to channel region. For the standard quadratic equation NP is normally taken to be 2.0.

3.2.3.1 Measurement Theory

Equation 3.9 can be written as

$$I_D = I_{DSS}\left(1 - \frac{V_{GS}}{VTO}\right)^{NP}\left(1 + \lambda \cdot V_{DS}\right) = C_2\left(1 - \frac{V_{GS}}{VTO}\right)^{NP} \tag{3.16}$$

where

$$C_2 = I_{DSS}\left(1 + \lambda \cdot V_{DS}\right). \tag{3.17}$$

The definition of g_m (equation 3.10) can be simplified by applying equation 3.17 which yields

$$g_m = -\frac{NP \cdot C_2}{VTO}\left(1 - \frac{V_{GS}}{VTO}\right)^{NP-1} \tag{3.18}$$

Solving equation 3.16 for V_{GS} yields

$$V_{GS} = \left[1 - \left(\frac{I_D}{C_2}\right)^{\frac{1}{NP}}\right] VTO\ . \tag{3.19}$$

Substituting equation 3.19 into equation 3.18 and simplifying gives

$$g_m = -\frac{NP\,(C_2)^{\frac{1}{NP}}}{VTO}(I_D)^{1-\frac{1}{NP}}. \tag{3.20}$$

Taking the logarithm of both sides of 3.20 and rearranging

$$\log(g_m) = \left(1 - \frac{1}{NP}\right)\log(I_D) + \log\left[-\frac{NP\,(C_2)^{\frac{1}{NP}}}{VTO}\right] \tag{3.21}$$

which is in a linear form given

$$y = \log(g_m),$$
$$x = \log(I_D),$$

and

$$b = \log\left[-\frac{(C_2)^{\frac{1}{NP}}}{VTO}\right].$$

NP can be found from the slope (m) as

$$m = 1 - \frac{1}{NP} \Rightarrow NP = \frac{1}{1-m}. \tag{3.22}$$

Equation 3.22 is illustrated in Figure 3.4.

Using the parameter analyzer, an evaluation of the slope of the line as shown in Figure 3.4 showed errors as large as +/- 6% for small changes

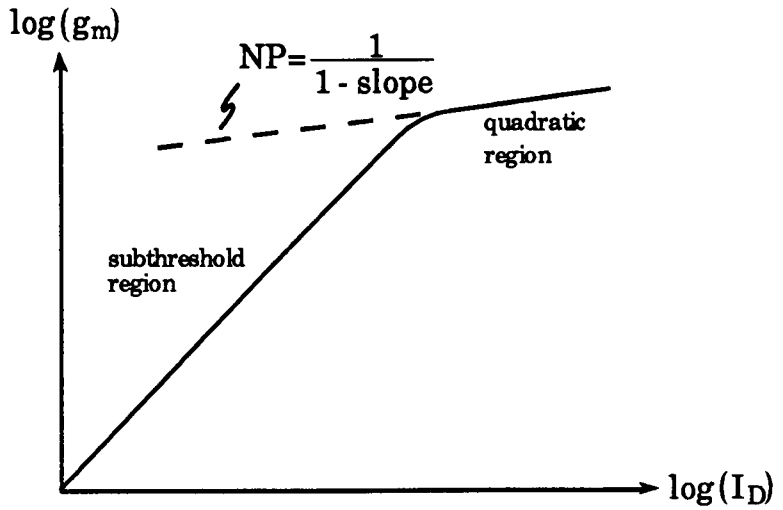


Figure 3.4. Measurement of NP graph.

in the data points used to define the line. This error was reduced by choosing the data points carefully and could be avoided in future measurements by increasing the integration time of the parameter analyzer.

3.2.3.2 Radiation Effects

The damage incurred by gamma radiation should not have much of an effect on the doping profile, thus NP should be fairly insensitive to the levels of gamma radiation applied to the devices.

3.2.3.3 Measurements

The results (see Table 3.5) showed little if any change in the value of NP for the devices tested. The small changes that did occur could possibly be a result of the measurement errors mentioned.

Table 3.5. Summary of NP measurements.

Part	Pre-radiation	Post-radiation	% Difference between Avg.
NJ3600L	**2.19** (2.43, 1.95)	**2.15** (2.30, 1.95)	**-1.83**
NJ903L	**1.72** (1.77, 1.67)	**1.71** (1.80, 1.62)	**-.581**
NJ1800DL	**2.28** (2.49, 2.14)	**2.29** (2.50, 2.15)	**.439**
2N6451	**1.87** (2.10, 1.72)	**1.91** (1.97, 1.81)	**2.14**
2SK152A	**1.77** (1.80, 1.75)	**1.75** (1.76, 1.73)	**-1.13**
2N4858	**1.76** (1.77, 1.75)	**1.78** (1.78, 1.78)	**1.14**
2N4416A	**1.41** (1.47, 1.37)	**1.40** (1.46, 1.36)	**-.709**
IMF5912	**1.44** (1.46, 1.41)	**1.44** (1.46, 1.41)	**0**
2N5432	**1.37** (1.41, 1.29)	**1.37** (1.41, 1.28)	**0**

3.2.4 VTO, I_{DSS}, and Beta

VTO is the threshold voltage, which for JFETs is most commonly referred to as the pinch-off voltage (V_P). Theoretically VTO is the voltage at which the depletion regions, formed from the applied drain and gate

potentials, meet. This condition is called pinch-off. More importantly VTO defines the transition from quadratic to subthreshold operation. As the magnitude of V_{GS} is made greater than the magnitude of VTO the device characteristics become defined by subthreshold operation.

I_{DSS} is the saturation current, and is the current at which the channel pinches off with the gate to source potential at zero volts.

Beta is strictly a modeling parameter that is a function of VTO, NP, and I_{DSS}. From equation 3.3 Beta can be written as

$$\text{Beta} = \frac{I_{DSS}}{|VTO|^{NP}} . \tag{3.23}$$

3.2.4.1 Measurement Theory

Given equation 3.9

$$I_D = I_{DSS}\left(1 - \frac{V_{GS}}{VTO}\right)^{NP}\left(1 + \lambda \cdot V_{DS}\right)$$

which can be rearranged such that

$$\left[\frac{I_D}{I_{DSS}}\frac{1}{\left(1 + \lambda \cdot V_{DS}\right)}\right]^{\frac{1}{NP}} = 1 - \frac{V_{GS}}{VTO} . \tag{3.24}$$

By letting

$$y = \left[\frac{I_D}{I_{DSS}} \frac{1}{(1 + \lambda \cdot V_{DS})} \right]^{\frac{1}{NP}}$$

and

$$x = V_{GS}$$

equation 3.24 can be written as

$$y = \left(-\frac{1}{VTO} \right) x + 1 . \tag{3.25}$$

This is a linear function where the slope (m) and the y-axis intercept (b) are

$$m = -\frac{1}{VTO}$$
$$b = 1 .$$

Given λ, V_{DS}, and NP equation 3.25 can be plotted for different values of I_{DSS} until the y-axis intercept equals one at which point

$$VTO = -\frac{1}{m} \tag{3.26}$$

and I_{DSS} is given from the iteration. An example of this measurement is shown in Figure 3.5.

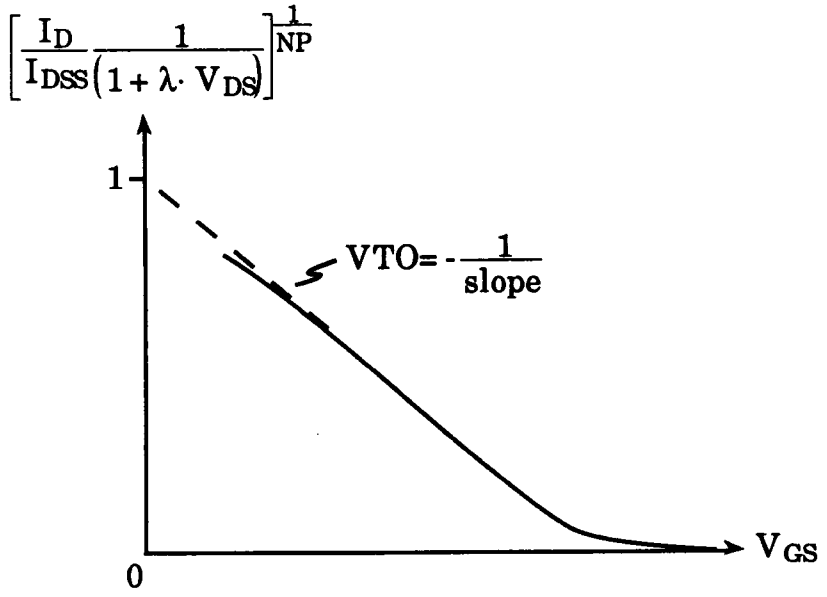


Figure 3.5. VTO, I_{DSS}, and Beta measurement.

A useful feature of this method of measurement is that it allows the measurement of JFETs that have large values of I_{DSS} to be made at a lower current level so that heating effects (i.e., temperature effects) will not produce errors in the measurement.

3.2.4.2 Radiation Effects

The changes in both I_{DSS} and VTO due to gamma radiation damage should be small. Since they are both very dependant on doping profiles, device geometry, and carrier mobility, it would be difficult to predict radiation effects on these parameters without this information.

3.2.4.3 Measurements

Because of the inaccuracies in the measurement of NP (which in reality probably had no change), the value of NP used in the post-radiation measurements was the same as that used in the pre-radiation measurements. The change that occurred in lambda after radiation exposure was included the measurement.

VTO showed little change after radiation, whereas I_{DSS} typically showed the greater change (Tables 3.6 and 3.7).

Table 3.6. Summary of VTO (V) measurements.

Part	Pre-radiation		Post-radiation		% Difference between Avg.
NJ3600L	**.815**	(1.10, .590)	**.818**	(1.10, .597)	**.368**
NJ903L	**1.06**	(1.14, .980)	**1.06**	(1.14, .976)	**0**
NJ1800DL	**.952**	(1.69, .662)	**.950**	(1.68, .669)	**-.210**
2N6451	**.739**	(.930, .518)	**.740**	(.925, .524)	**.135**
2SK152A	**.898**	(.935, .816)	**.884**	(.930, .819)	**-1.56**
2N4858	**2.27**	(2.84, 1.69)	**2.26**	(2.82, 1.69)	**-.441**
2N4416A	**2.72**	(3.11, 2.12)	**2.71**	(3.07, 2.11)	**-.368**
IMF5912	**2.55**	(2.67, 2.44)	**2.55**	(2.67, 2.43)	**0**
2N5432	**7.42**	(7.94, 6.90)	**7.45**	(8.01, 6.94)	**.404**

Table 3.7. Summary of I_{DSS} (mA) measurements.

Part	Pre-radiation		Post-radiation		% Difference between Avg.
NJ3600L	**268**	(450, 145)	**269**	(455, 145)	**.373**
NJ903L	**153**	(170, 135)	**152**	(170, 134)	**-.654**
NJ1800DL	**207**	(520, 92.0)	**208**	(525, 92.0)	**.483**
2N6451	**11.7**	(17.0, 6.00)	**11.9**	(17.2, 6.20)	**1.71**
2SK152A	**10.5**	(11.0, 9.20)	**10.5**	(11.3, 9.40)	**0**
2N4858	**42.0**	(56.0, 28.0)	**42.0**	(56.0, 28.0)	**0**
2N4416A	**7.90**	(9.00, 6.00)	**8.65**	(9.80, 6.60)	**9.49**
IMF5912	**11.1**	(11.7, 10.5)	**11.8**	(12.5, 11.2)	**6.31**
2N5432	**408**	(435, 395)	**457**	(485, 442)	**12.0**

3.2.5 NS

NS is a shape factor for the exponential characteristics of the subthreshold current. For MOSFET devices [7]

$$NS = 1 + \frac{C_D}{C_{OX}}$$

where

C_D = surface depletion capacitance per unit area
C_{OX} = oxide capacitance per unit area

In a JFET no oxide layer exists and by theory NS should have a value of one [25].

3.2.5.1 Measurement Theory

Given $|V_{GS}| >> |VTO|$

$$I_D \approx IO \left\{ \exp\left(\frac{V_{GS} - VTO}{NS \cdot V_T} \right) \left[1 - \exp\left(\frac{-V_{DS}}{V_T} \right) \right] \right\}. \tag{3.27}$$

For $V_{DS} > V_T$

$$I_D = IO \cdot \exp\left(\frac{V_{GS} - VTO}{NS \cdot V_T} \right). \tag{3.28}$$

Taking the natural logarithm of equation 3.28

$$\ln\left(\frac{I_D}{IO} \right) = \frac{V_{GS} - VTO}{NS \cdot V_T} \tag{3.29}$$

which can be written as

$$\ln(I_D) = \frac{V_{GS} - VTO}{NS \cdot V_T} + \ln(IO). \tag{3.30}$$

Converting equation 3.30 to logarithm (base ten) using the relationship

$$\ln(y) = \frac{\log(y)}{\log(e)} \tag{3.31}$$

yields

$$\frac{\log(I_D)}{\log(e)} = \frac{V_{GS} - VTO}{NS \cdot V_T} + \frac{\log(IO)}{\log(e)} . \tag{3.32}$$

As a result of multiplying through by log (e) and rearranging

$$\log(I_D) = \left[\frac{\log(e)}{NS \cdot V_T}\right] V_{GS} - VTO\left[\frac{\log(e)}{NS \cdot V_T}\right] + \log(IO) . \tag{3.33}$$

Equation 3.33 can be written in a linear form by letting y = log (I_D) and x = V_{GS} so that

$$y = \left[\frac{\log(e)}{NS \cdot V_T}\right] x - VTO\left[\frac{\log(e)}{NS \cdot V_T}\right] + \log(IO) . \tag{3.34}$$

For equation 3.34 the slope (m) is defined as

$$m = \frac{\log(e)}{NS \cdot V_T} \Rightarrow NS = \frac{\log(e)}{m \cdot V_T} . \tag{3.35}$$

The measurement of NS is illustrated in Figure 3.6.

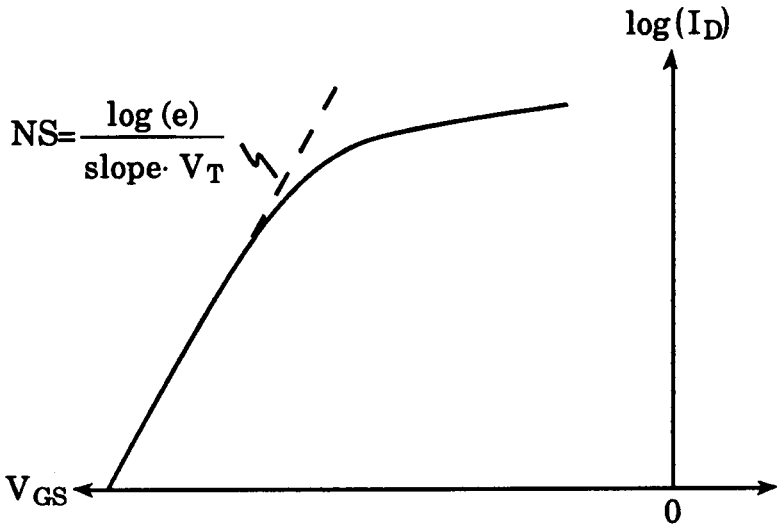


Figure 3.6. Measurement of NS.

3.2.5.2 Radiation Effects

Ionization of surface states in a JFET due to gamma radiation would create an almost insulated gate-like region in the JFET [14]. This would cause an increase in the value of NS.

3.2.5.3 Measurements

NS was harder to characterize after radiation due to the increase in gate leakage current that reduced the definable subthreshold region. The measurement results are shown in Table 3.8.

Table 3.8. Summary of NS measurements.

Part	Pre-radiation	Post-radiation	% Difference between Avg.
NJ3600L	**1.01** (1.01, 1.00)	**1.02** (1.03, 1.02)	**.990**
NJ903L	**1.01** (1.01, 1.01)	**1.15** (1.17, 1.14)	**13.9**
NJ1800DL	**1.00** (1.00, .994)	**1.05** (1.06, 1.03)	**5.00**
2N6451	**1.01** (1.02, .994)	**1.03** (1.04, 1.02)	**1.98**
2SK152A	**1.07** (1.08, 1.06)	**1.11** (1.12, 1.10)	**3.74**
2N4858	**1.02** (1.03, 1.01)	**1.06** (1.06, 1.05)	**3.92**
2N4416A	**1.18** (1.23, 1.15)	**1.27** (1.31, 1.23)	**7.63**
IMF5912	**1.20** (1.21, 1.18)	**1.33** (1.37, 1.31)	**10.8**
2N5432	**1.43** (1.53, 1.32)	**2.03** (2.22, 1.80)	**42.0**

3.2.6 IO (threshold current)

From equation 3.28 the current in the subthreshold region can be expressed as

$$I_D = IO \cdot \exp\left(\frac{V_{GS} - VTO}{NS \cdot V_T}\right).$$

This expression can be related more to device parameters and geometries by [9]

$$I_D = \frac{N_D \cdot q \cdot D \cdot L_D}{L} \sqrt{2\pi} \exp\left(-\frac{|V_G| - |V_P|}{V_T}\right) \qquad (3.36)$$

where

N_D = concentration of donors in the channel
D = diffusion coefficient = $\mu_n \cdot V_T$
μ_n = moblilty of majority carriers in the channel
L_D = Debye length = $\sqrt{\frac{\epsilon_{Si} \cdot V_T}{q \cdot N_D}}$
ϵ_{Si} = permittivity of silicon = 11.7 .

Thus by expanding terms in equation 3.36 and simplifying, IO can be written as

$$IO = \frac{\mu_n \cdot V_T}{L} \sqrt{2\pi \cdot q \cdot \epsilon_{Si} \cdot V_T \cdot N_D} \ . \tag{3.37}$$

3.2.6.1 Measurement Theory

From equation 3.28

$$I_D = IO \cdot \exp\left(\frac{V_{GS} - VTO}{NS \cdot V_T}\right)$$

it can be seen that IO is the extrapolated value of I_D (as defined in the subthreshold region) when V_{GS} = VTO. This is illustrated in Figure 3.7. The extrapolated value is usually out of range on a graph of $\log(I_D)$ vs V_{GS} and so another method of measurement must be used.

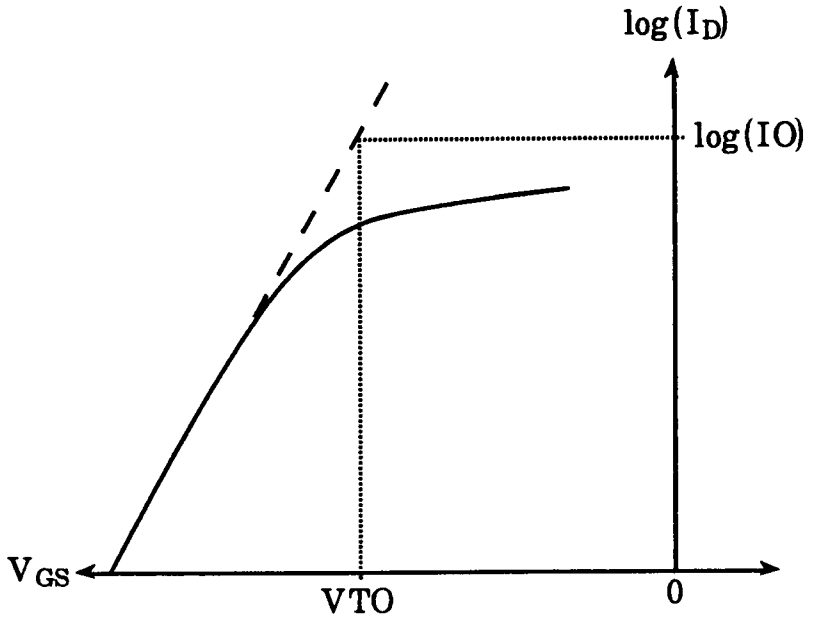


Figure 3.7. Definition of IO.

Writing equation 3.28 as

$$IO = \frac{I_D}{\exp\left(\frac{V_{GS} - VTO}{NS \cdot V_T}\right)} \tag{3.38}$$

the value of IO can be calculated by substituting values for V_{GS} and I_D that come from a measured point of the subthreshold region.

Using the y-axis intercept of equation 3.33 to solve for IO was avoided due to errors in the parameter analyzer's calculation of the intercept.

3.2.6.2 Radiation Effects

From equation 3.37

$$IO = \frac{\mu_n \cdot V_T}{L} \sqrt{2\pi \cdot q \cdot \epsilon_{Si} \cdot V_T \cdot N_D}$$

a decrease in channel mobility and a decrease in the the number of donors in the channel would both cause a decrease in the value of IO.

3.2.6.3 Measurements

Some of the shift in IO can be attributed to an increase in the gate leakage current which made characterization of the subthreshold region more difficult. Note in Table 3.9 the wide range of values for IO, due to the exponential behavior of equation 3.38. Thus, the accuracy of the stated IO value is probably no better than +/- 50%. Indeed, one really needs a better characterization of subthreshold operation than is currently available.

3.2.7 Gate Leakage Current

The gate leakage current of a JFET is the sum of the surface, reverse saturation, and generation leakage currents [26]. The surface leakage [27] current is a result of surface generation sites at the gate surface.

Table 3.9. Summary of IO (A) measurements.

Part	Pre-radiation		Post-radiation		% Difference between Avg.
NJ3600L	**1.03m**	(2.32m, .508m)	**.997m**	(2.30m, .417m)	**-3.20**
NJ903L	**72.6**	(145, .321)	**36.6m**	(66.7m, 6.49m)	**-100**
NJ1800DL	**9.54m**	(11.4m, 7.06m)	**5.76m**	(7.52m, 2.94m)	**-39.6**
2N6451	**173u**	(386u, 31.3u)	**155u**	(314u, 30.6u)	**-10.4**
2SK152A	**188u**	(274u, 34.9u)	**163u**	(196u, 133u)	**-13.3**
2N4858	**122u**	(154u, 90.4u)	**139u**	(213u, 64.8u)	**13.7**
2N4416A	**47.2m**	(136m, 7.34m)	**18.0m**	(43.1m, 4.80m)	**-62.0**
IMF5912	**6.13M**	(24.5M, 937)	**64.5K**	(256K, 75.3)	**-99.0**
2N5432	**1.67T**	(6.68T, 136)	**2.34M**	(9.35M, 15.8m)	**-100**

The reverse saturation current occurs in any reversed biased junction and is defined as [26]

$$I_{RS} = q \cdot A \left(\frac{D_p \cdot p_{no}}{L_p} + \frac{D_n \cdot n_{po}}{L_n} \right) \left[\exp\left(\frac{V_R}{V_T} \right) - 1 \right] \tag{3.39}$$

where

A = cross-sectional area
D = diffusion constant for respective materials
p_{no} = density of holes in the n material's valence band
n_{po} = density of electrons in the p material's valence band
L = diffusion length
V_R = reverse voltage applied to the junction .

When the junction is reversed biased the value of V_R is negative in equation 3.39. If the magnitude of this reverse bias is a little larger than V_T than the current basically becomes independent of any increase in reverse bias.

The generation current is the main component of the leakage current and for an abrupt junction is defined as [26,28]

$$I_{gen} = \frac{q \cdot n_i \cdot A}{2 \cdot \tau_0} \left[2 \cdot \frac{\epsilon_{SI}}{q} \left(\frac{1}{N_a} + \frac{1}{N_d} \right) (\Phi_i - V_R) \right]^{\frac{1}{2}} \tag{3.40}$$

where

n_i = Intrensic carrier concentration
τ_0 = effective minority-carrier lifetime in the depletion region
$N_a = \frac{\text{number of acceptors}}{cm^3}$
$N_d = \frac{\text{number of donors}}{cm^3}$
Φ_i = built-in potential .

3.2.7.1 Measurement Theory

The gate leakage current (I_G) was characterized as a function of V_{DS} at a drain current level of 100uA and was measured using the parameter analyzer. An example plot of the gate leakage current is shown in Figure 3.8.

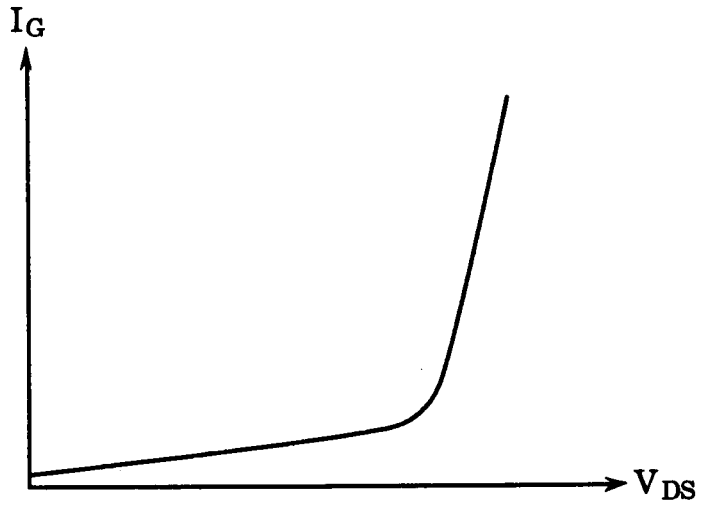


Figure 3.8. Gate current versus drain to source voltage.

3.2.7.2 Radiation Effects

Gamma radiation damage causes the gate current to increase significantly. This is due to an increase in both surface states in the device and an increase in generation currents. The n-channel JFET experiences much greater increases in the gate current after exposure to gamma radiation than the p-channel JFET [15].

3.2.7.3 Measurements

The measurement results for the gate leakage current are shown in Table 3.10 and 3.11.

Table 3.10. I_G (A) for I_D = 100uA and V_{DS} = 2.5V.

Part	Pre-radiation		Post-radiation	
NJ3600L	**285p**	(409p, 106p)	**6.25n**	(10.4n, 4.02n)
NJ903L	**85.4p**	(170p, .750p)	**25.6n**	(33.2n, 17.9n)
NJ1800DL	**.880p**	(1.10p, .750p)	**3.70n**	(4.18n, 3.34n)
2N6451	**.120p**	(.200p, .050p)	**185p**	(211p, 170p)
2SK152A	**.588p**	(1.00p, .375p)	**.839n**	(1.43n, .609n)
2N4858	**.952p**	(1.55p, .354p)	**716p**	(812p, 619p)
2N4416A	**< .1p**	(< .1p, < .1p)	**377p**	(399p, 327p)
IMF5912	**.525p**	(.900p, .150p)	**75.7p**	(82.5p, 68.6p)
2N5432	**61.8p**	(157p, 13.4p)	**14.1n**	(14.5n, 13.4n)

Table 3.11. I_G (A) for I_D = 100uA and V_{DS} = 5V.

Part	Pre-radiation		Post-radiation	
NJ3600L	**463p**	(665p, 176p)	**9.03n**	(14.7n, 5.64n)
NJ903L	**86.2p**	(171p, 1.40p)	**26.0n**	(33.6n, 18.3n)
NJ1800DL	**1.45p**	(1.70p, 1.15p)	**4.70n**	(5.31n, 4.15n)
2N6451	**.160p**	(.250p, .087p)	**229p**	(257p, 214p)
2SK152A	**.913p**	(1.55p, .600p)	**1.14n**	(1.96n, .862n)
2N4858	**1.43p**	(2.30p, .550p)	**827p**	(932p, 721p)
2N4416A	**< .1p**	(< .1p, < .1p)	**417p**	(443p, 363p)
IMF5912	**.590p**	(.961p, .200p)	**88.0p**	(95.1p, 79.8p)
2N5432	**68.0p**	(173p, 14.7p)	**15.3n**	(15.8n, 14.5n)

3.3 Capacitance

The capacitance of a normally biased JFET can be modeled by C_{GS} and C_{GD} as shown in Figure 3.9.

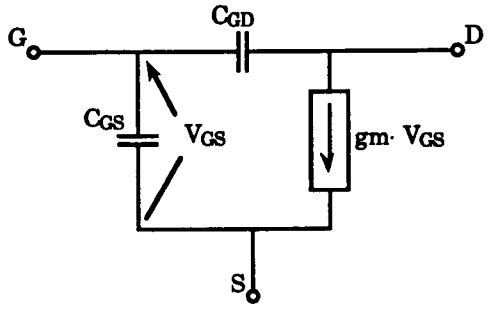


Figure 3.9. Small signal JFET model.

The capacitances C_{GS} and C_{GD} are both formed due to depletion regions that occur at the p and n material interfaces of these junctions. These depletion region capacitances can be modeled by [28]

$$C = \left[\frac{q \cdot \epsilon_{SI}}{2\left(\frac{1}{N_a} + \frac{1}{N_d}\right)(\Phi_i - V_R)} \right]^{\frac{1}{2}} \tag{3.41}$$

which is the capacitance per unit area of a reversed biased abrupt junction. The majority carrier doping values N_a and N_d are for an (assumed) uniformly doped junction. An example plot of equation 3.41 is shown in Figure 3.10.

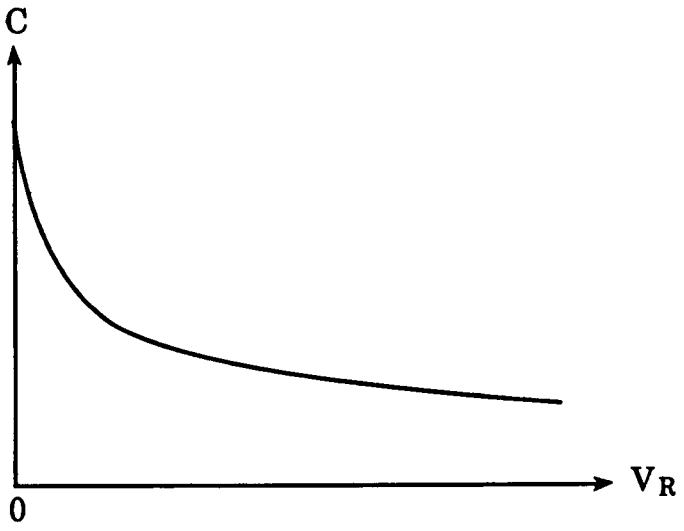


Figure 3.10. Capacitance of junction vs reverse voltage.

3.3.1 Radiation Effects

The changes in junction capacitance due to radiation induced damage are typically small and have been observed to both increase and decrease in measured devices [14]. Based on equation 3.41 the direction and amount of change would be dependant on the actual nonlinear doping profiles of the junction and the resulting change in the depletion region after radiation. Also, capacitances formed between the surface and the bulk could contribute to the measurement and changes in the junction capacitance.

3.3.2 Measurement Techniques

Both C_{ISS} and C_{RSS} of the JFETs were measured using the HP4280A capacitance meter.

C_{ISS} is a measure of the parallel combination of the gate to source and gate to drain capacitance as a function of voltage. The voltage is applied so that both gate to source and gate to drain junctions are reversed biased as in normal operation. The connections for the measurement of C_{ISS} are shown in Figure 3.11.

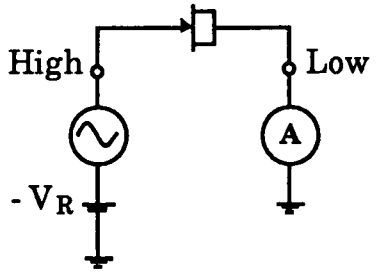


Figure 3.11. C_{ISS} measurement connections.

C_{RSS} is a measure of the gate to drain capacitance as a function of voltage. The same reverse bias is applied to both junctions as in the measurement of C_{ISS}, and the effect of the gate to source capacitance is removed through guarding the source. The connections for this measurement are shown in Figure 3.12.

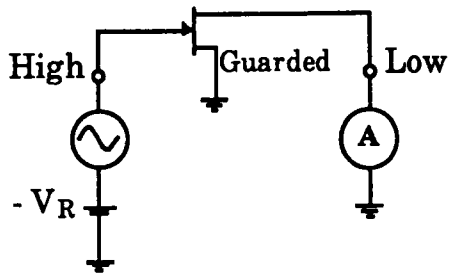


Figure 3.12. C_{RSS} measurement connections (ground connections act as a guard).

3.3.3 Measurements

On the following curves (Figures 3.13 - 3.21) the "error bars" indicate the range (minimum to maximum) for all units of each type tested. Note also that the simple capacitance equation 3.41 (as shown in Figure 3.10) does not necessarily apply for V_R close to 0V.

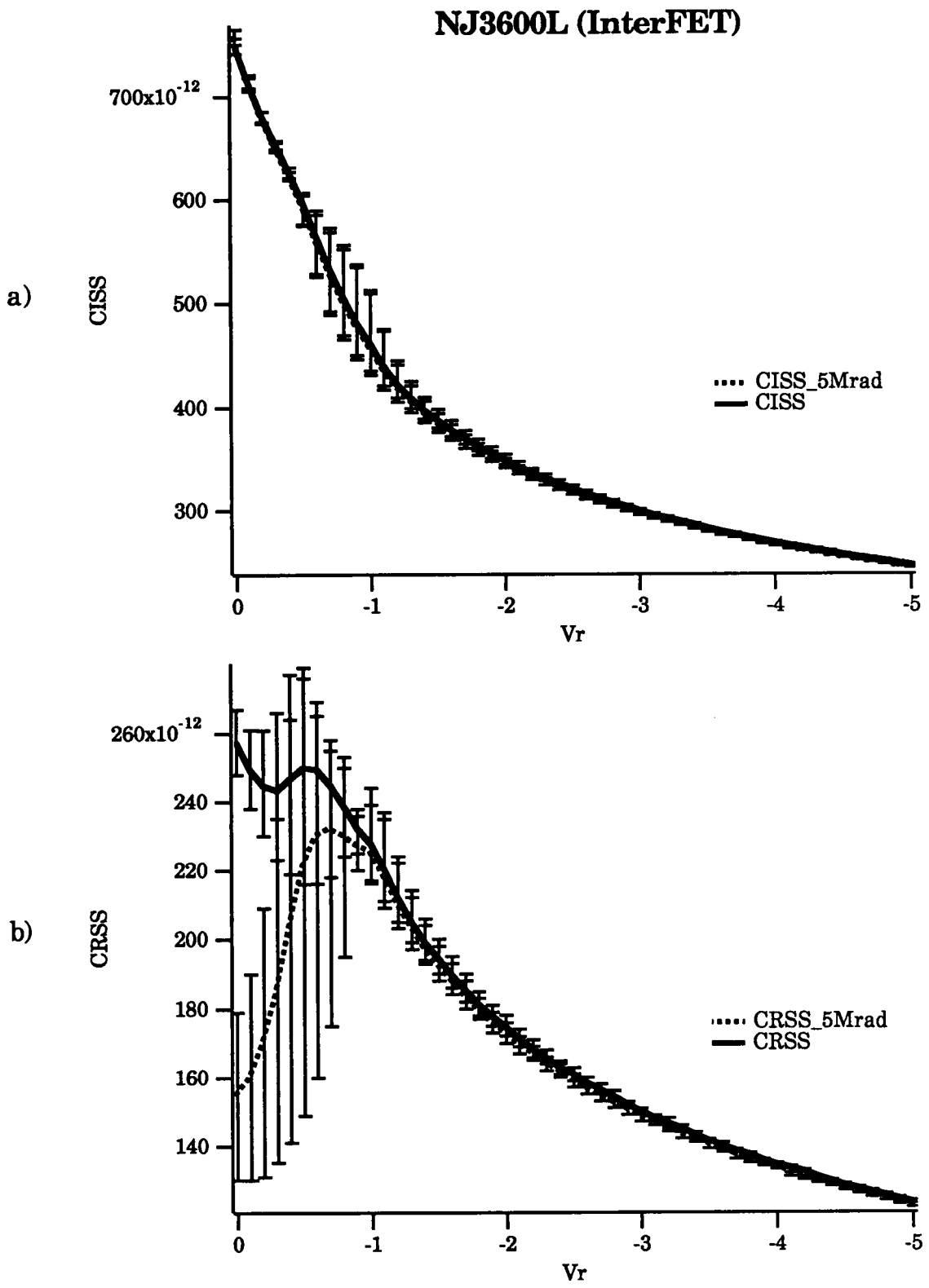


Figure 3.13. a) CISS vs Vr and b) CRSS vs Vr.

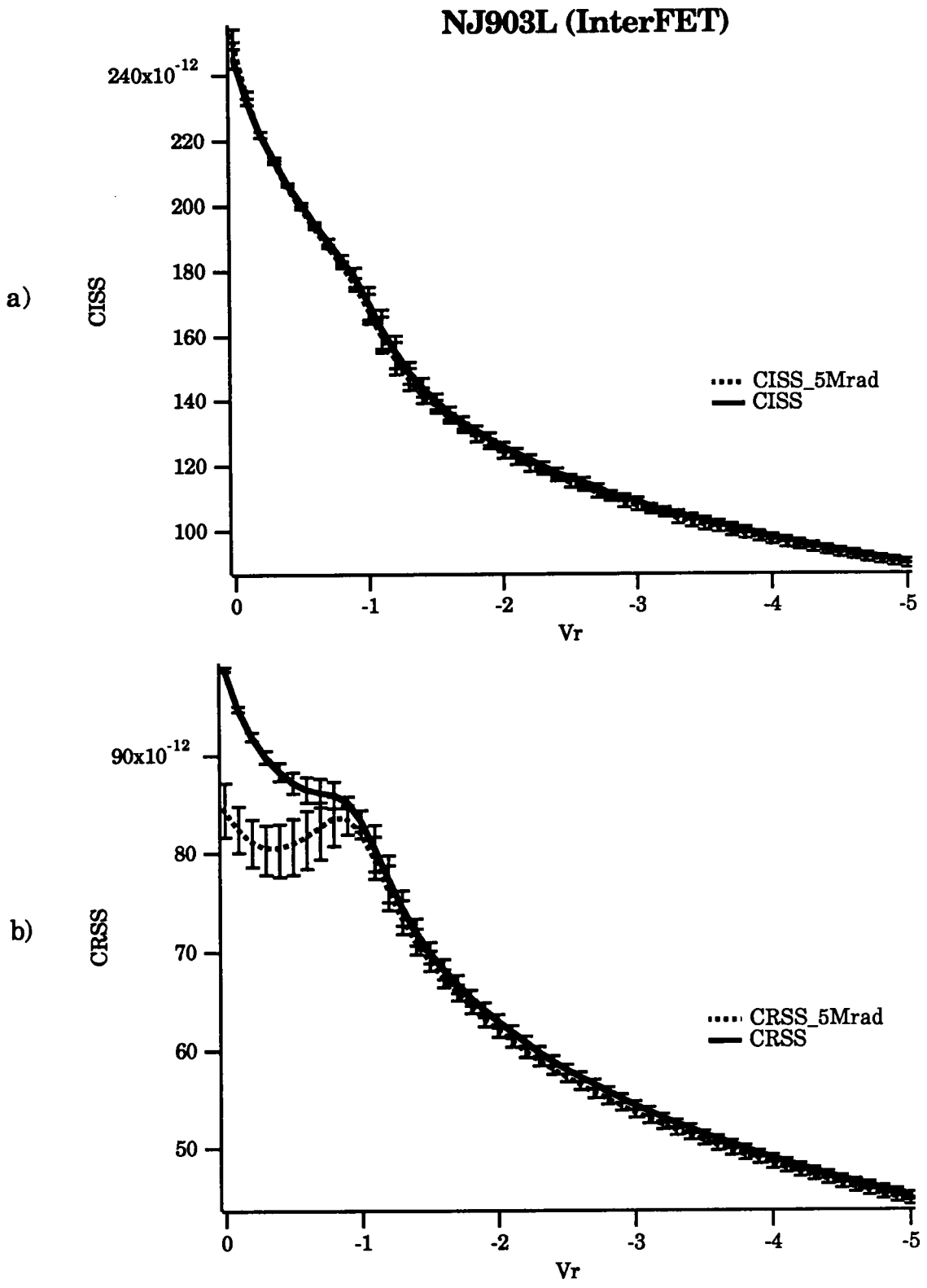


Figure 3.14. a) CISS vs Vr and b) CRSS vs Vr.

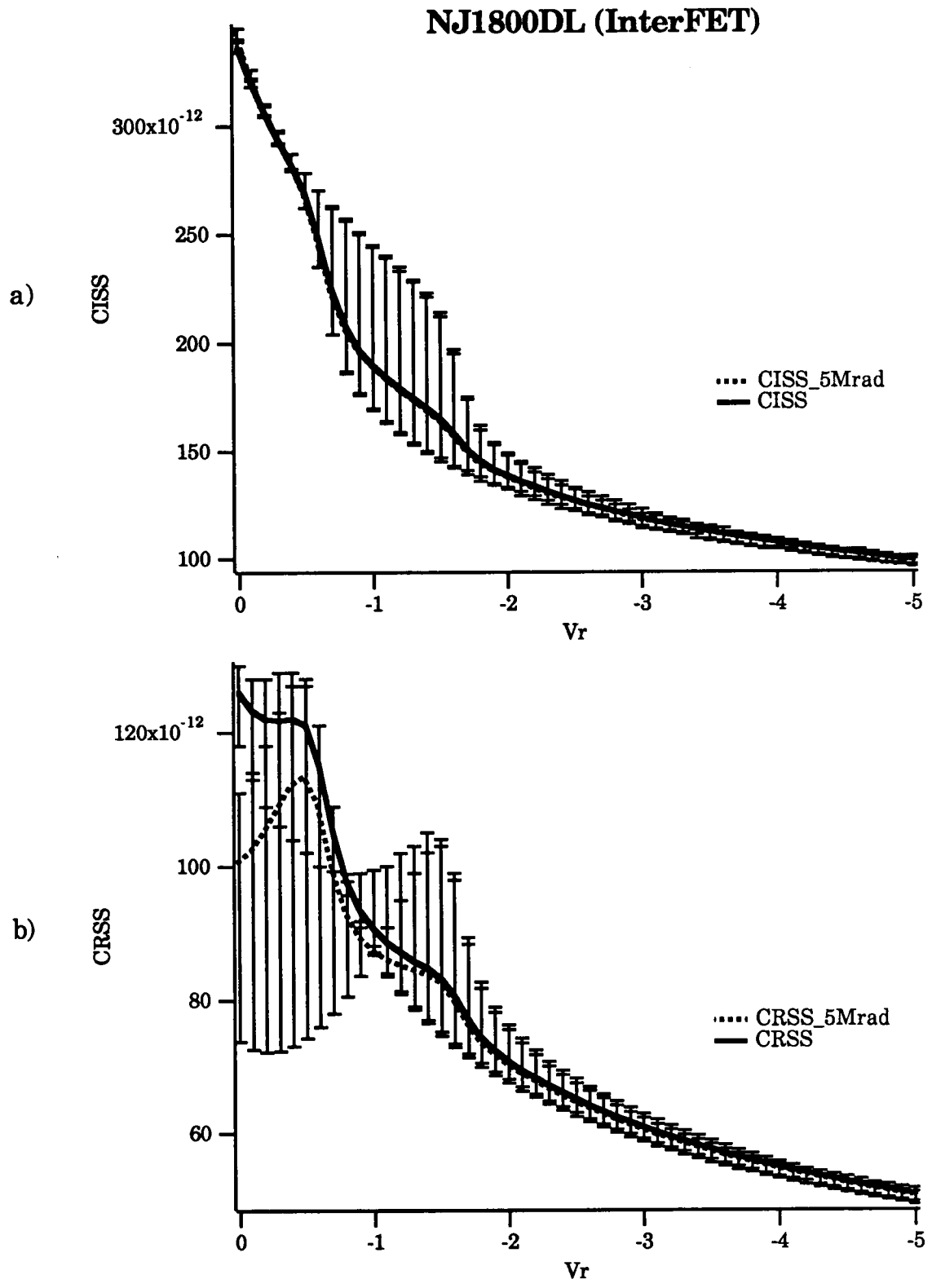


Figure 3.15. a) CISS vs Vr and b) CRSS vs Vr.

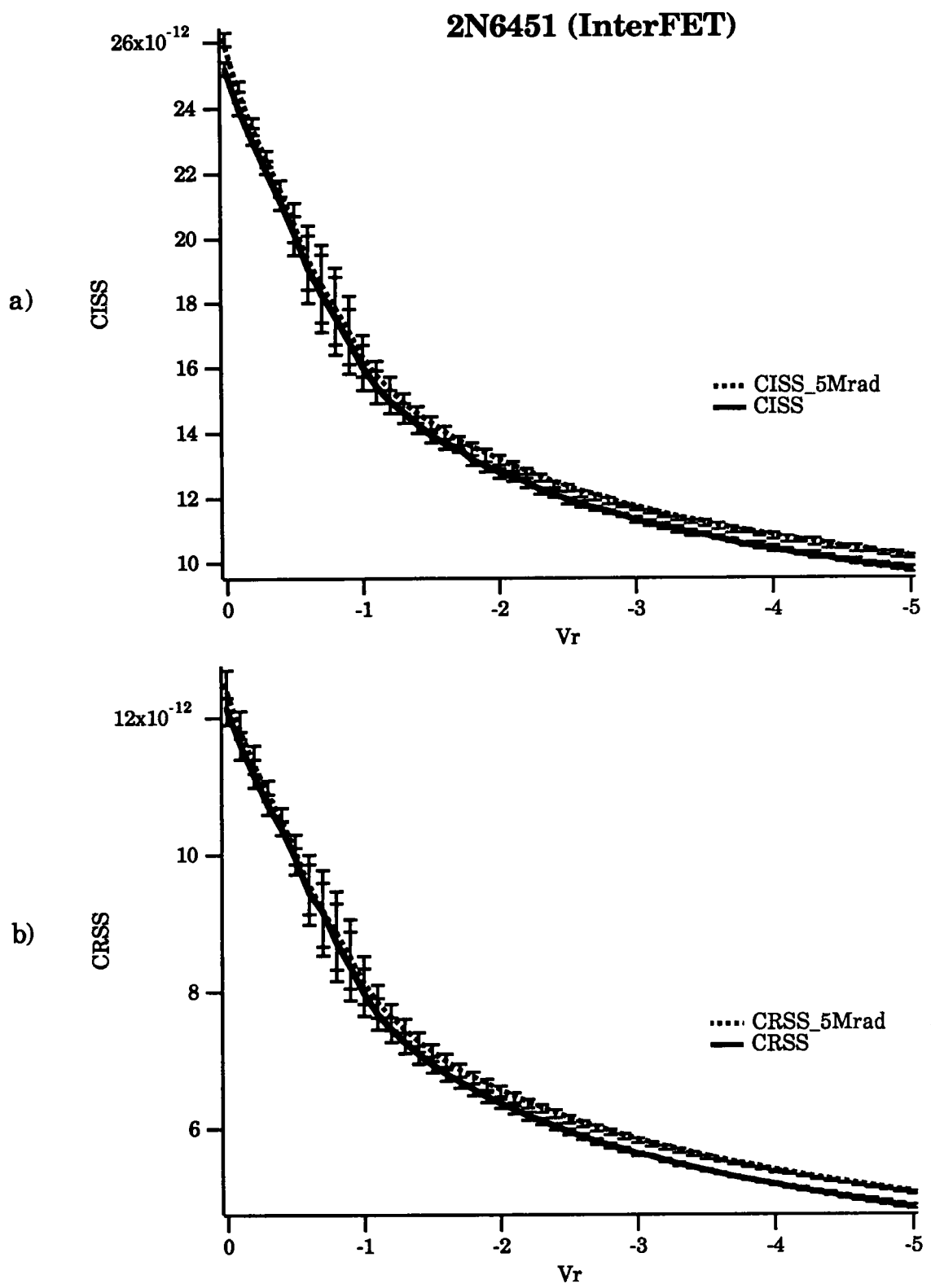


Figure 3.16. a) CISS vs Vr and b) CRSS vs Vr.

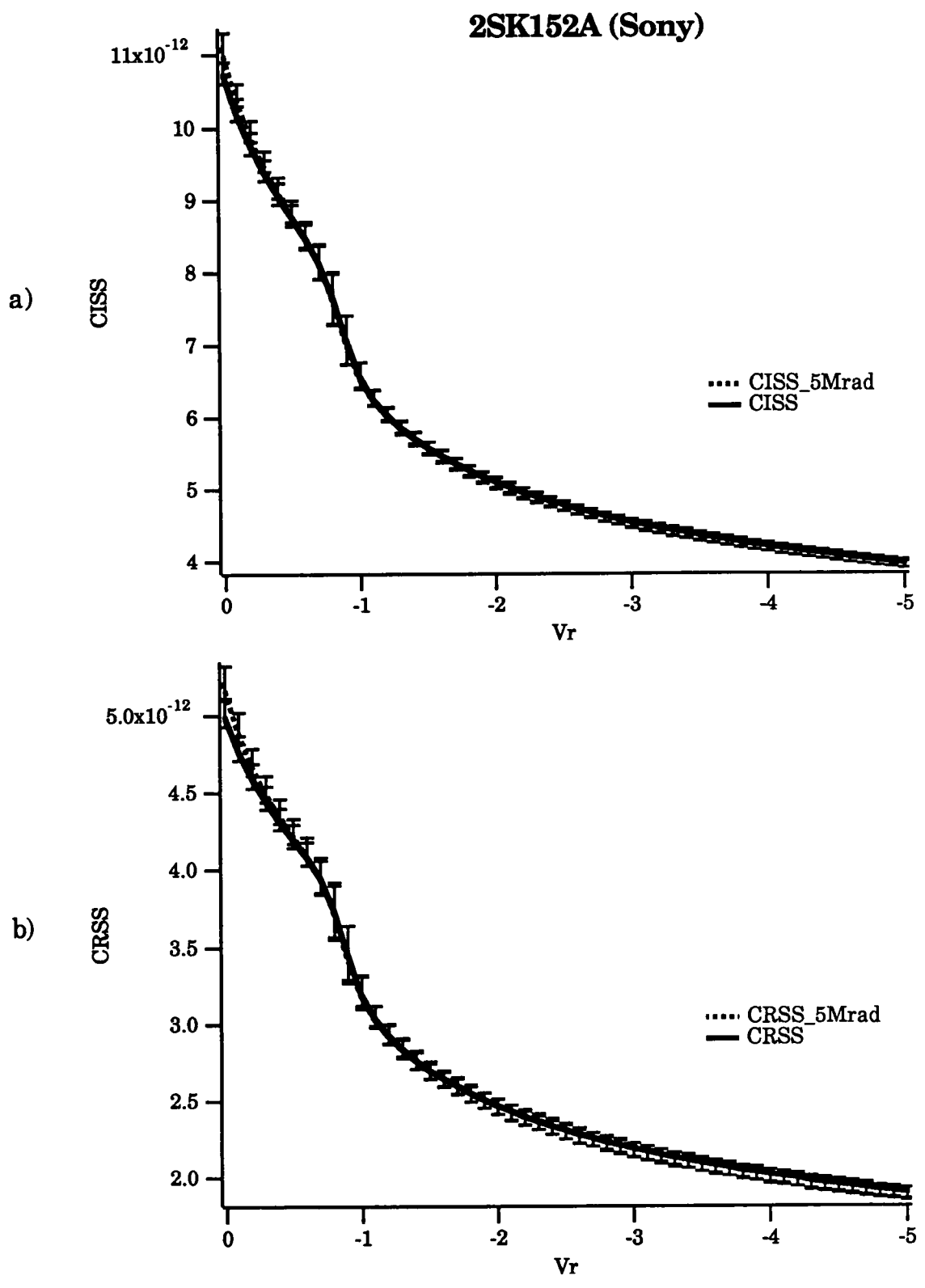


Figure 3.17. a) CISS vs Vr and b) CRSS vs Vr.

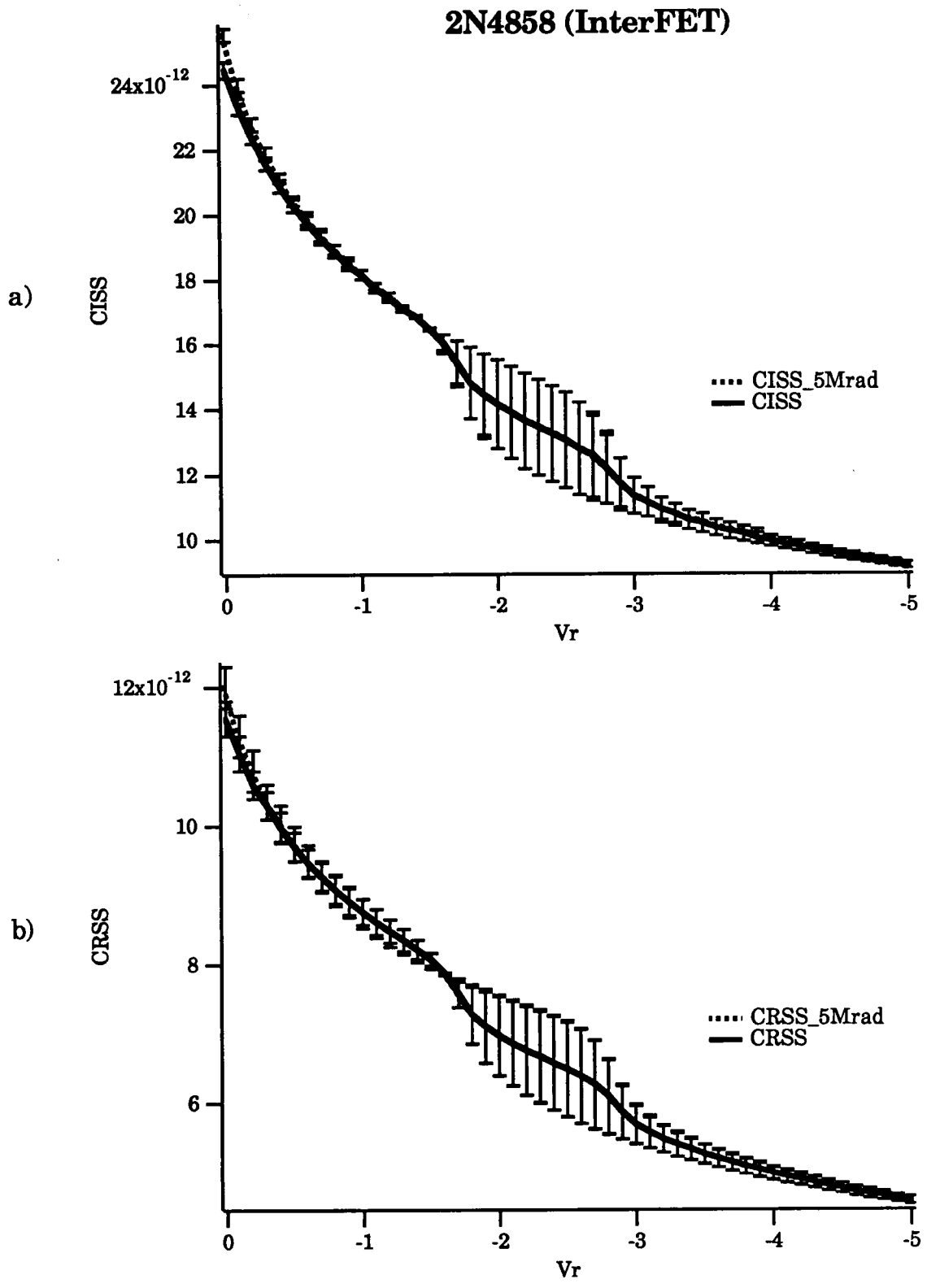


Figure 3.18. a) CISS vs Vr and b) CRSS vs Vr.

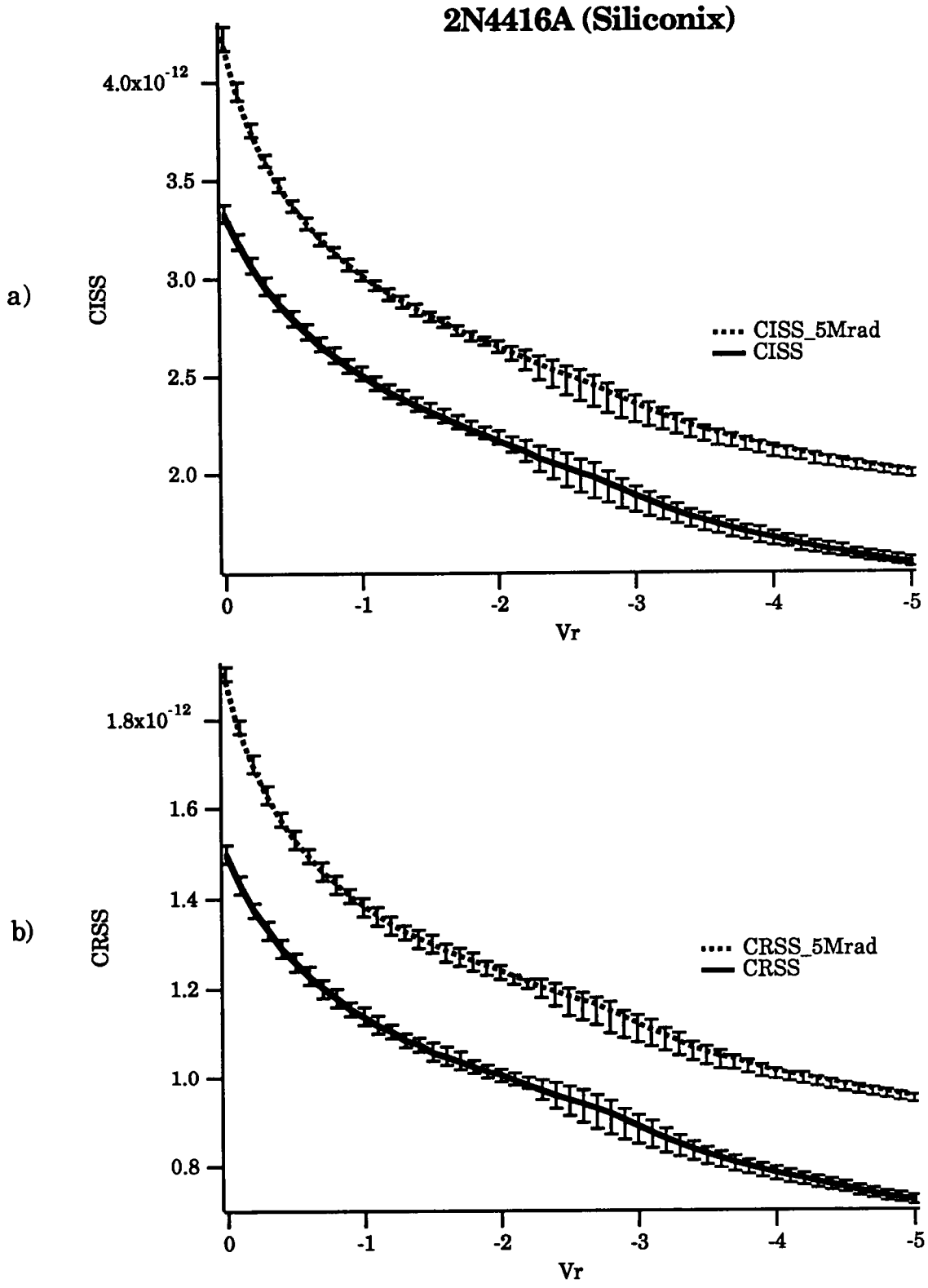


Figure 3.19. a) CISS vs Vr and b) CRSS vs Vr.

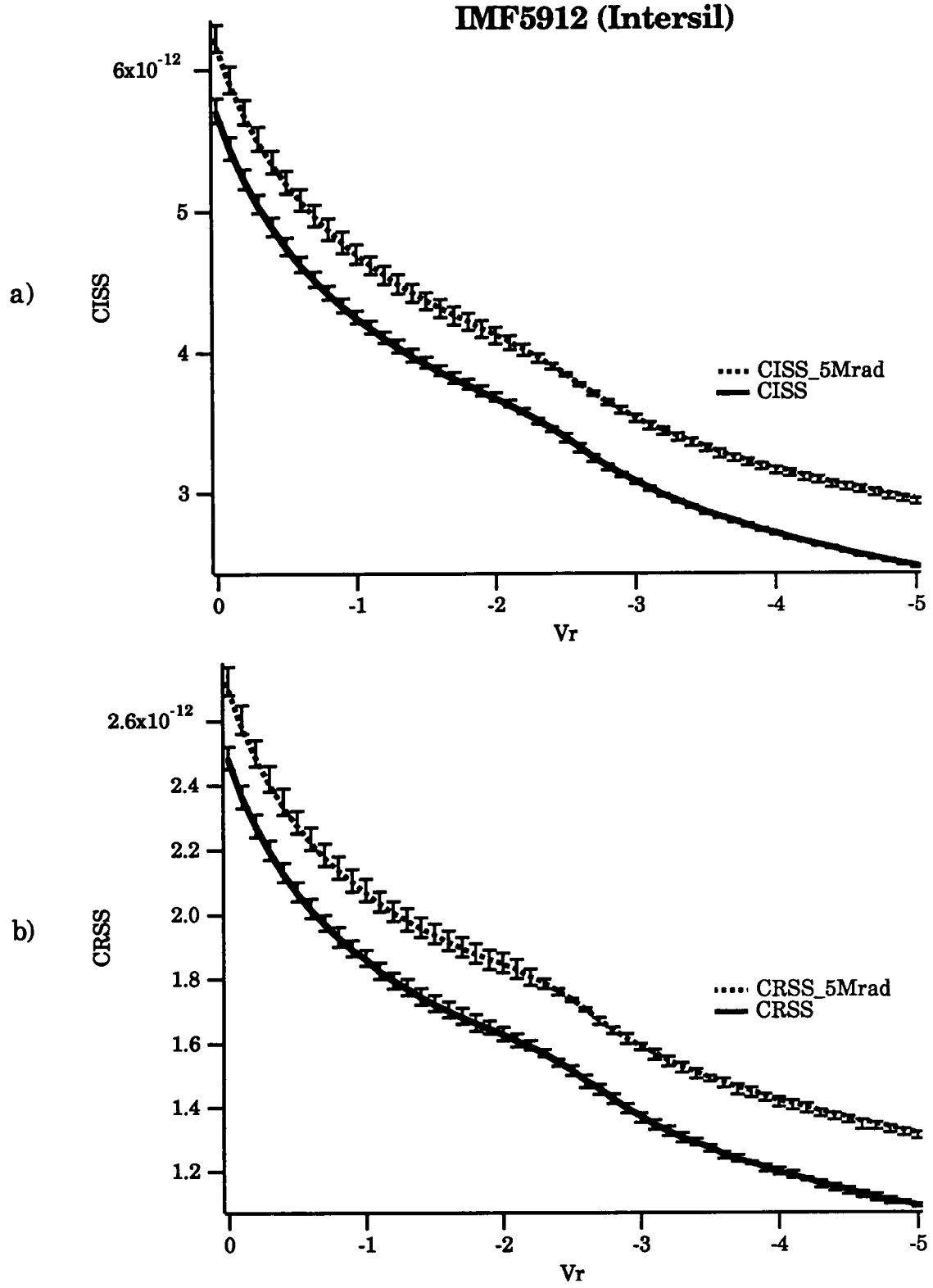


Figure 3.20. a) CISS vs Vr and b) CRSS vs Vr.

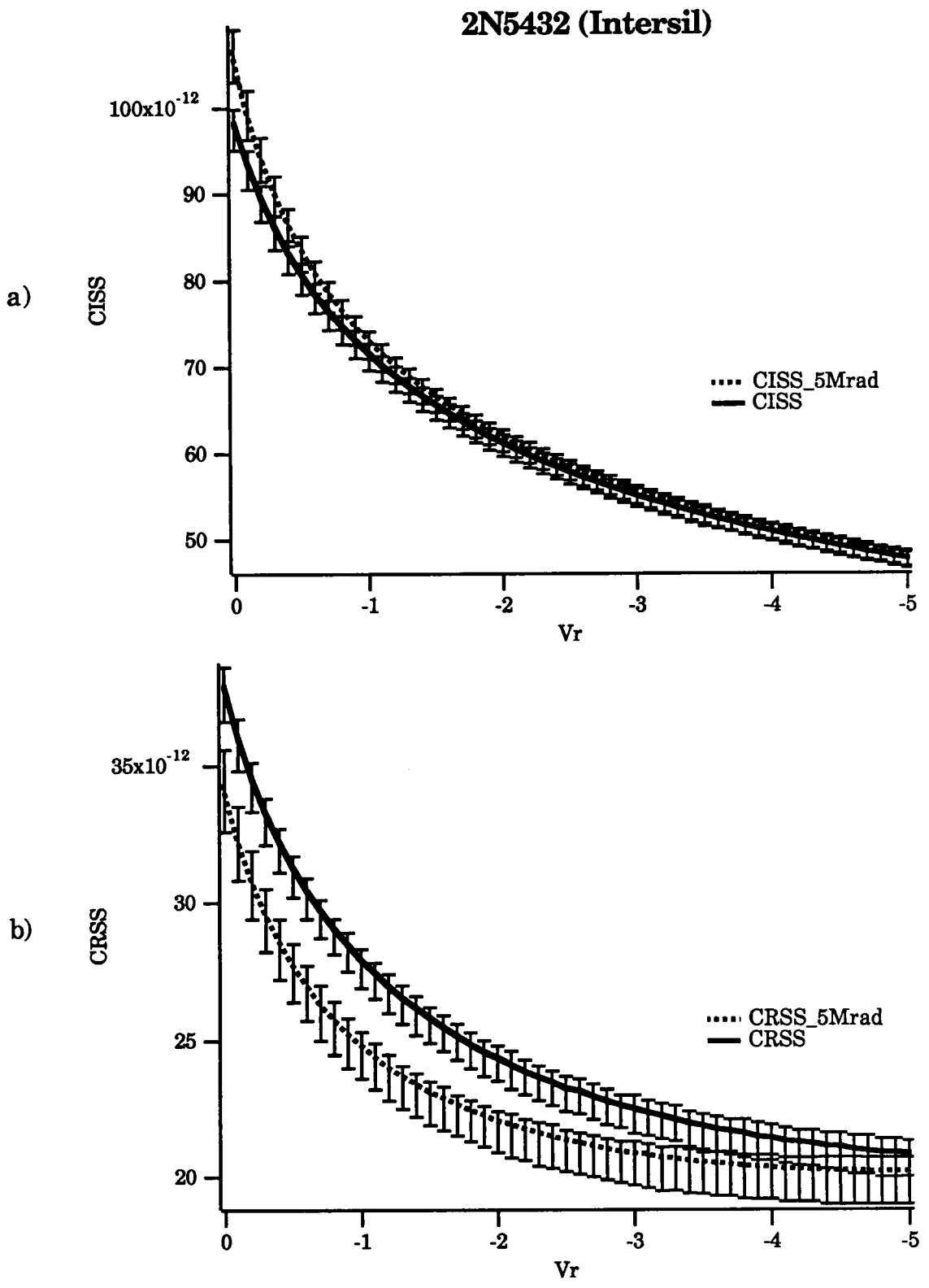


Figure 3.21. a) CISS vs Vr and b) CRSS vs Vr.

3.4 Noise

3.4.1 Definition

The noise characteristics of a JFET can be modeled by the two noise generators S_{IG} and S_{ID} as shown in Figure 3.22 [29].

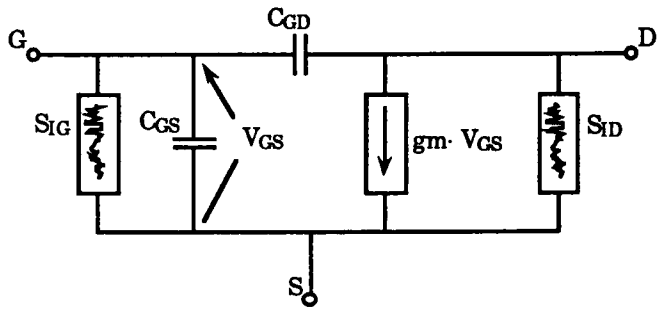


Figure 3.22. JFET noise model.

S_{IG} and S_{ID} are both spectral noise power terms and have dimensions of (power/Hz).

S_{IG} is defined as [30,31]

$$S_{IG} = \underbrace{2 \cdot q \cdot I_G}_{\text{Shot noise}} + \underbrace{\frac{4}{3} k \cdot T \left(C_3 \frac{1}{g_m}\right)\left(2 \cdot \pi \cdot f \cdot C_{GS}\right)^2}_{f^2 \text{ noise}} \tag{3.42}$$

where equation 3.42 is an expression for shot noise as well as a high frequency noise component that is due to fluctuations in the channel

current that are injected via a feedback process through C_{GS} [31]. Shot noise occurs in devices where current flow can be viewed as the sum effect of discrete current pulses. An example of this occurs in a reversed biased junction where the leakage current is composed of discrete electrons and holes crossing the depletion region in a random manner. The shot noise component of S_{IG} is due to the shot noise of the gate current which is generated from the leakage current of the reversed biased junction between the gate and channel material.

S_{ID} is generally defined as [29]

$$S_{ID} = \underbrace{4 \cdot k \cdot T \left(C_3 \cdot g_m\right)}_{\text{Thermal noise}} + \underbrace{C_4 \frac{(I_D)^a}{f^b}}_{\text{Flicker noise}} + \underbrace{C_5 \frac{(I_D)^c}{1 + \left(\frac{f}{f_c}\right)^2}}_{\text{Burst noise}} . \tag{3.43}$$

S_{ID} can be composed of thermal, flicker, and burst noise components.

The thermal noise component is a result of the thermal noise generated from the resistance of the channel. Thermal noise is due to the random thermal motion of the electrons and its magnitude is strictly dependant on temperature [29]. The thermal noise component contains a device dependant parameter C3. C3 typically ranges from 0.6 to 0.7 [30], and was chosen to be equal to 2/3 (0.666) for any theoretical calculations presented in this thesis.

The flicker noise component is believed to be a result of recombination-generation centers in the depletion regions that are adjacent to the conducting channel [32]. A JFET device typically has both flicker and thermal noise as shown in Figure 3.23.

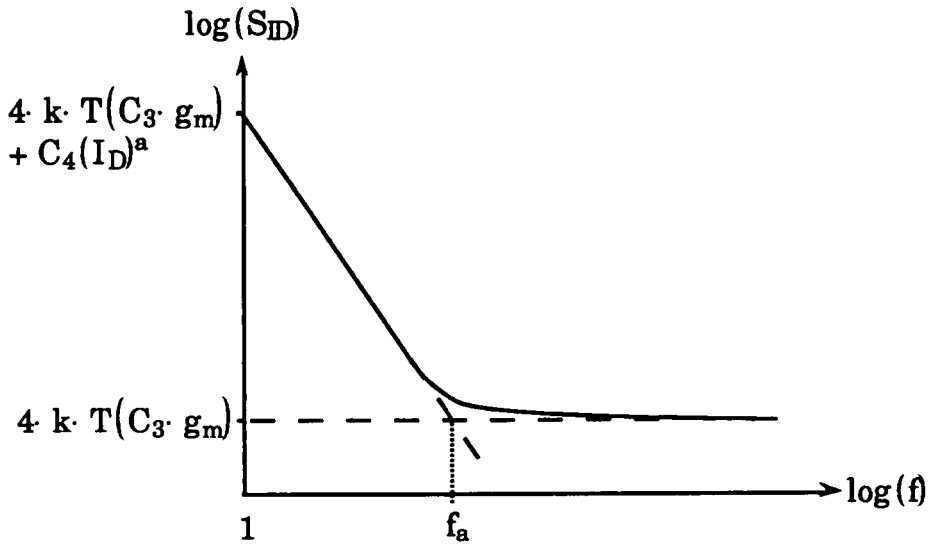


Figure 3.23. Thermal and flicker noise components of S_{ID}.

If the region where the flicker noise component dominates is extrapolated to the value of thermal noise component, the intersection defines the flicker noise corner frequency (f_a) as shown in Figure 3.23 [29]. An expression for f_a can be derived by equating the thermal and flicker noise components as follows. The flicker noise component is

$$S_F = C_4 \frac{(I_D)^a}{f} \quad . \tag{3.44}$$

Taking the logarithm of both sides and rearranging yields

$$\log (S_F) = - \log (f) + \log [C_4 (I_D)^a] \, . \tag{3.45}$$

Given the thermal noise component

$$S_T = 4 \cdot k \cdot T \left(C_3 \cdot g_m\right) \tag{3.46}$$

and taking the logarithm of both sides gives

$$\log\left(S_T\right) = \log\left[4 \cdot k \cdot T \left(C_3 \cdot g_m\right)\right]. \tag{3.47}$$

Equating equation 3.45 with equation 3.47 and defining the frequency where this occurs as f_a

$$-\log\left(f_a\right) + \log\left[C_4 \left(I_D\right)^a\right] = \log\left[4 \cdot k \cdot T \left(C_3 \cdot g_m\right)\right]. \tag{3.48}$$

Solving equation 3.48, f_a can be defined as

$$f_a = \frac{C_4 \left(I_D\right)^a}{4 \cdot k \cdot T \left(C_3 \cdot g_m\right)}. \tag{3.49}$$

At the flicker noise corner frequency the magnitude of the noise can be found by substituting equation 3.49 into

$$S_{ID}^{'} = 4 \cdot k \cdot T \left(C_3 \cdot g_m\right) + C_4 \frac{\left(I_D\right)^a}{f} \tag{3.50}$$

which yields

$$S_{ID}^{'} = 2\left[4 \cdot k \cdot T \left(C_3 \cdot g_m\right)\right]. \tag{3.51}$$

Thus at the defined noise corner frequency (f_a) the noise spectral power is twice the value of the thermal noise component.

Burst noise is attributed to heavy-metal ion contamination [29] and may also be due to localized microplasmas in the junctions [33]. A spectral plot of this noise component is shown in Figure 3.24.

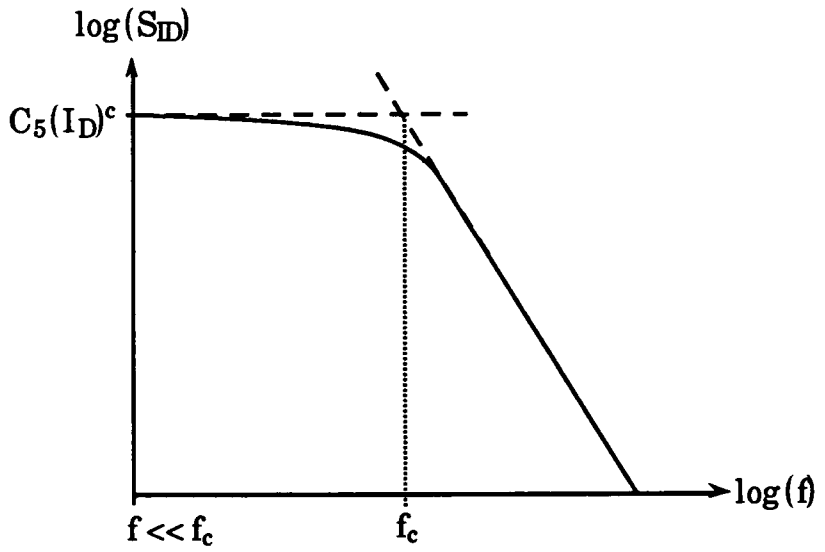


Figure 3.24. Burst noise component of S_{ID}.

A device can have multiple burst noise components each having its own magnitude and frequency (f_c).

S_{ID} is often related to the equivalent noise that would be generated by a resistor in series with the gate of the JFET, as shown in Figure 3.25.

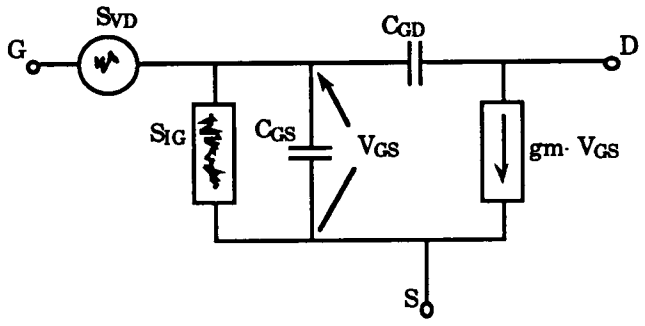


Figure 3.25. Modified JFET noise model.

Equation 3.43 can be reflected to the input (S_{VD}) as

$$S_{VD} = 4\cdot k\cdot T\left(C_3\frac{1}{g_m}\right) + C_4\frac{(I_D)^a}{(g_m)^2}\frac{1}{f^b} + \frac{C_5}{(g_m)^2}\frac{(I_D)^c}{1+\left(\frac{f}{f_c}\right)^2}. \tag{3.52}$$

For measurement purposes S_{VD} is normally evaluated as a noise resistance, where for a resistor

$$S_{VR} = 4\cdot k\cdot T\cdot R \;\Rightarrow\; R = \frac{S_{VR}}{4\cdot k\cdot T}. \tag{3.53}$$

Thus using equation 3.53, equation 3.52 can be expressed as

$$R_n = C_3\frac{1}{g_m} + \frac{C_4}{4\cdot k\cdot T}\frac{(I_D)^a}{(g_m)^2}\frac{1}{f^b} + \frac{C_5}{4\cdot k\cdot T\,(g_m)^2}\frac{(I_D)^c}{1+\left(\frac{f}{f_c}\right)^2}. \tag{3.54}$$

To simplify the evaluation of the noise measurements, the constants can be grouped and an extra burst noise component added as shown below.

$$R_n = C_3 \frac{1}{g_m} + \frac{C_6}{f} + \frac{C_7}{1+\left(\frac{f}{f_7}\right)^2} + \frac{C_8}{1+\left(\frac{f}{f_8}\right)^2} \tag{3.55}$$

Making the proper changes to equation 3.49, the corner frequency for the flicker noise component can be written as

$$f_a = \frac{C_6}{C_3\left(\frac{1}{g_m}\right)}. \tag{3.56}$$

As an illustration, a noise spectrum containing all the components of equation 3.55 is shown in Figure 3.26.

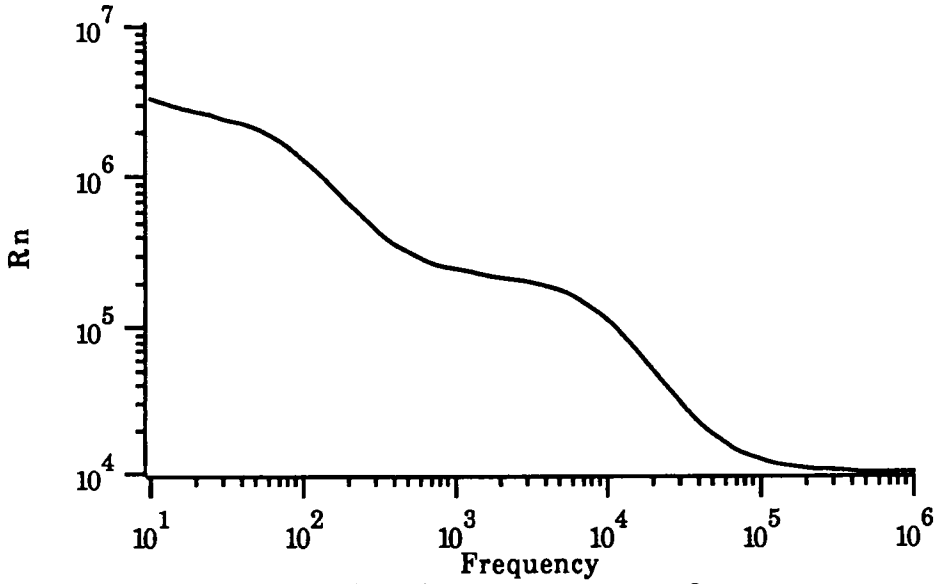


Figure 3.26. Plot of equation 3.55 vs frequency.

where

$$C_3 \frac{1}{g_m} = 10K\Omega$$

$$C_6 = 10M\Omega$$

$$C_7 = 2M\Omega$$
$$f_7 = 100Hz$$

$$C_8 = 200K\Omega$$
$$f_8 = 10KHz\,.$$

It is interesting to note that the noise corner frequency (f_a) occurs at 1KHz. The noise corner frequency accounts only for the flicker noise component and is unaffected by the burst noise components. For Figure 3.26 it can be seen that f_a based only on the flicker noise component does not show the true value where the noise power has increased to twice the thermal value. Since this would be useful information for the circuit designer, an extra parameter f_n is defined as the frequency at which the noise power spectrum is twice the thermal noise component.

The parameters of equation 3.55 could be estimated from a plot of R_n but curve fitting was used to obtain more accurate values.

3.4.2 Radiation Effects

For the gamma radiated device, the generation-recombination mechanisms that generate low frequency noise in unirradiated devices are increased due to ionization damage. The dominant effects are an increase

in flicker noise and the creation (or intensification) of burst noise components.

3.4.3 Measurements

The following noise resistance spectrum plots (Figures 3.27 - 3.34) were obtained from the noise measurement system described in appendix A. As in the capacitance curves, error bars for each device indicate the range (minimum, maximum) of data at each frequency. For I_D = 10uA the theoretical value of R_n at higher frequencies was greater than the measured value of R_n. It may be that the present noise theories derived for quadratic operation do not apply in the subthreshold region (which for a drain current of 10uA, all the JFETs were in the subthreshold region of operation).

Tables 3.12 through 3.15 are a summary of the parameters of equation 3.55.

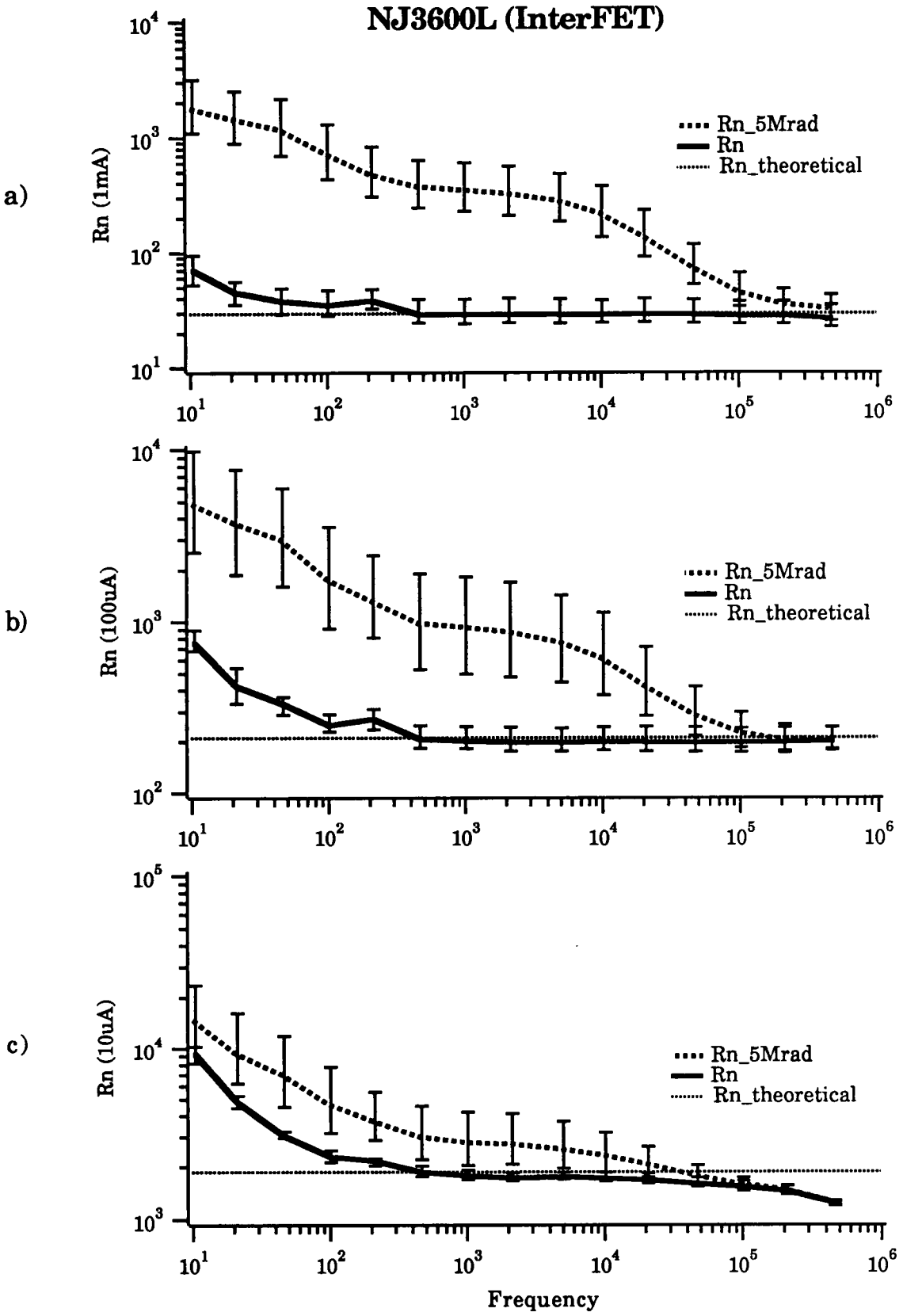


Figure 3.27. Rn vs frequency for Id equal a) 1mA, b) 100uA, and c) 10uA.

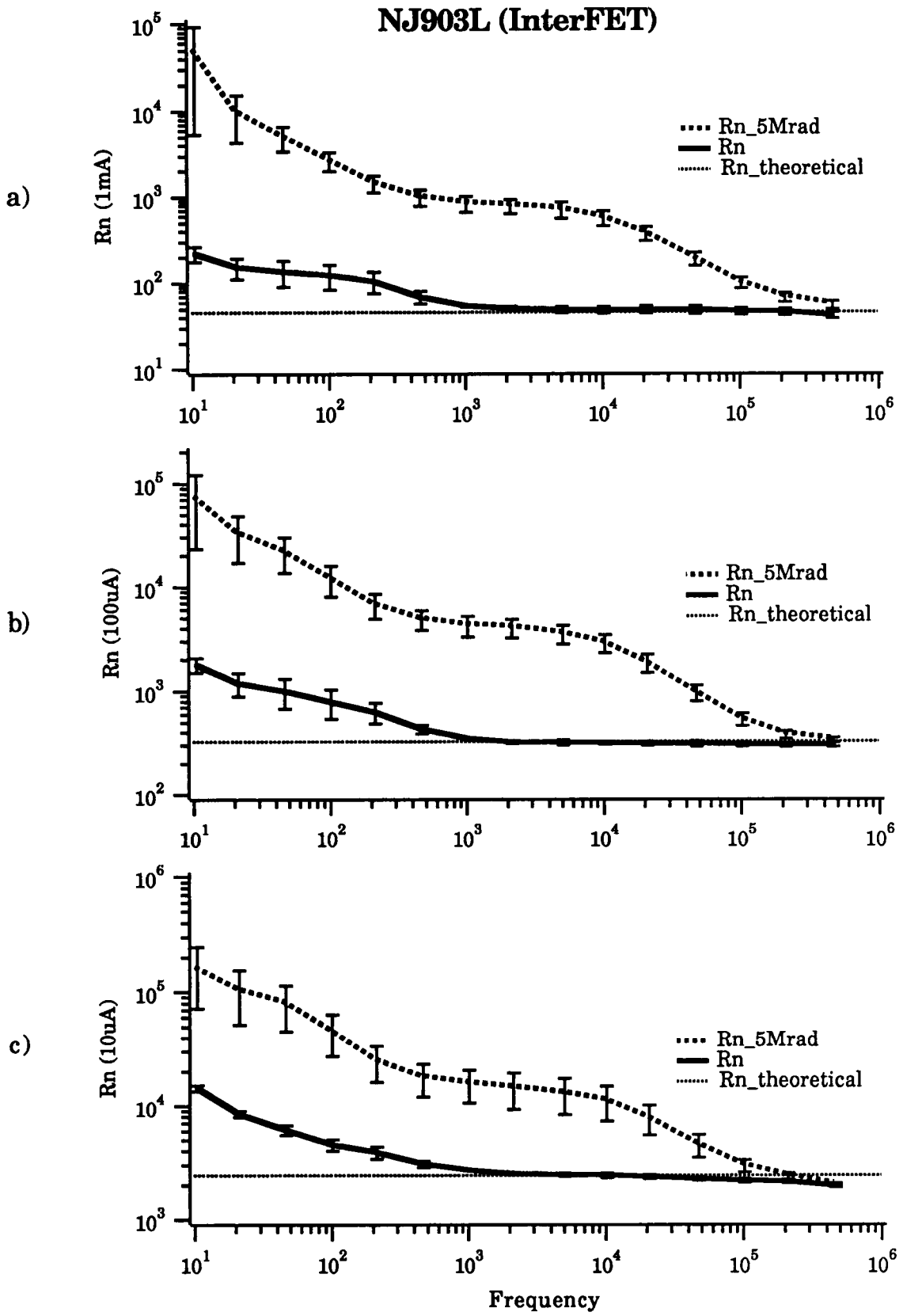


Figure 3.28. Rn vs frequency for Id equal a) 1mA, b) 100uA, and c) 10uA.

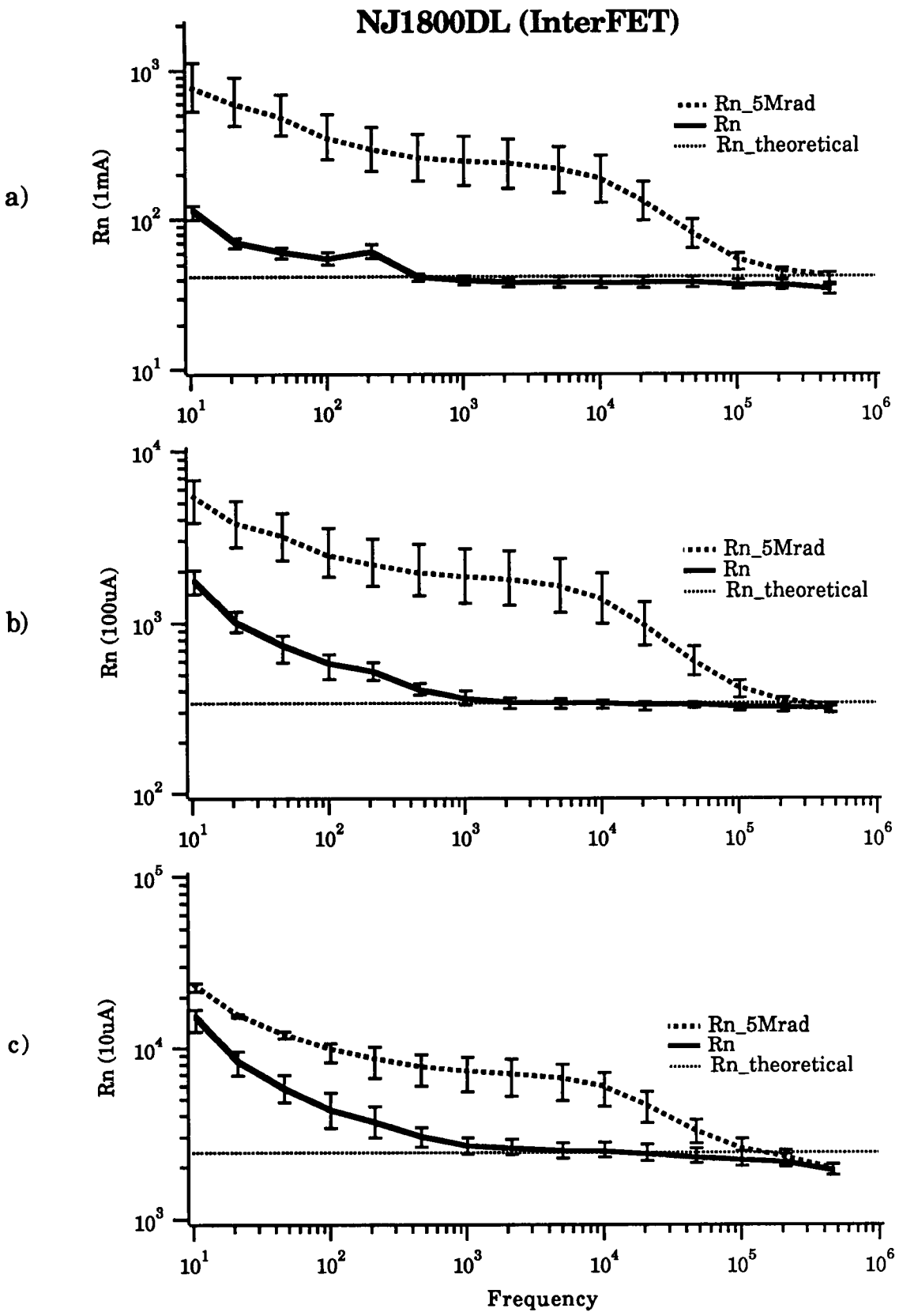


Figure 3.29. Rn vs frequency for Id equal a) 1mA, b) 100uA, and c) 10uA.

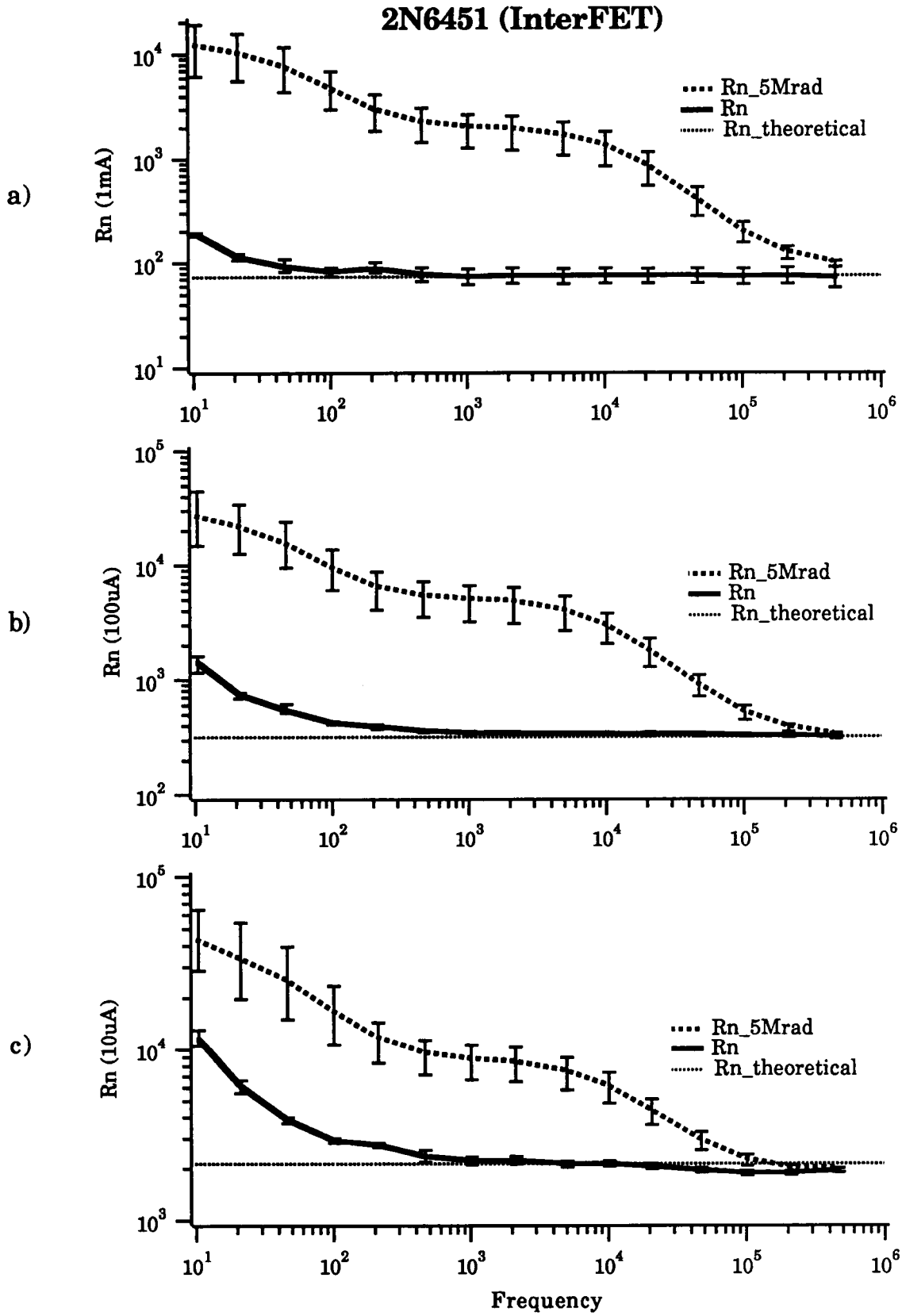


Figure 3.30. Rn vs frequency for Id equal a) 1mA, b) 100uA, and c) 10uA.

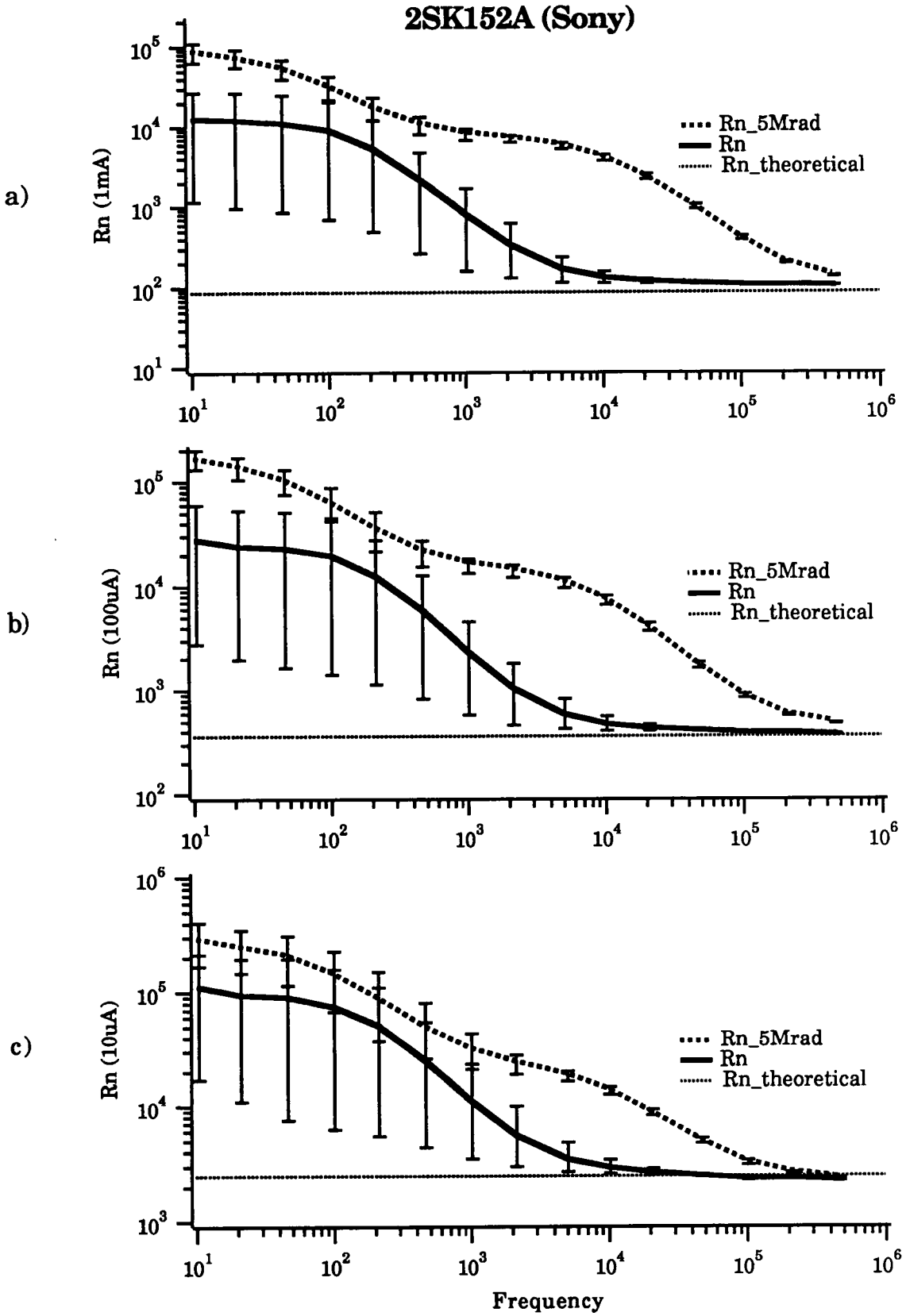


Figure 3.31. Rn vs frequency for Id equal a) 1mA, b) 100uA, and c) 10uA.

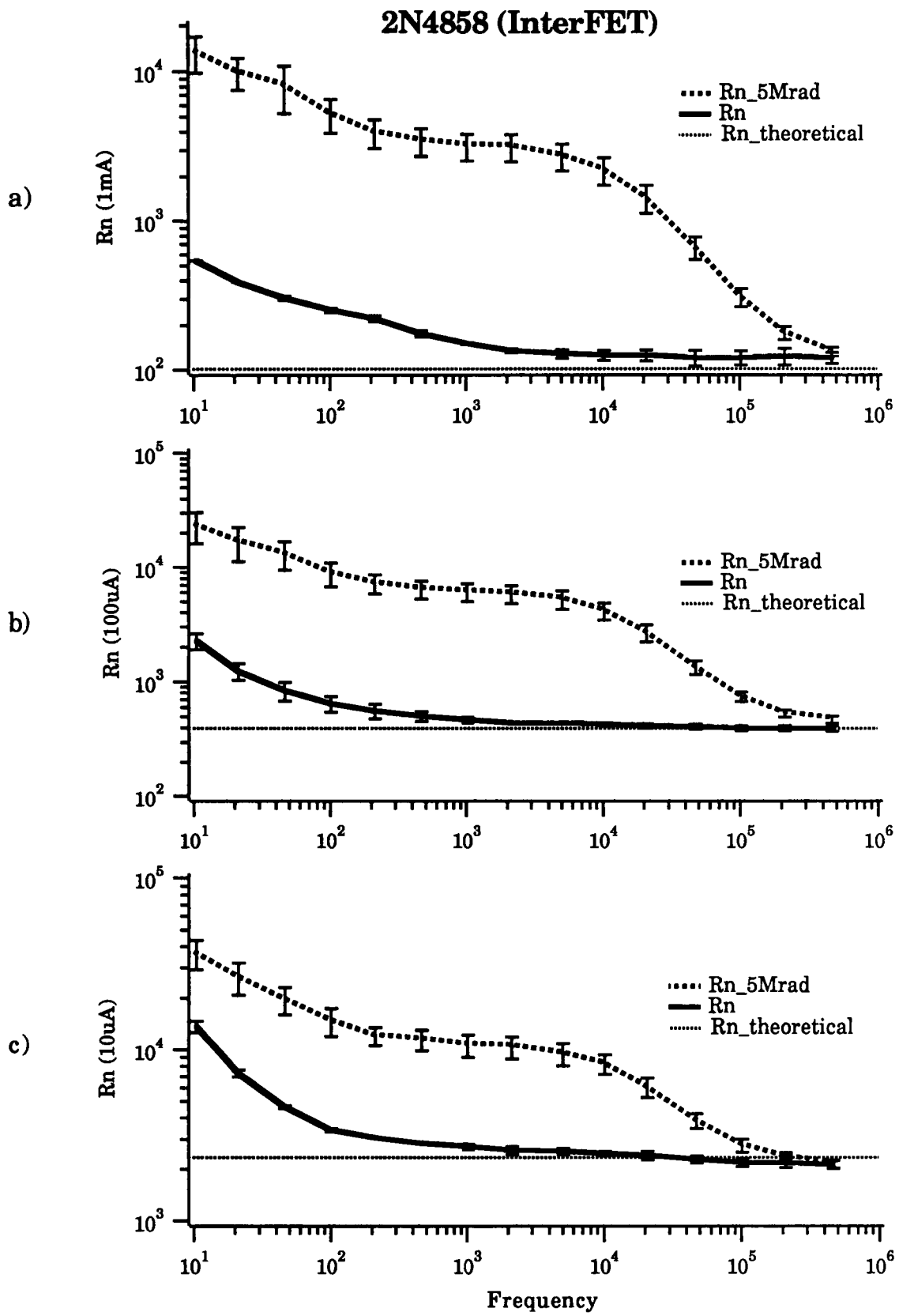


Figure 3.32. Rn vs frequency for Id equal a) 1mA, b) 100uA, and c) 10uA.

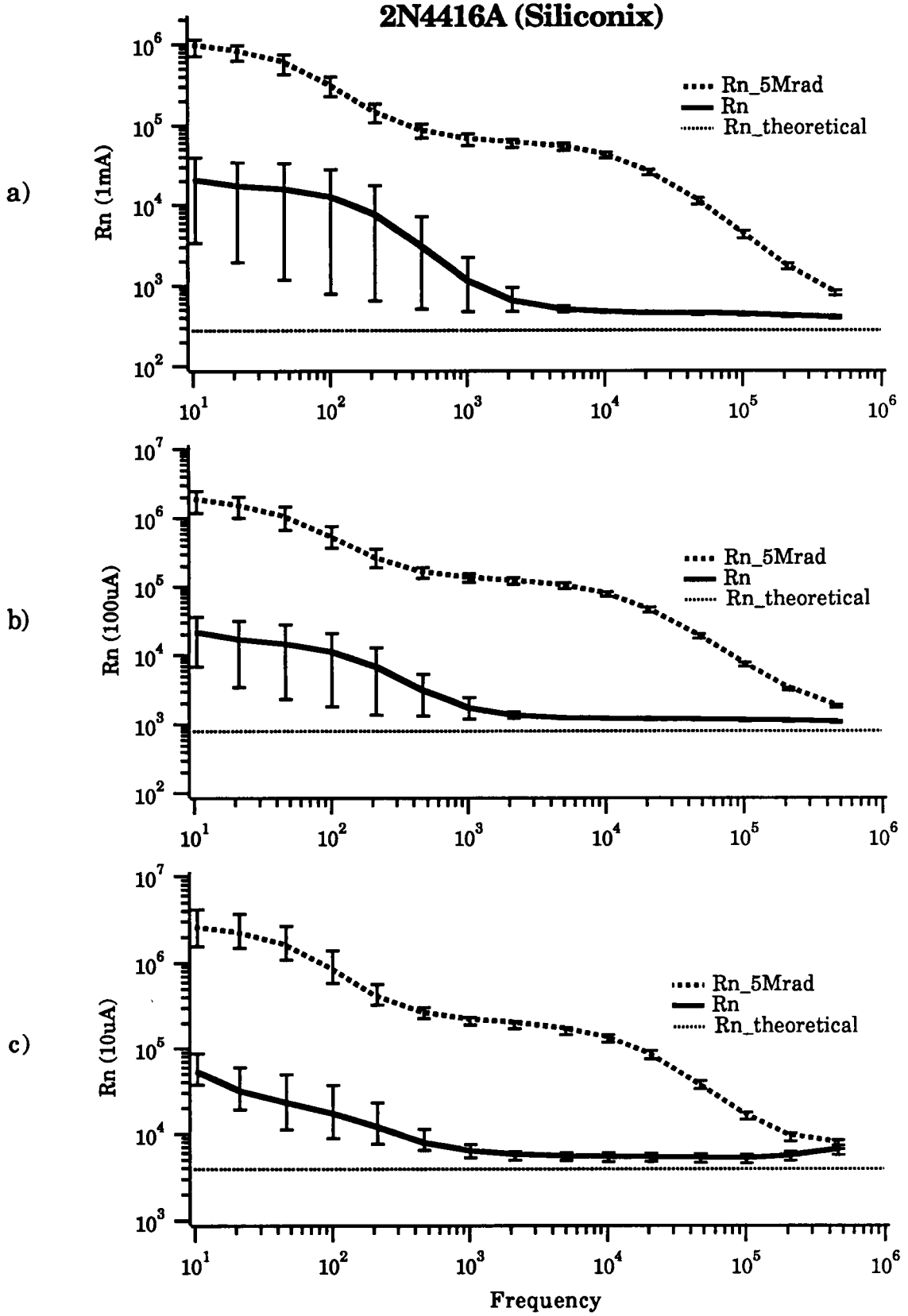


Figure 3.33. Rn vs frequency for Id equal a) 1mA, b) 100uA, and c) 10uA.

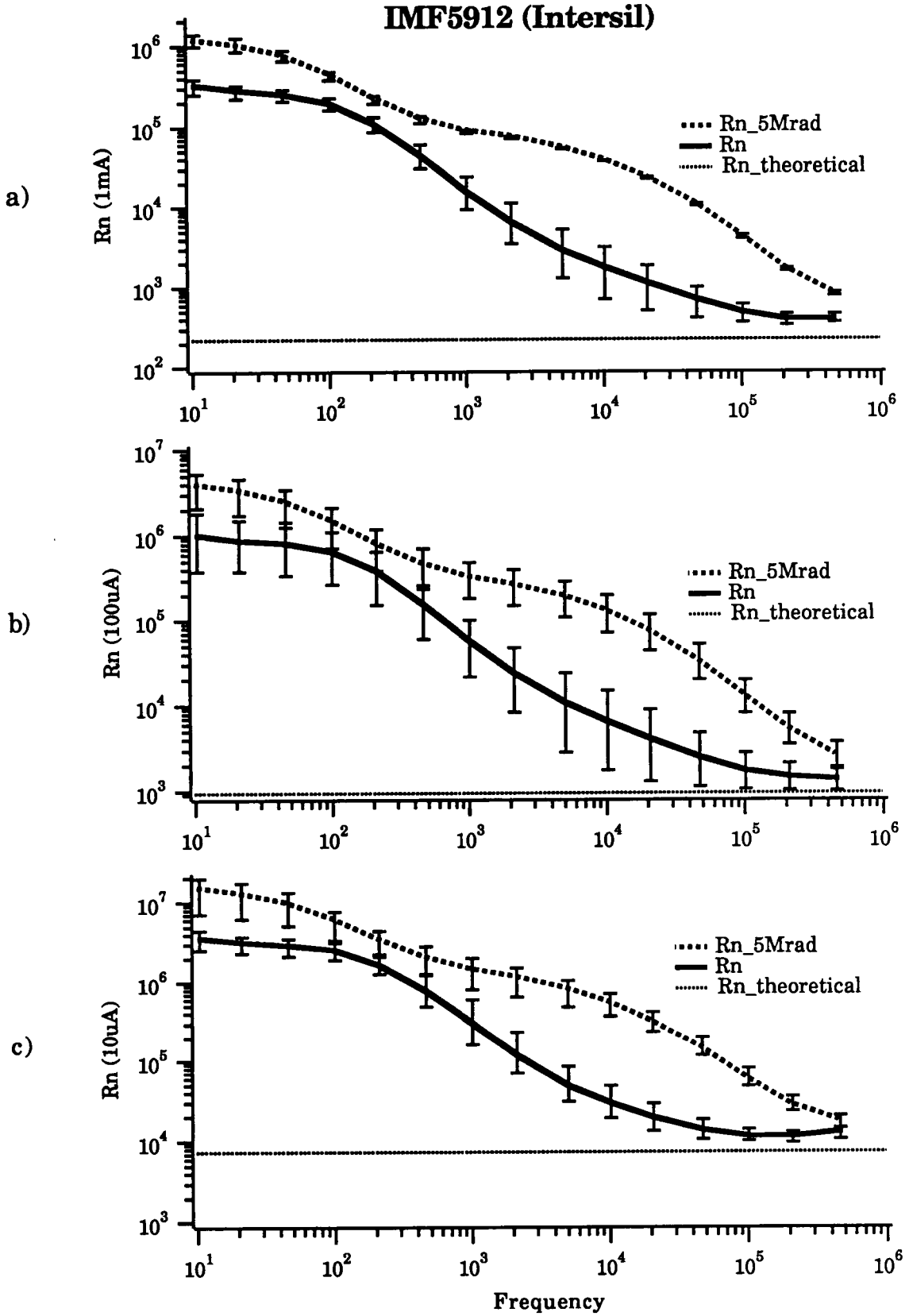


Figure 3.34. Rn vs frequency for Id equal a) 1mA, b) 100uA, and c) 10uA.

Table 3.12. Summary of noise measurements.

	I_D = 1mA			I_D = 100uA			I_D = 10uA		
Part	**Rn (midband)**	**Pre-rad f_n**	**Post-rad f_n**	**Rn (midband)**	**Pre-rad f_n**	**Post-rad f_n**	**Rn (midband)**	**Pre-rad f_n**	**Post-rad f_n**
NJ3600L	28.6	12	67K	197	23	21K	1.70K	37	280
NJ903L	48.5	250	110K	310	220	89K	2.17K	130	52K
NJ1800DL	37.8	21	52K	331	70	40K	2.41K	81	18K
2N6451	74.4	11	140K	336	25	73K	2.05K	42	21K
2SK152A	105	3.5K	190K	380	3.6K	130K	2.27K	3.0K	50K
2N4858	121	110	140K	394	58	95K	2.17K	57	37K
2N4416A	450	1.4K	400K	1.18K	710	300K	5.31K	300	180K
IMF5912	387	40K	500K	1.30K	49K	460K	11.2K	17K	280K

Table 3.13. Summary of noise components for Id = 1mA.

	Pre-radiation							Post-radiation					
Part	C_3	C_6	f_a	C_7	f_7	C_8	f_8	C_6	f_a	C_7	f_7	C_8	f_8
NJ3600L	.664	350	12					12K	410	950	60	270	16K
NJ903L	.728	900	19	70	300			170K	3.5K			650	22K
NJ1800DL	.612	630	17	6	330			2.7K	71	250	90	190	22K
2N6451	.698	800	11					38K	510	6.0K	90	1.8K	20K
2SK152A	.836	17K	160	11K	200	60	9.0K	300K	2.8K	50K	100	6.0K	18K
2N4858	.810	3.3K	27	95	400	10	6.0K	50K	410	5.0K	70	3K	20K
2N4416A	1.13	45K	100	15K	200			5M	11K	500K	80	50K	25K
IMF5912	1.21	900K	2.3K	230K	230	1.9K	18K	3M	7.7K	800K	120	50K	23K

Table 3.14. Summary of noise components for Id = 100uA.

	Pre-radiation							Post-radiation					
Part	C_3	C_6	f_a	C_7	f_7	C_8	f_8	C_6	f_a	C_7	f_7	C_8	f_8
NJ3600L	.634	4.6K	23					20K	98	2.3K	80	650	15K
NJ903L	.654	11K	36	450	250			650K	2.1K			3.2K	22K
NJ1800DL	.662	12K	36	120	350			28K	83	750	100	1.4K	20K
2N6451	.722	8.5K	25					85K	250	12K	80	4.3K	16K
2SK152A	.722	60K	160	22K	240	270	7.0K	500K	1.3K	100K	110	12K	16K
2N4858	.678	17K	43	55	800	35	30K	125K	317	6K	70	5.3K	20K
2N4416A	1.02	70K	60	12K	180			13M	11K	900K	65	100K	21K
IMF5912	.944	2.7M	2.1K	800K	230	7.5K	16K	12M	9.2K	2.5M	120	200K	22K

Table 3.15. Summary of noise components for Id = 10uA.

	Pre-radiation							Post-radiation					
Part	C_3	C_6	f_a	C_7	f_7	C_8	f_8	C_6	f_a	C_7	f_7	C_8	f_8
NJ3600L	.617	63K	37					63K	37	3.8K	80	900	15K
NJ903L	.612	110K	51	1.3K	250	270	20K	900K	420	50K	90	12K	22K
NJ1800DL	.674	110K	46	1.0K	350			140K	57	2.1K	180	4.3K	20K
2N6451	.652	85K	42					150K	73	17K	90	6.2K	16K
2SK152A	.629	300K	132	80K	240	2.5K	5K	800K	350	180K	180	19K	16K
2N4858	.625	100K	46	150	3K	300	35K	200K	92	6K	80	8.2K	21K
2N4416A	.934	320K	60	12K	190			12M	2.3K	1.9M	65	170K	20K
IMF5912	1.05	10M	893	2.7M	290	39K	9K	40M	3.4K	9.5M	20	900K	19K

CHAPTER 4

BIPOLAR TRANSISTORS

4.1 Introduction

Bipolar transistors are generally less resistant to radiation damage than JFET's. Ionization damage due to gamma radiation mainly affects the current gain (Beta or h_{FE}) of bipolar transistors. Also, there is typically a slight increase in both junction capacitances, as well as a slight decrease in the gain bandwidth product (f_T).

4.2 DC Characteristics

The complete Gummel model for a bipolar transistor is illustrated in Figure 4.1 [21]

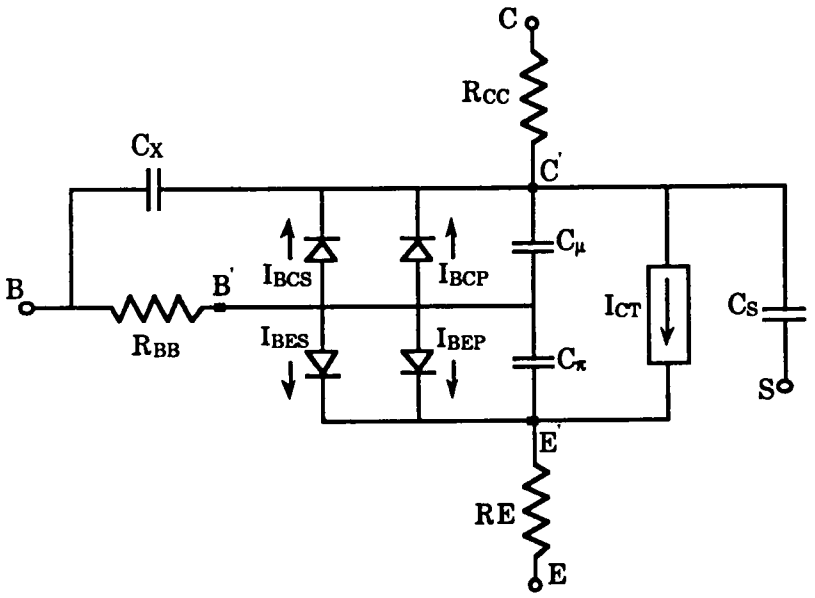


Figure 4.1. Gummel model for the bipolar transistor.

where

$$I_{CT} = \frac{IS}{QB}\left[\exp\left(\frac{V_{B'E'}}{NF \cdot V_T}\right) - \exp\left(\frac{V_{B'C'}}{NR \cdot V_T}\right)\right] \tag{4.1}$$

$$I_{BEP} = \frac{IS}{BF}\left[\exp\left(\frac{V_{B'E'}}{NF \cdot V_T}\right) - 1\right] \tag{4.2}$$

$$I_{BES} = C2 \cdot IS\left[\exp\left(\frac{V_{B'E'}}{NEL \cdot V_T}\right) - 1\right] \tag{4.3}$$

$$I_{BCP} = \frac{IS}{BR}\left[\exp\left(\frac{V_{B'C'}}{NR \cdot V_T}\right) - 1\right] \tag{4.4}$$

$$I_{BCS} = C4 \cdot IS\left[\exp\left(\frac{V_{B'C'}}{NCL \cdot V_T}\right) - 1\right] \tag{4.5}$$

$$QB = \frac{Q1}{2}\left(1 + \sqrt{1 + 4 \cdot Q2}\right) \tag{4.6}$$

$$Q1 = \frac{1}{1 - \frac{V_{B'C'}}{VA} - \frac{V_{B'E'}}{VB}} \tag{4.7}$$

$$Q2 = \frac{IS}{IK}\left[\exp\left(\frac{V_{B'E'}}{NF \cdot V_T}\right) - 1\right] + \frac{IS}{IKR}\left[\exp\left(\frac{V_{B'C'}}{NR \cdot V_T}\right) - 1\right] \tag{4.8}$$

IS = saturation current
NF = forward emission coefficient
NR = reverse current emission coefficient
BF = ideal forward current gain
BR = ideal reverse current gain
C2 = forward low-current non-ideal base current coefficient
C4 = reverse low-current non-ideal base current coefficient
NEL = nonideal low-current base-emitter emission coefficient
NCL = nonideal low-current base-collector emission coefficient
VA = forward Early voltage
VR = reverse Early voltage
IK = forward high-current knee current for beta roll-off
IKR = reverse high-current knee current for beta roll-off .

This model can be simplified by assuming the transistor is being operated with the base to collector junction reverse biased and the base to emitter junction forward biased (normal operation) in which case:

$$I_{CT} = \frac{IS}{QB}\exp\left(\frac{V_{B'E'}}{NF \cdot V_T}\right) \tag{4.9}$$

$$I_{BEP} = \frac{IS}{BF}\left[\exp\left(\frac{V_{B'E'}}{NF \cdot V_T}\right) - 1\right] \tag{4.10}$$

$$I_{BES} = C2 \cdot IS\left[\exp\left(\frac{V_{B'E'}}{NEL \cdot V_T}\right) - 1\right] \tag{4.11}$$

$$I_{BCP} = -\frac{IS}{BR} \tag{4.12}$$

$$I_{BCS} = -C4 \cdot IS \tag{4.13}$$

$$QB = \frac{Q1}{2}\left(1 + \sqrt{1 + 4 \cdot Q2}\right) \tag{4.14}$$

$$Q1 = \frac{1}{1 - \frac{V_{B'C'}}{VA} - \frac{V_{B'E'}}{VB}} \tag{4.15}$$

$$Q2 = \frac{IS}{IK}\left[\exp\left(\frac{V_{B'E'}}{NF \cdot V_T}\right) - 1\right] - \frac{IS}{IKR}. \tag{4.16}$$

4.2.1 Beta

The beta (often referred to as h_{FE} on manufacturer's data sheets) of a bipolar transistor is defined simply as the ratio of the dc collector current to the dc base current for a fixed value of V_{CE}.

$$\text{Beta} = \left.\frac{I_C}{I_B}\right|_{V_{CE}}$$

Beta has a current dependency that can be divided into three regions [29] as shown in Figure 4.2.

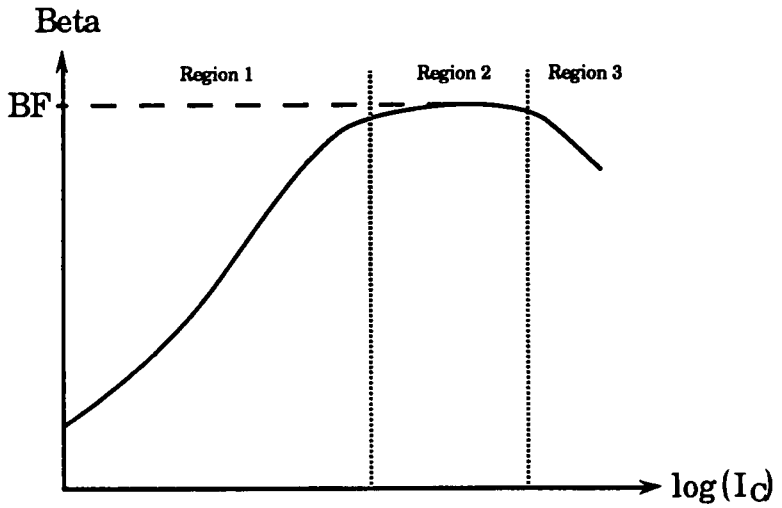


Figure 4.2. Beta vs log (I_C).

In region 2 beta is relatively constant and reaches a maximum value that can be defined as [29]

$$BF = \frac{1}{\frac{(W_B)^2}{2 \cdot \tau_b \cdot D_n} + \frac{D_p \cdot W_B \cdot N_a}{D_n \cdot L_p \cdot N_d}} \tag{4.17}$$

where

W_B = effective base width
τ_b = effective minority-carrier lifetime in the base
D_n = diffusion constant for electrons
D_p = diffusion constant for holes
$N_a = \frac{\text{number of acceptors}}{cm^3}$
$N_d = \frac{\text{number of donors}}{cm^3}$
L_p = diffusion length for holes in the emitter .

In region 2 the base current is dominated by equation 4.10 where the exponential term is much greater than -1 and can thus be written as

$$I_B = \frac{IS}{BF} \exp\left(\frac{V_{B'E'}}{NF \cdot V_T}\right) \tag{4.18}$$

The collector current in this region is defined by equation 4.9 and with QB = 1 can be expressed as

$$I_C = IS \exp\left(\frac{V_{B'E'}}{NF \cdot V_T}\right). \tag{4.19}$$

In region 1 the collector current follows equation 4.19 whereas the current generated due to the recombination of carriers in the base-emitter depletion region becomes an important component of I_B. This current is defined by equation 4.11.

$$I_{BES} = C2 \cdot IS\left[\exp\left(\frac{V_{B'E'}}{NEL \cdot V_T}\right) - 1\right] \approx C2 \cdot IS \exp\left(\frac{V_{B'E'}}{NEL \cdot V_T}\right) \tag{4.20}$$

where NEL is on the order of two. Thus the base current in region 1 is

$$I_B = \frac{IS}{BF} \exp\left(\frac{V_{B'E'}}{NF \cdot V_T} - 1\right) + C2 \cdot IS \exp\left(\frac{V_{B'E'}}{NEL \cdot V_T}\right). \tag{4.21}$$

For low values of collector current the recombination current dominates and I_B can be written as

$$I_B = C2 \cdot IS \exp\left(\frac{V_{B'E'}}{NEL \cdot V_T}\right). \tag{4.22}$$

Using the definition of beta and combining equations 4.19 and 4.22, beta for low values of collector current can be defined as

$$Beta = \frac{1}{C2} \exp\left[\frac{V_{B'E'}}{V_T}\left(\frac{1}{NF} - \frac{1}{NEL}\right)\right]. \tag{4.23}$$

Removing the exponential using equation 4.19 and allowing NF = 1 and NEL = 2 yields

$$Beta = \left(\frac{1}{C2\sqrt{I_S}}\right)\sqrt{I_C}. \tag{4.24}$$

Thus in region 1 beta is proportional to the square root of the collector current.

In region 3 the main change in beta can be attributed to a change in I_C due to the increasing significance of minority carriers injected into the base region. This causes a change in the collector current since an equal

number of majority carriers from the collector region are required to maintain charge neutrality in the base region [34]. At high levels of collector current I_C can be expressed as [29]

$$I_C = I_{SH} \exp\left(\frac{V_{BE}}{2 \cdot V_T}\right). \tag{4.25}$$

The base current can change due to the internal base resistance, but the amount of change is assumed negligible for this analysis. Thus applying the definition of beta to equation 4.25 and equation 4.18 yields

$$\text{Beta} = \frac{I_{SH}}{IS}\, BF \cdot \exp\left(-\frac{V_{BE}}{2 \cdot V_T}\right). \tag{4.26}$$

Beta can then be expressed in terms of the collector current by replacing the exponential with equation 4.25.

$$\text{Beta} = \frac{(I_{SH})^2}{IS}\, BF\, \frac{1}{I_C} \tag{4.27}$$

From this equation it can be seen that beta decreases significantly with increasing collector current. Beta can also decrease in region 3 due to a current density limitation caused by the finite emitter perimeter [14].

4.2.1.1 Measurement Theory

The beta of all transistors was measured as a function of the logarithm of the collector current using the Hewlett Packard semiconductor parameter analyzer. Typical plots would be similar to Figure 4.2 which was presented at the beginning of section 4.2.1.

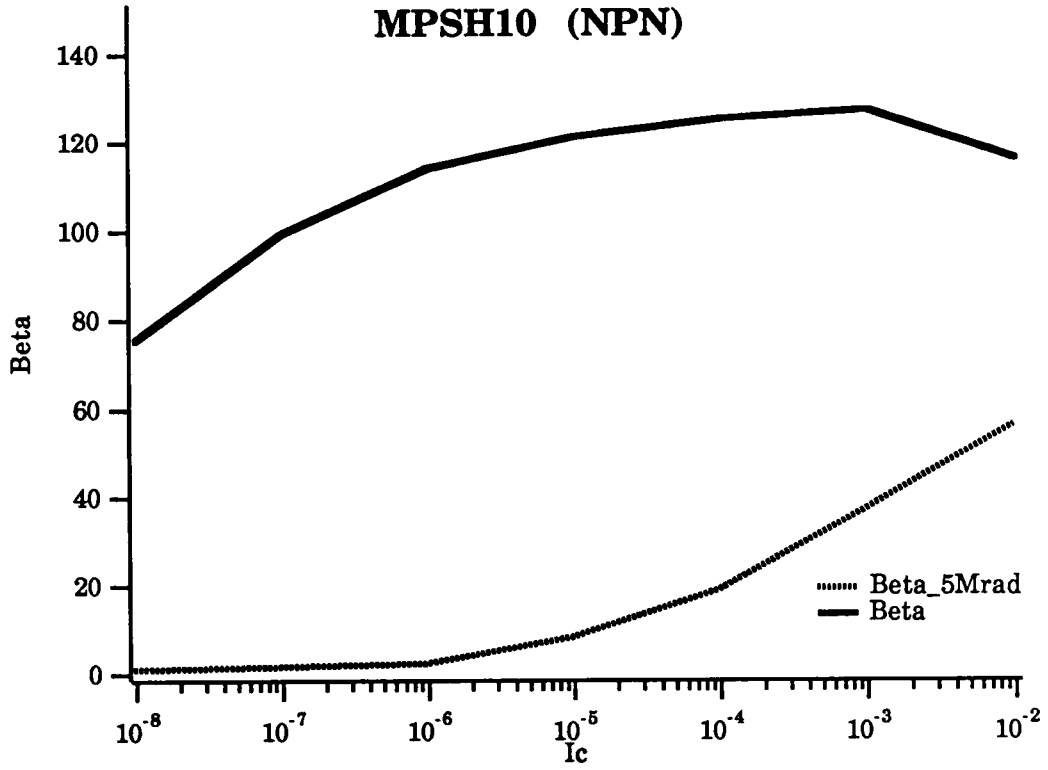
4.2.1.2 Radiation Effects

The beta of bipolar devices is degraded by gamma radiation due to increased number of surface states [15]. These surface states increase the generation-recombination currents in the base and have a more pronounced effect on the beta degradation of the device at lower collector current levels. Beta can also decrease because of the introduction of trapping sites, thus lowering the minority carrier lifetime in the base region, with a resulting increase in the recombination of carriers moving through the base. This effect is particularly important in region 1 of Figure 4.2.

4.2.1.3 Measurement Results

Only a few selected bipolar devices were evaluated for radiation effects. These devices were chosen based on earlier irradiations of Wu [1]. In Figures 4.3 through 4.7 beta is plotted as a function of the collector current for V_{CE} = 2.5V.

a)



b)

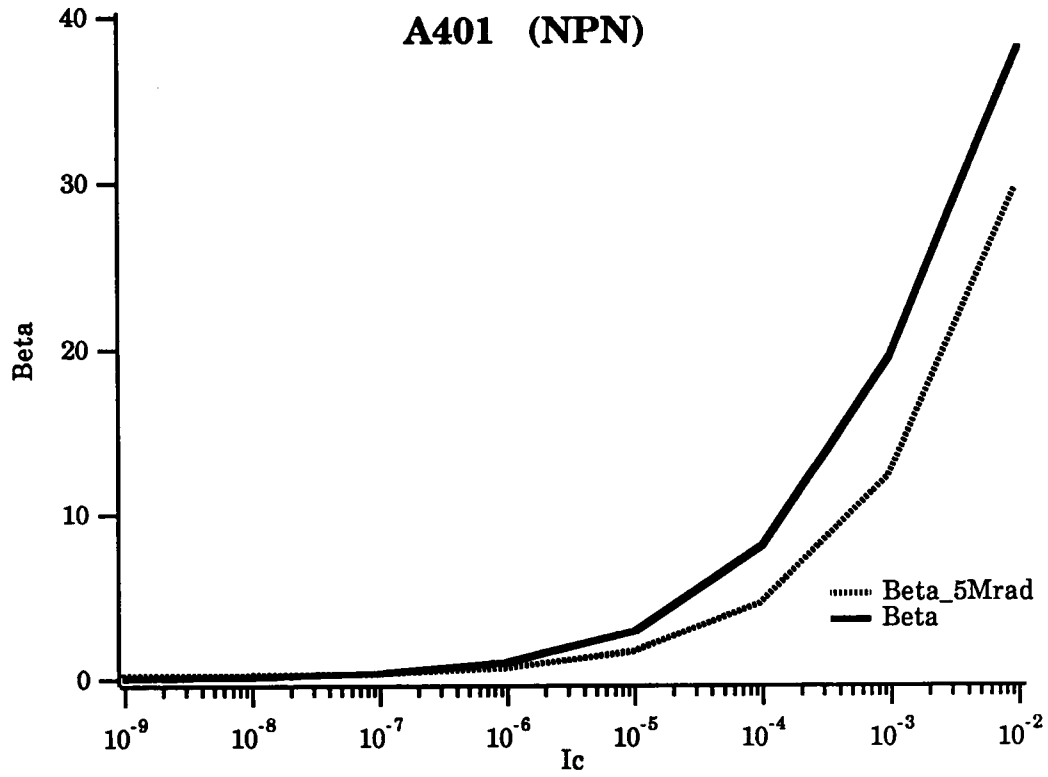
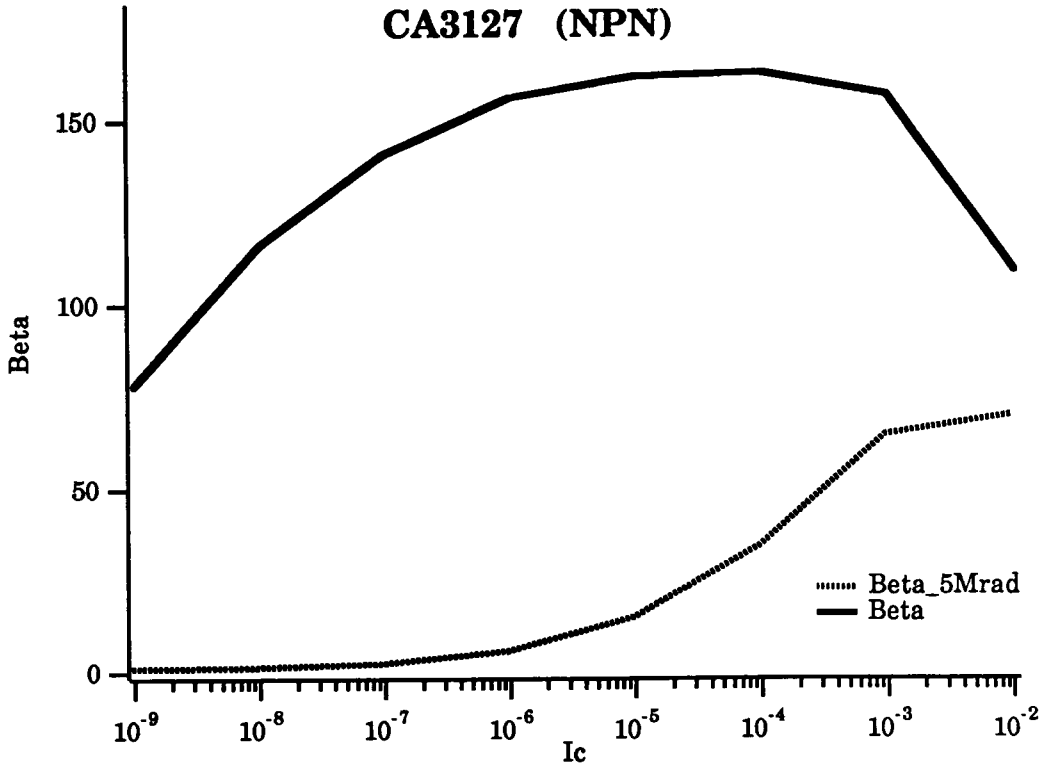


Figure 4.3. Beta vs Ic for a) MPSH10 and b) A401.

a)



b)

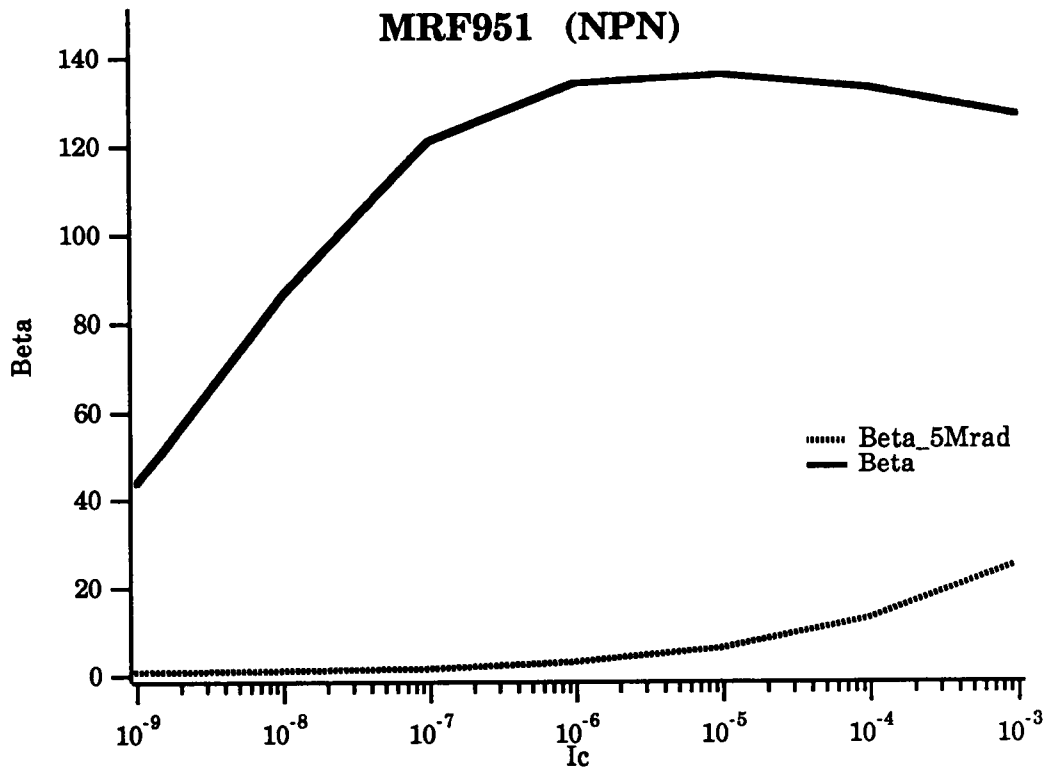
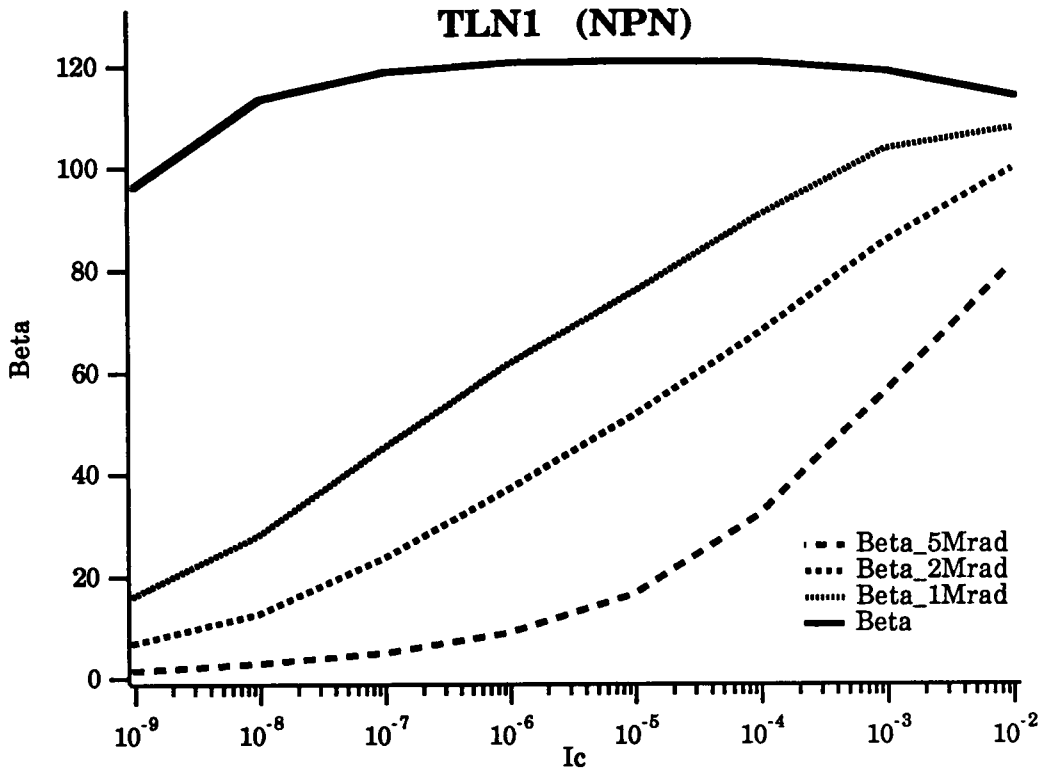


Figure 4.4. Beta vs Ic for a) CA3127 and b) MRF951.

a)



b)

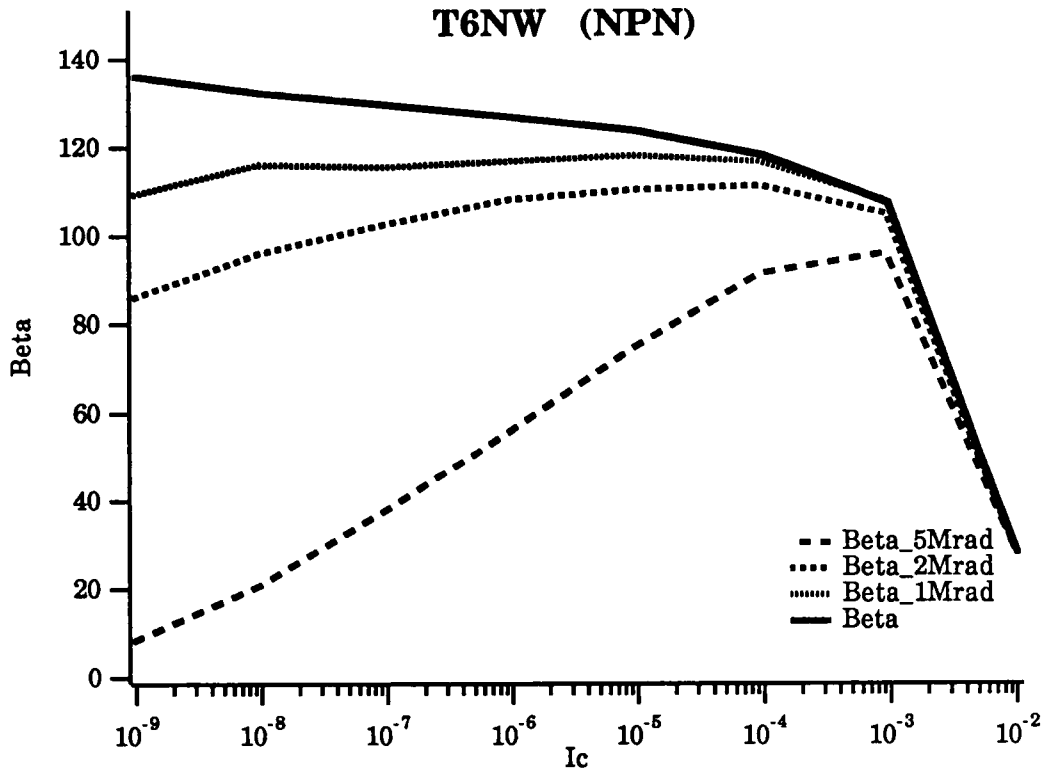
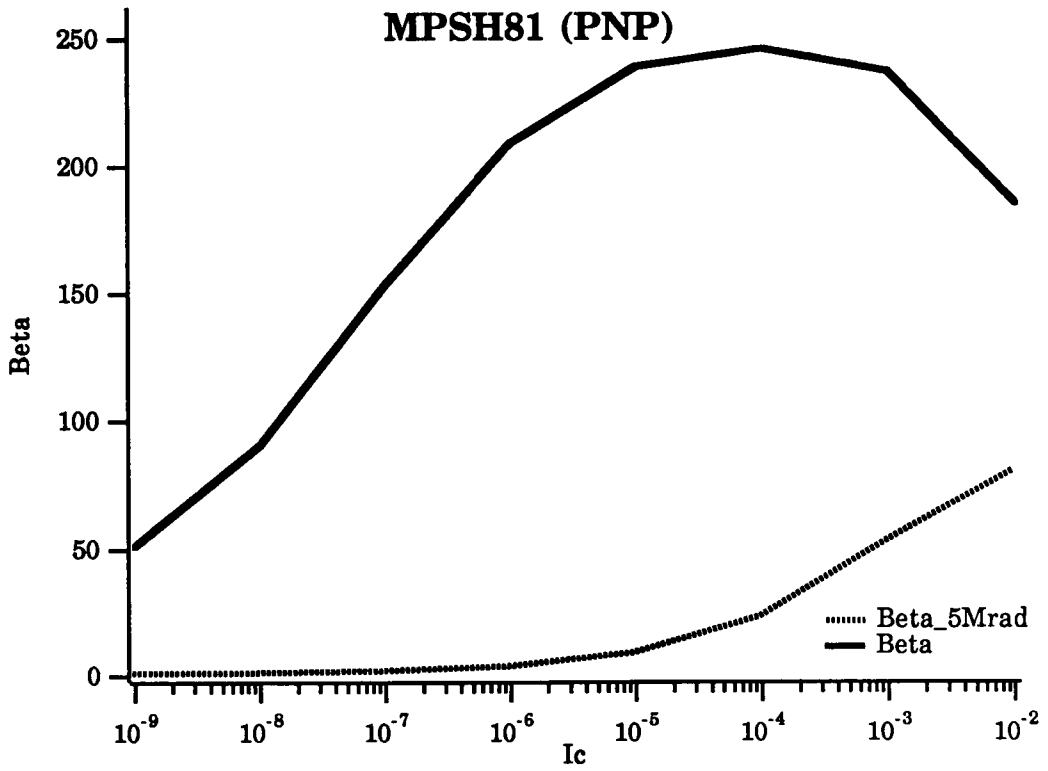


Figure 4.5. Beta vs Ic for a) TLN1 and b) T6NW.

a)



b)

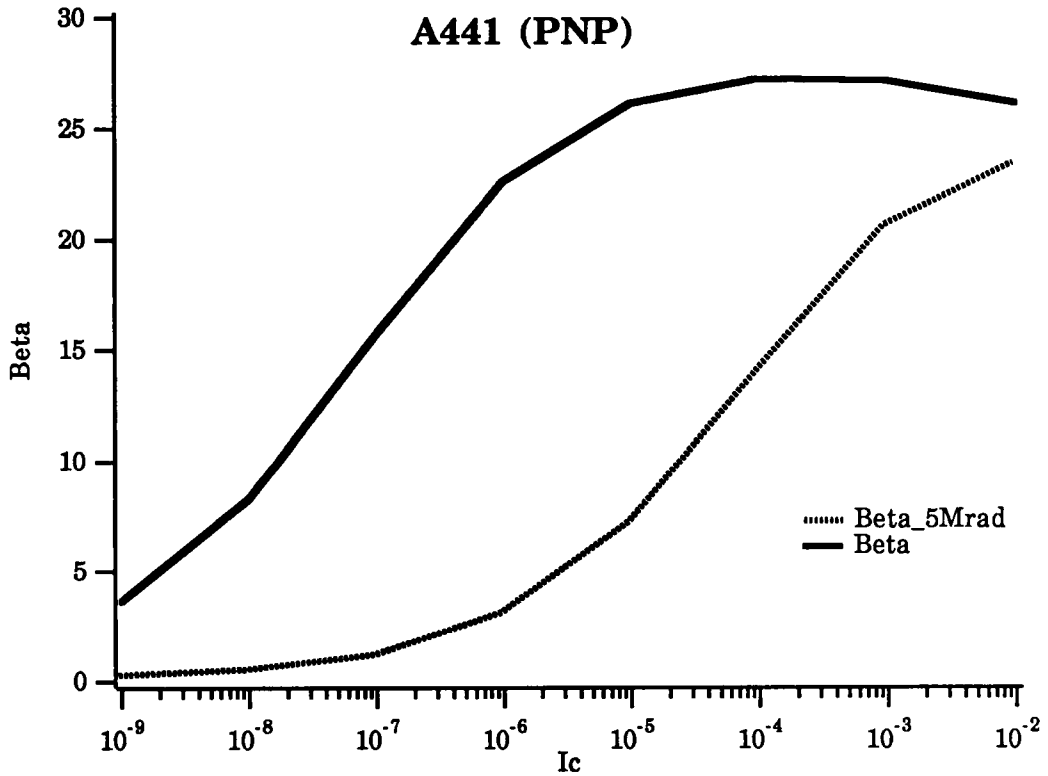


Figure 4.6. Beta vs Ic for a) MPSH81 and b) A441.

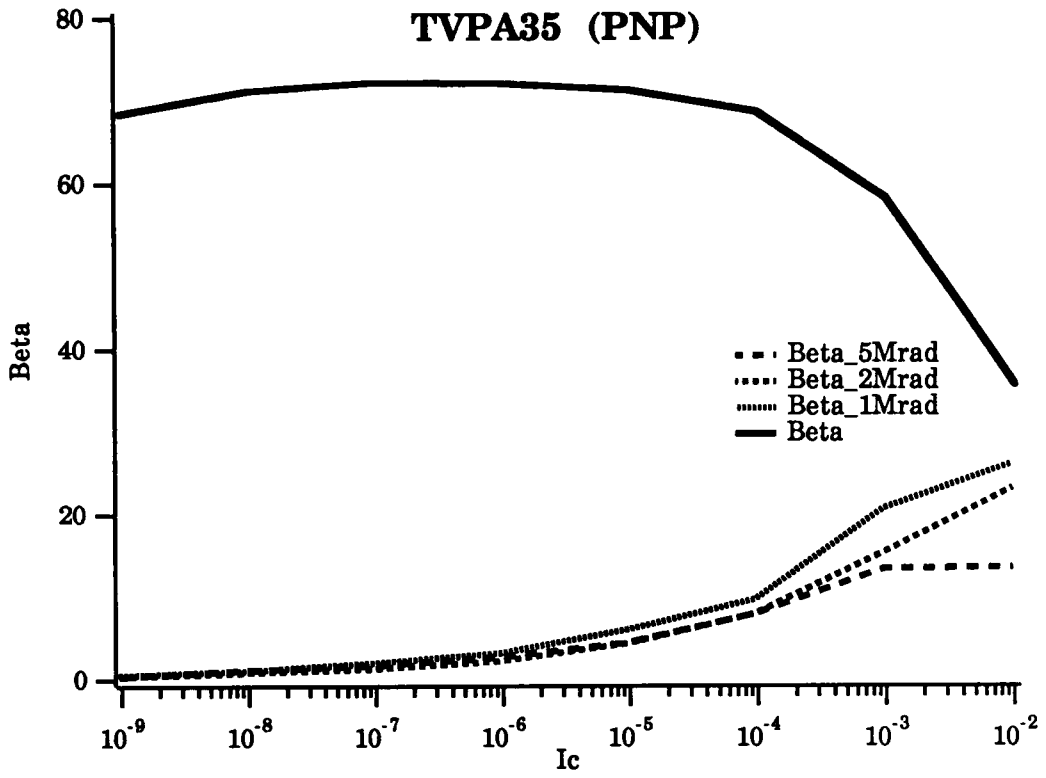


Figure 4.7. Beta vs Ic for TVPA35.

The TLN1, T6NW, and TVPA35 devices were evaluation samples from VTC Incorporated and represent typical npn and pnp devices available with the semi-custom VTC linear integrated circuit arrays. The VTC npn devices are very high frequency units with $f_T(min) = 1$ GHz for TLN1 and $f_T(min) = 6$ GHz for T6NW, while the pnp units have $f_T(min) = 1$ GHz.

4.2.2 Early Voltage

The Early voltage (V_A) of bipolars is a similar parameter to 1/lambda of JFETs. The Early voltage can be defined as [29]

$$V_A = \frac{I_C}{\left(\frac{\partial I_C}{\partial V_{CE}}\right)} \tag{4.28}$$

and is illustrated in Figure 4.8. An expression for the Early voltage in terms of base width [29] is

$$V_A = - W_B \frac{dV_{CE}}{dW_B} . \tag{4.29}$$

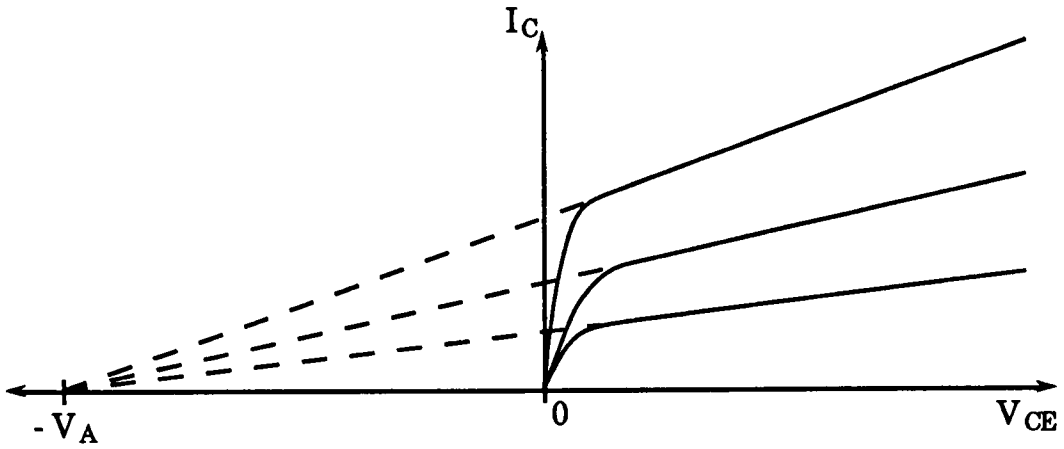


Figure 4.8. Early voltage graph.

4.2.2.1 Measurement Theory

The Early voltage was measured by finding the value of the x-axis intercept for the device in the forward active region as illustrated in Figure 4.8. The semiconductor parameter analyzer was used to obtain this data. Evaluations of V_A were typically made for I_C equal 1mA to 5mA and V_{DS} equal 2.5 Volts.

4.2.2.2 Radiation Effects

The Early voltage is complex in its relation to the physical characteristics of the device. This complexity makes it difficult to predict the reasons for change in the Early voltage due to gamma induced damage.

4.2.2.3 Measurement Results

The measurement results for the Early voltage are presented in Table 4.1.

Table 4.1. Summary of Early voltage measurements.

Part	Pre-radiation	Post-radiation	% Difference between Avg.
NPN			
MPSH10	104	101	-2.89
A401	49.0	50.0	2.04
CA3127	60.1	55.9	-6.99
MRF951	51.8	29.3	-43.4
TLN1	26.4	17.3	-34.5
T6NW	31.2	29.3	-6.1
PNP			
MPSH81	21.6	20.4	-5.56
A441	20.6	20.2	-1.94
TVPA35	10.7	7.70	-28

4.2.3 Gummel Plots

Gummel plots are graphs of the logarithm of both the base and the collector current versus the forward biased base to emitter voltage for a fixed V_{CE} voltage (typically $V_{CE} < 1V$). These plots are very useful in that they reveal several characteristics and modeling parameters in one graph.

To extract model parameters it is best to set the base to collector voltage to zero. Example Gummel curves for this case are shown in Figure 4.9.

4.2.3.1 Measurement Theory

The Gummel curves were obtained using the semiconductor parameter analyzer.

4.2.3.2 Radiation Effects

As a result of gamma radiation damage the collector current at V_{BE} = 0 (I_L) as defined in Figure 4.9 increases significantly. Also the base current experiences a large increase at lower values of V_{BE} due to the surface states formed as mentioned in section 4.2.1.2.

4.2.3.3 Measurement Results

For the Gummel curves shown (Figures 4.10 - 4.18) all post-radiation data is for 5Mrad, gamma.

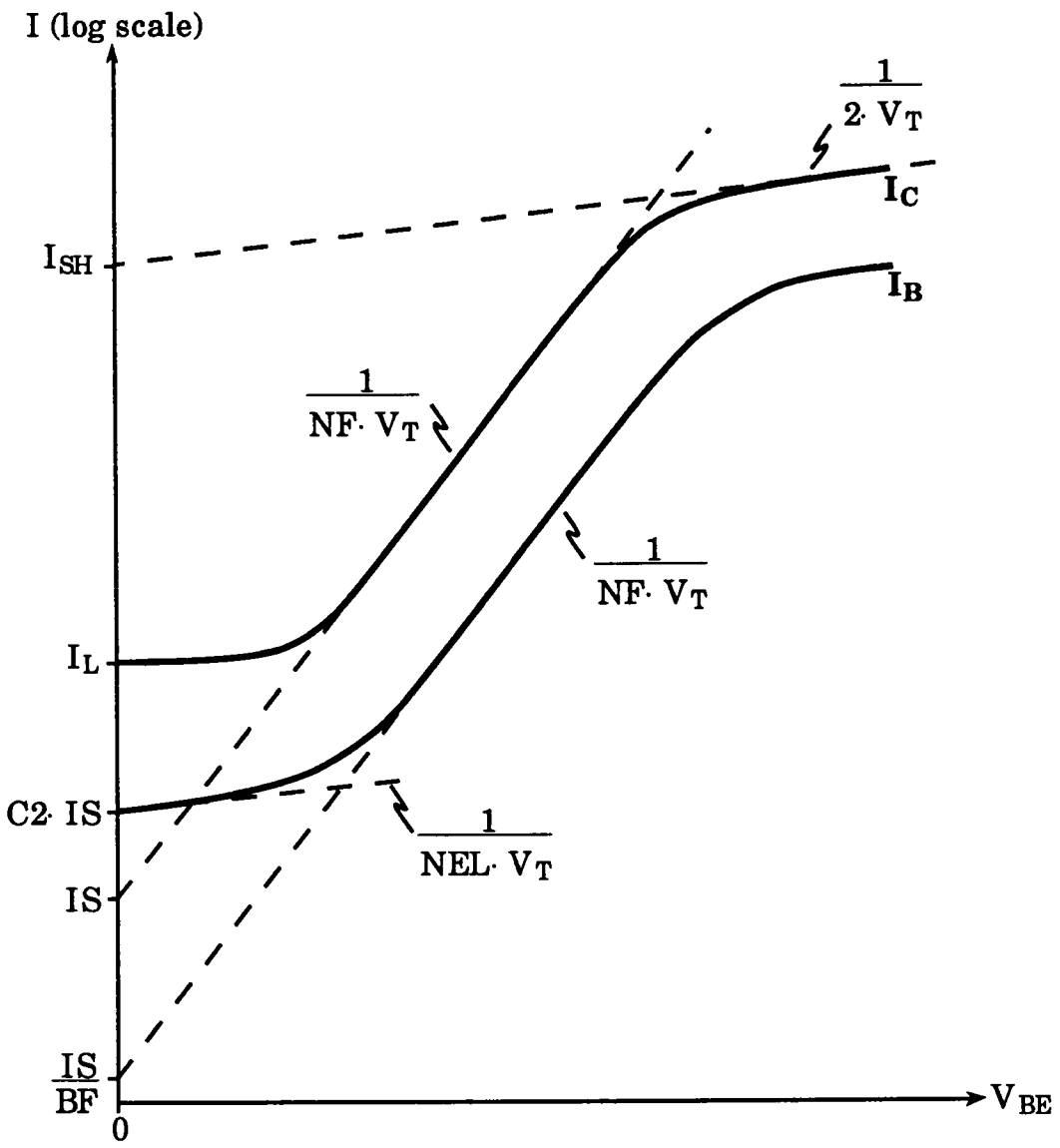


Figure 4.9. Gummel curves.

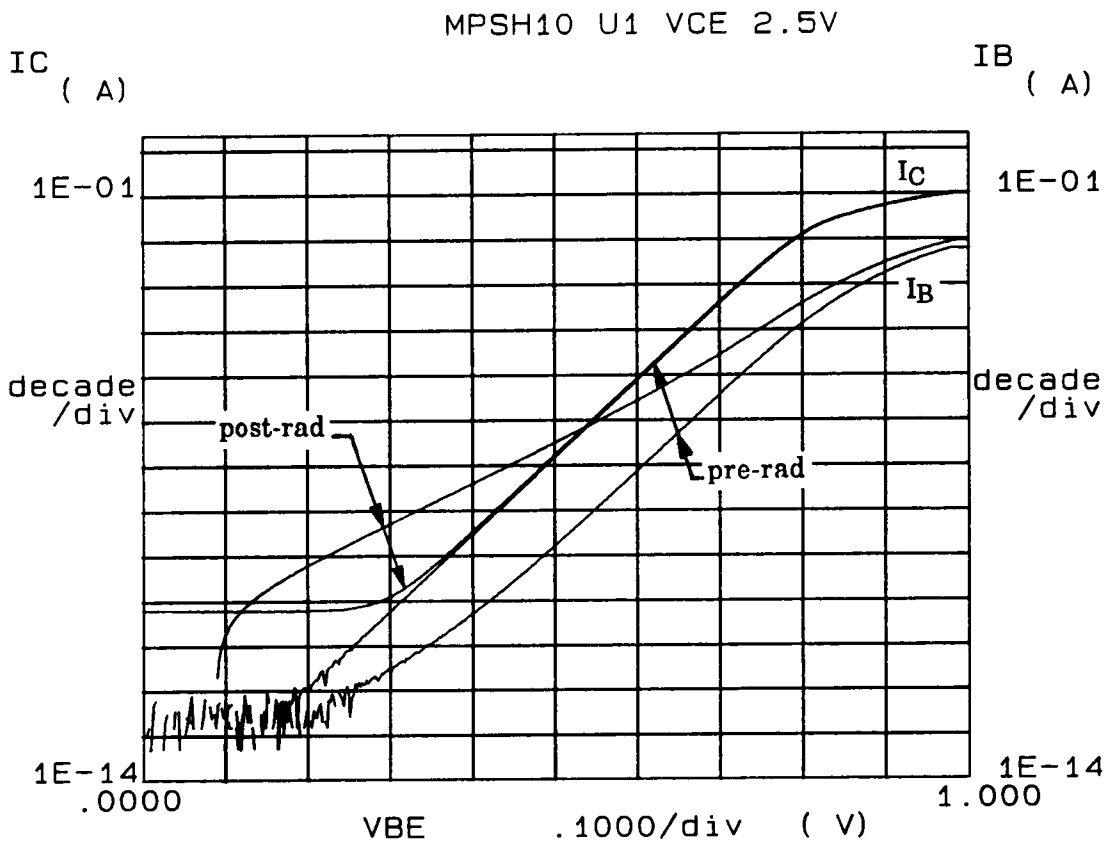


Figure 4.10. Gummel curves for MPSH10, V_{CE} = 2.5V.

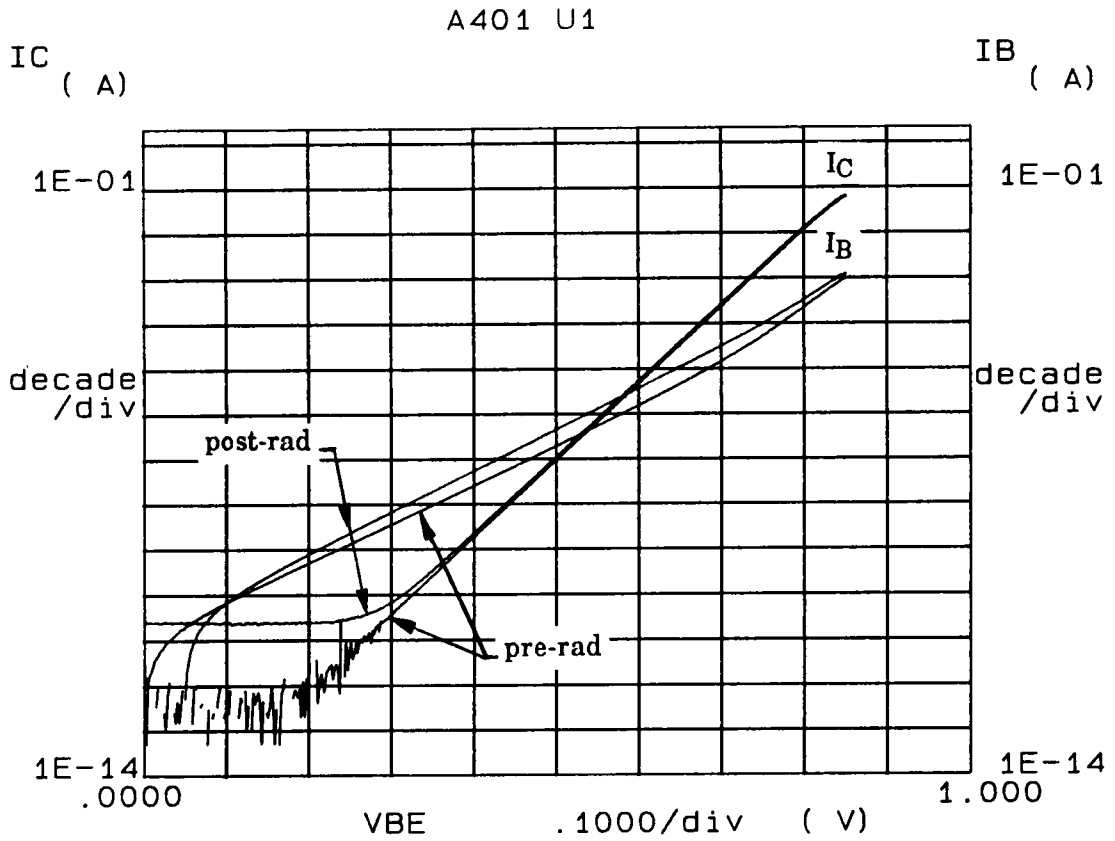


Figure 4.11. Gummel curves for A401, V_{CE} = 2.5V.

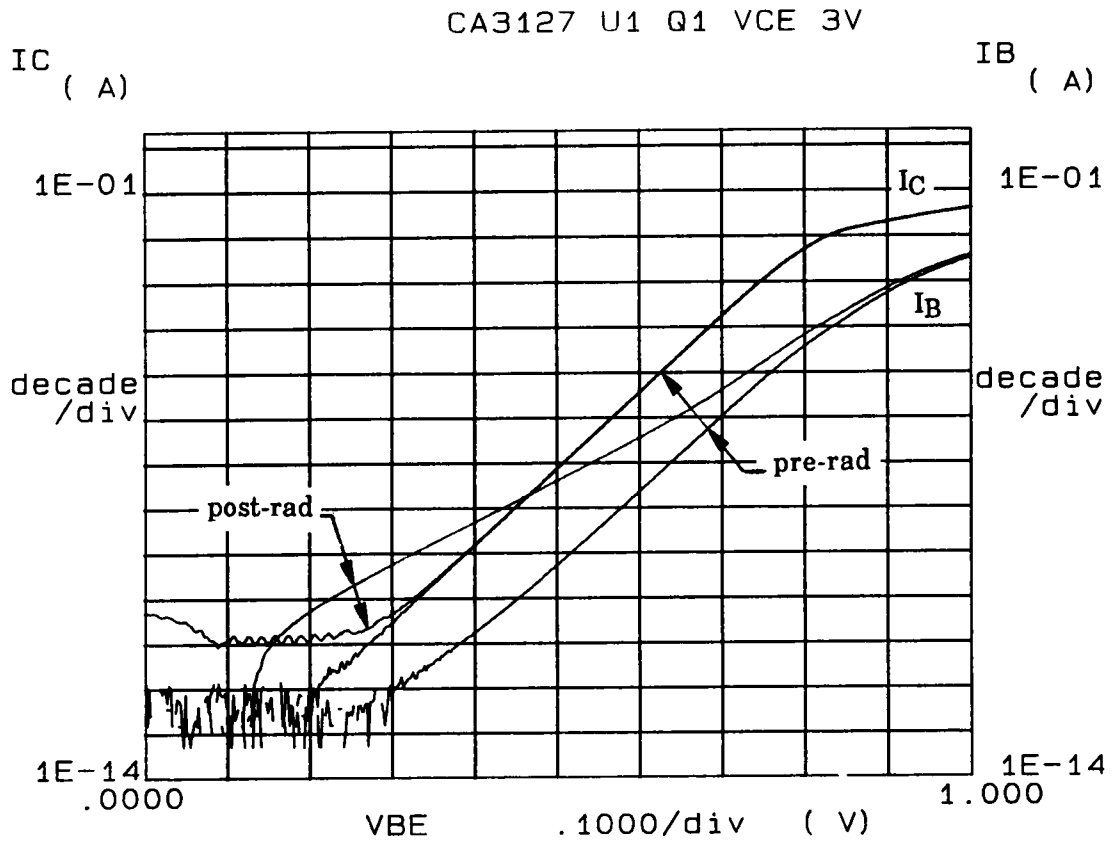


Figure 4.12. Gummel curves for CA3127, V_{CE} = 3V.

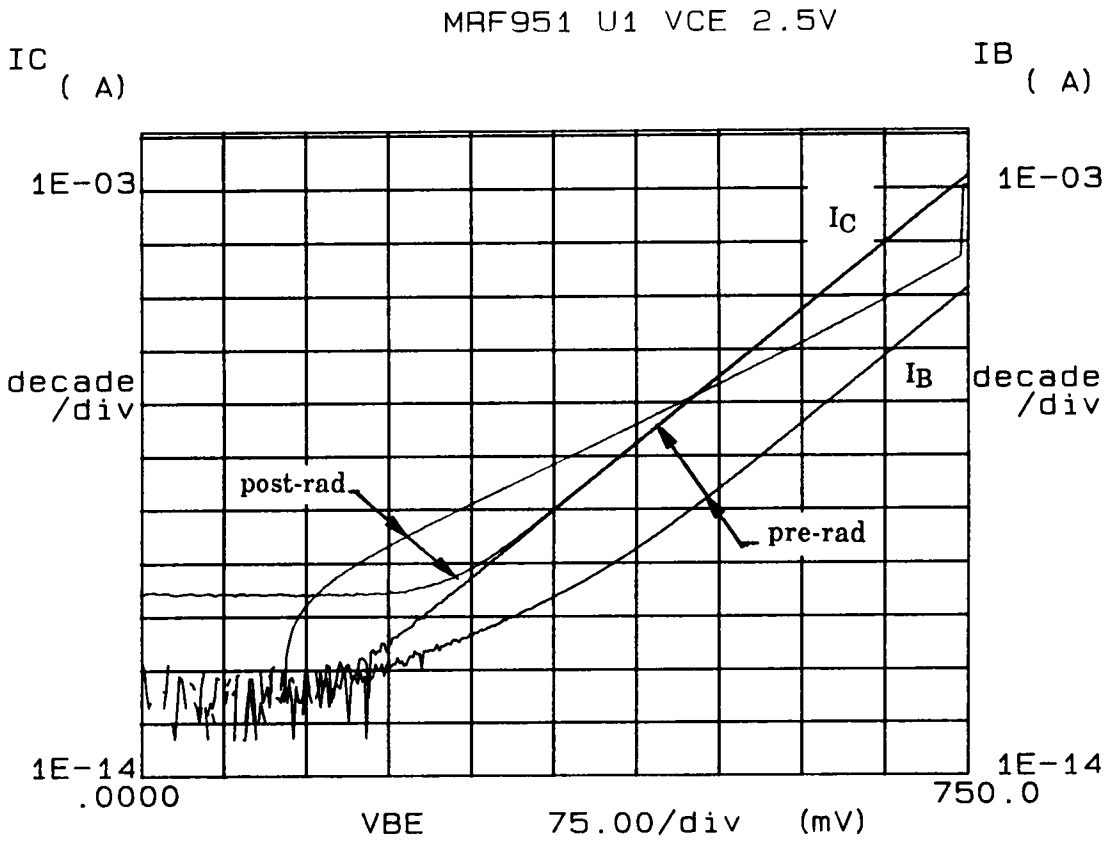


Figure 4.13. Gummel curves for MRF951, V_{CE} = 2.5V.

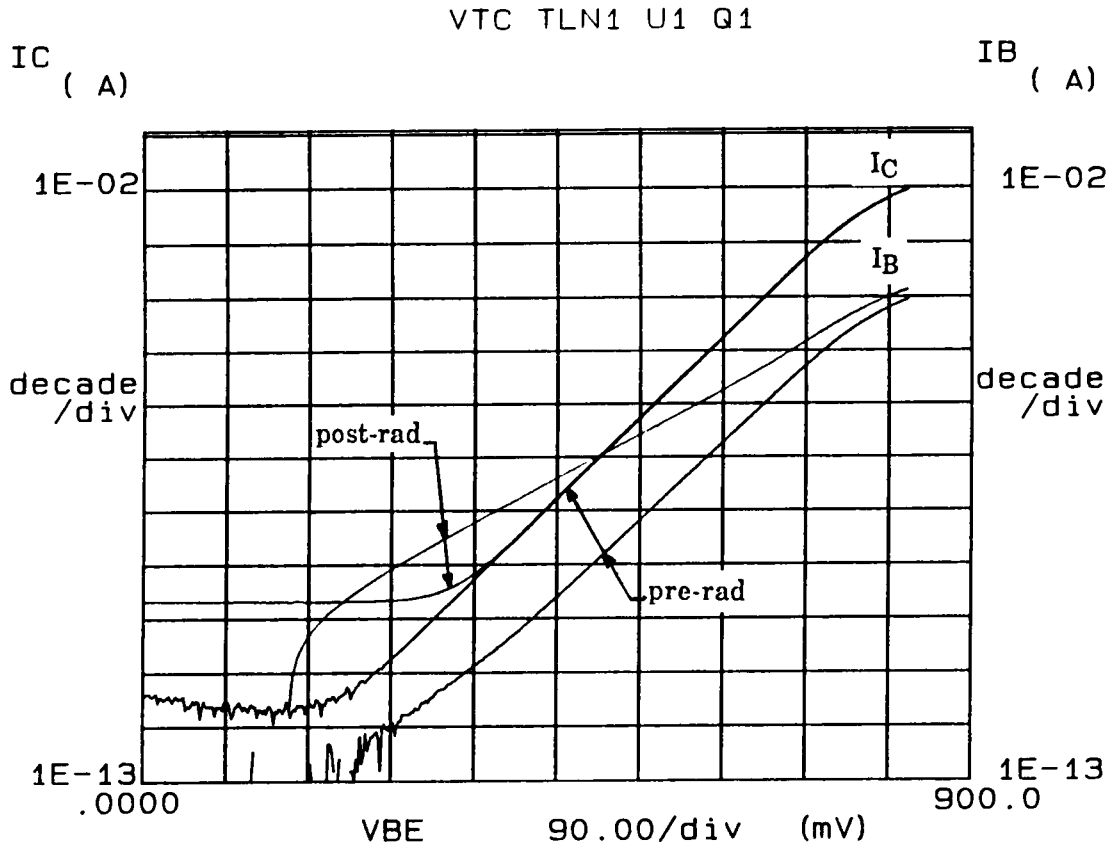


Figure 4.14. Gummel curves for TLN1, V_{CE} = 2.5V.

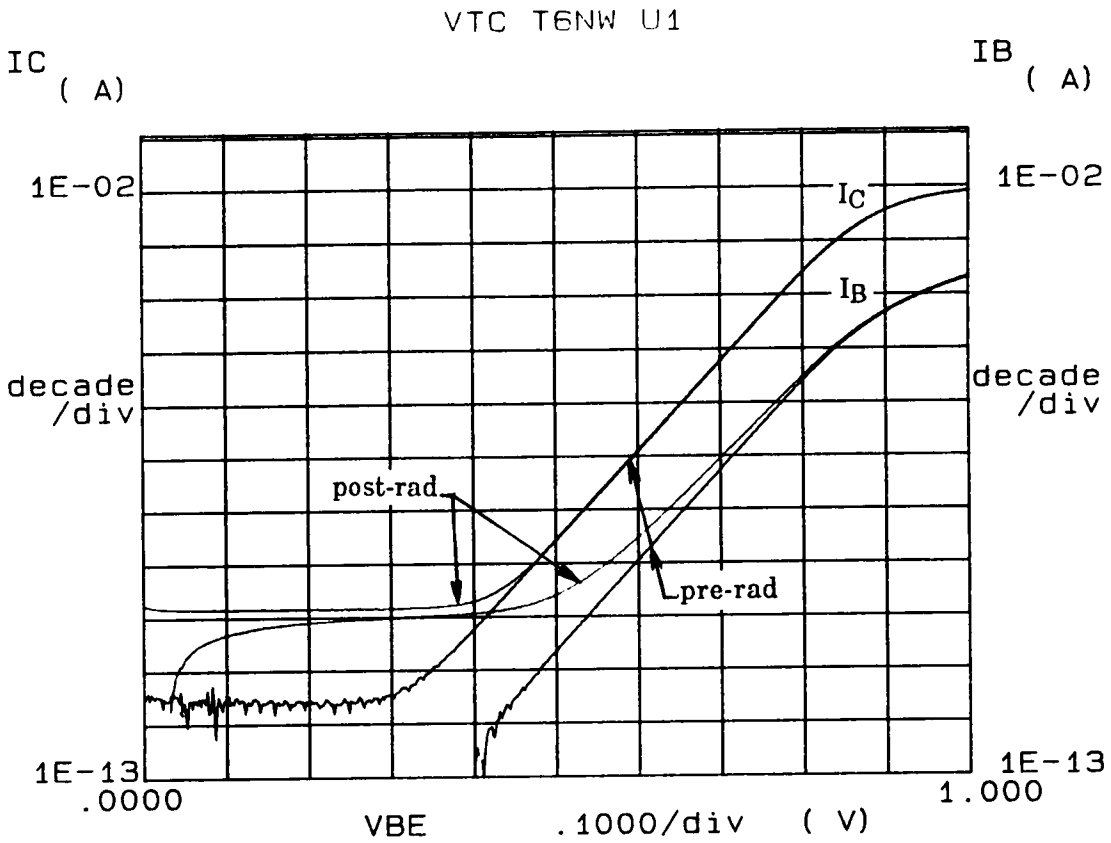


Figure 4.15. Gummel curves for T6NW, V_{CE} = 2.5V.

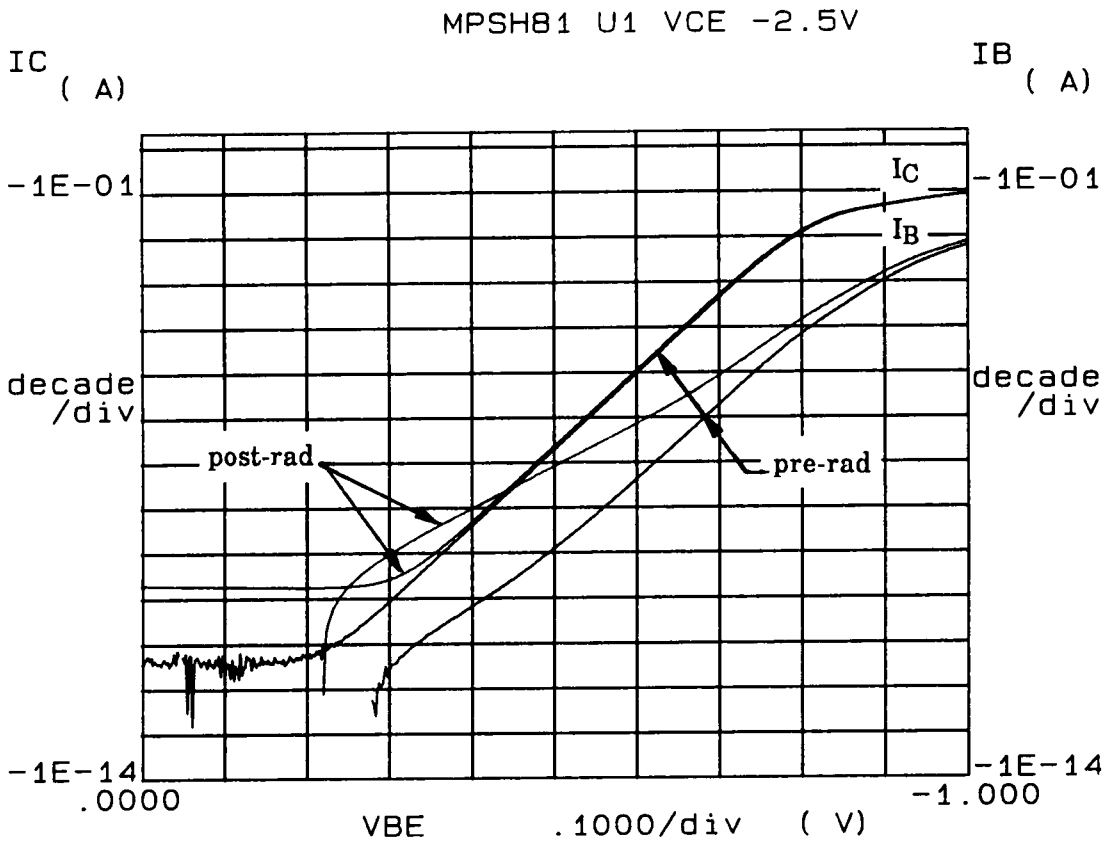


Figure 4.16. Gummel curves for MPSH81, V_{CE} = 2.5V.

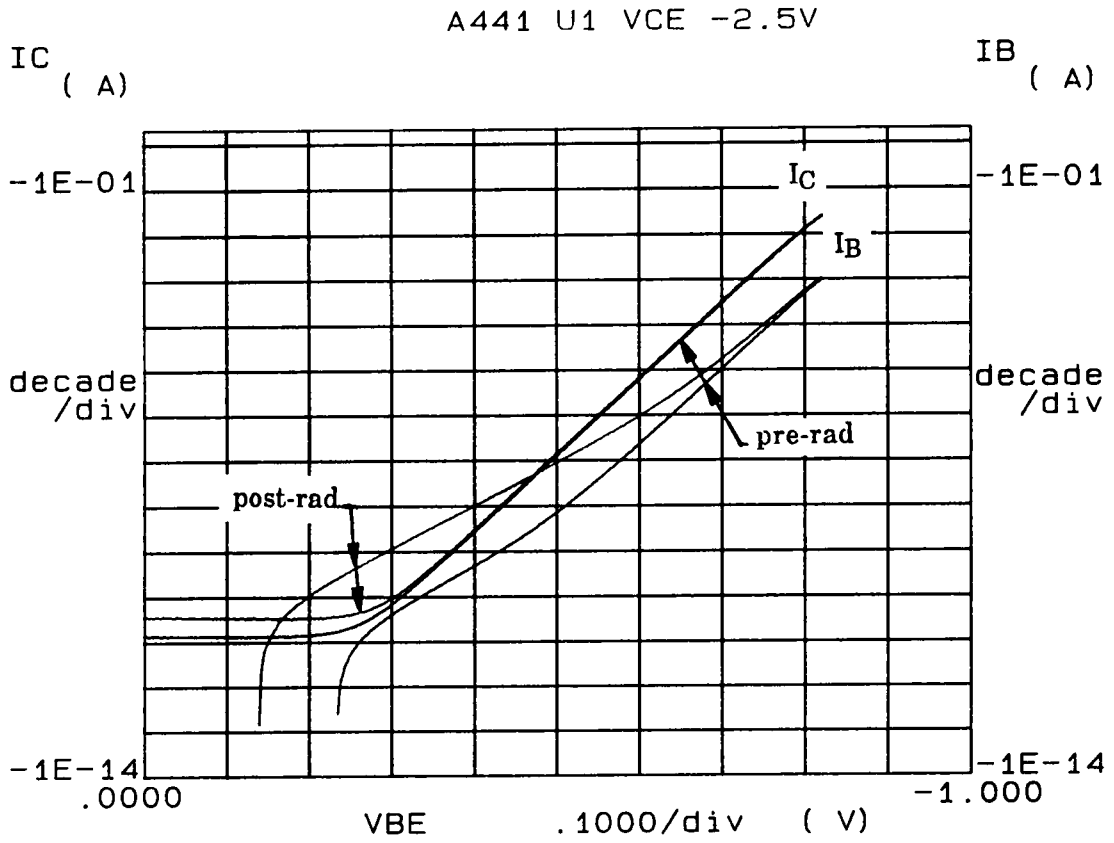


Figure 4.17. Gummel curves for A441, V_{CE} = 2.5V.

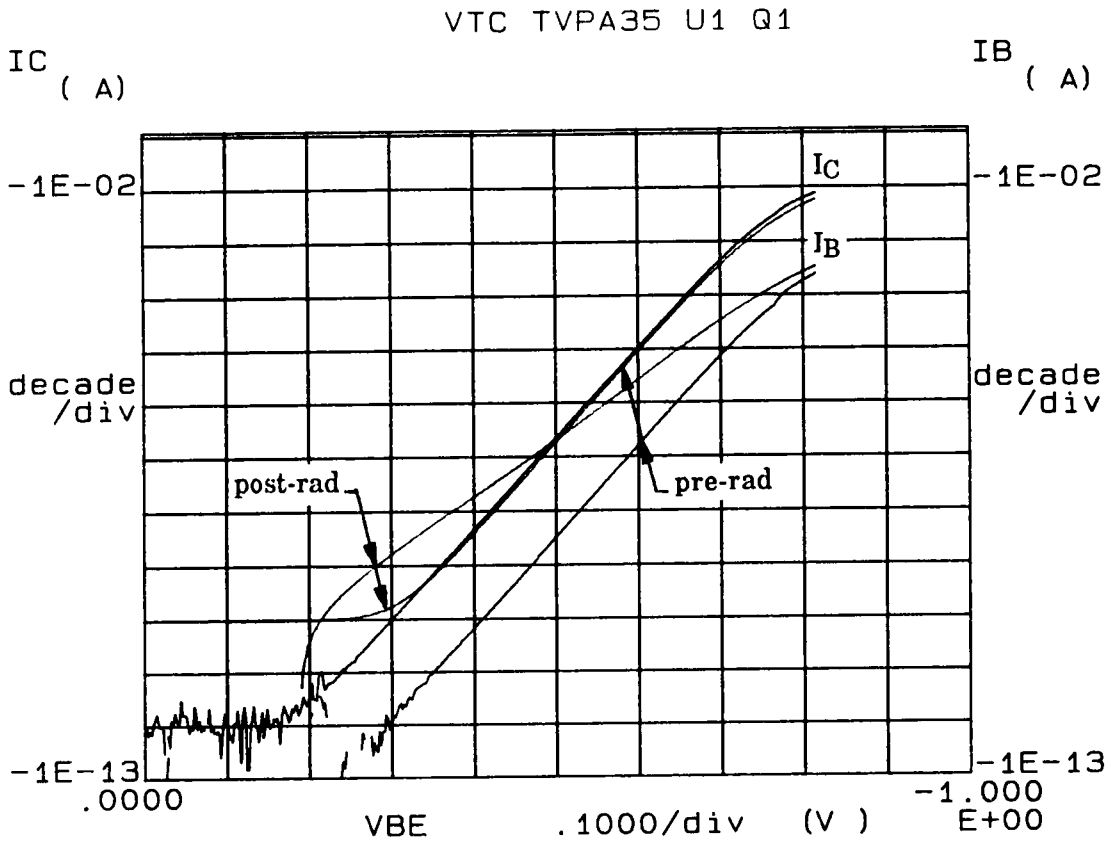


Figure 4.18. Gummel curves for TVPA35, V_{CE} = 2.5V.

4.3 Capacitance

The VTC process was characterized for capacitance before and after radiation. In all the measurements made the junctions were reversed biased thus the theoretical behavior is the same as that presented in section 3.3 on JFET capacitance measurements.

4.3.1 Measurement Theory

COB and CCS were characterized for all three types of transistors of the VTC process. CEB was also measured for the TLN1 and TVPA35 devices.

COB is the capacitance of the reverse biased base to collector junction. For npn devices this was measured as shown in Figure 4.19.

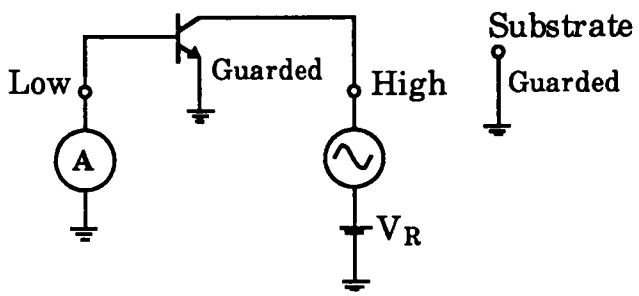


Figure 4.19. Connections for COB measurement ($V_R \geq 0$).

CCS is a measure of the reverse biased substrate to collector junction capacitance. For npn devices this was measured as shown in Figure 4.20.

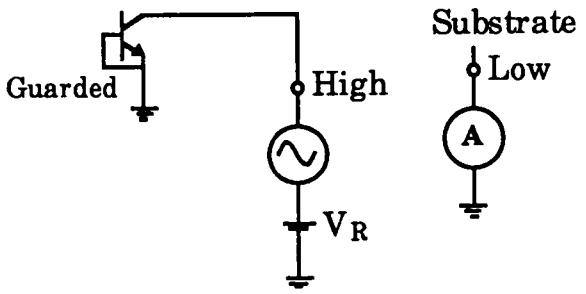


Figure 4.20. Connections for CCS measurement ($V_R \geq 0$).

CEB is a measure of the reverse biased base to emitter junction capacitance. For npn devices this was measured as shown in Figure 4.21.

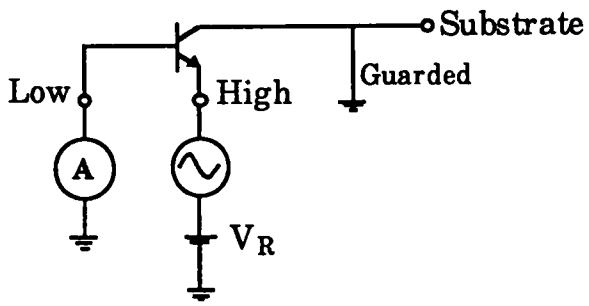


Figure 4.21. Connections for CEB measurement ($V_R \geq 0$).

4.3.2 Radiation Effects

The effects would be the same as those presented in section 3.3.1 for the radiation effects on JFETs.

4.3.3 Measurement Results

As in the JFET capacitance measurements, error bars on the following graphs (Figures 4.22 - 4.26) indicate the range of measurements (minimum to maximum) at each value of reverse voltage V_R.

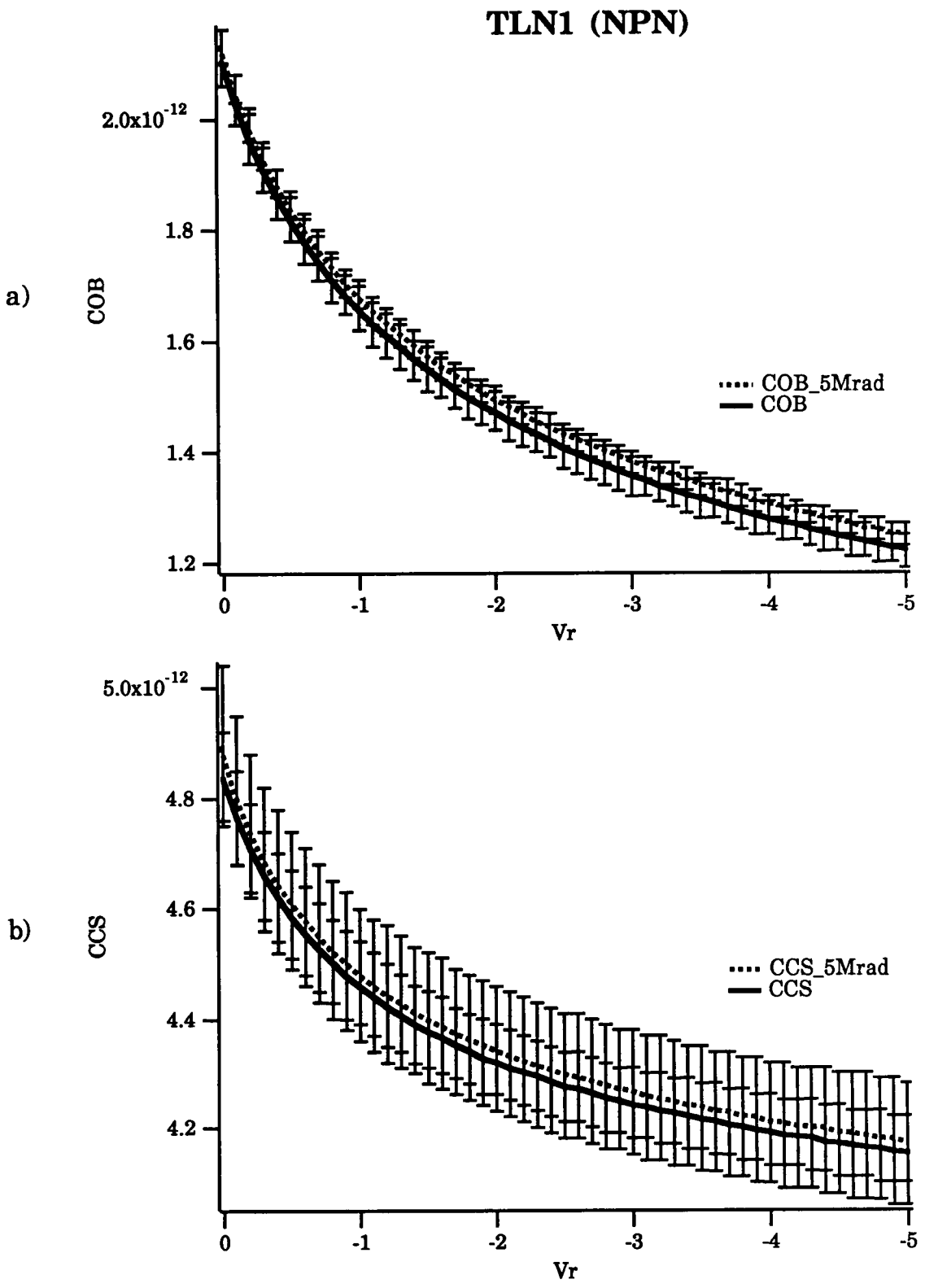


Figure 4.22. a) COB vs Vr and b) CCS vs Vr.

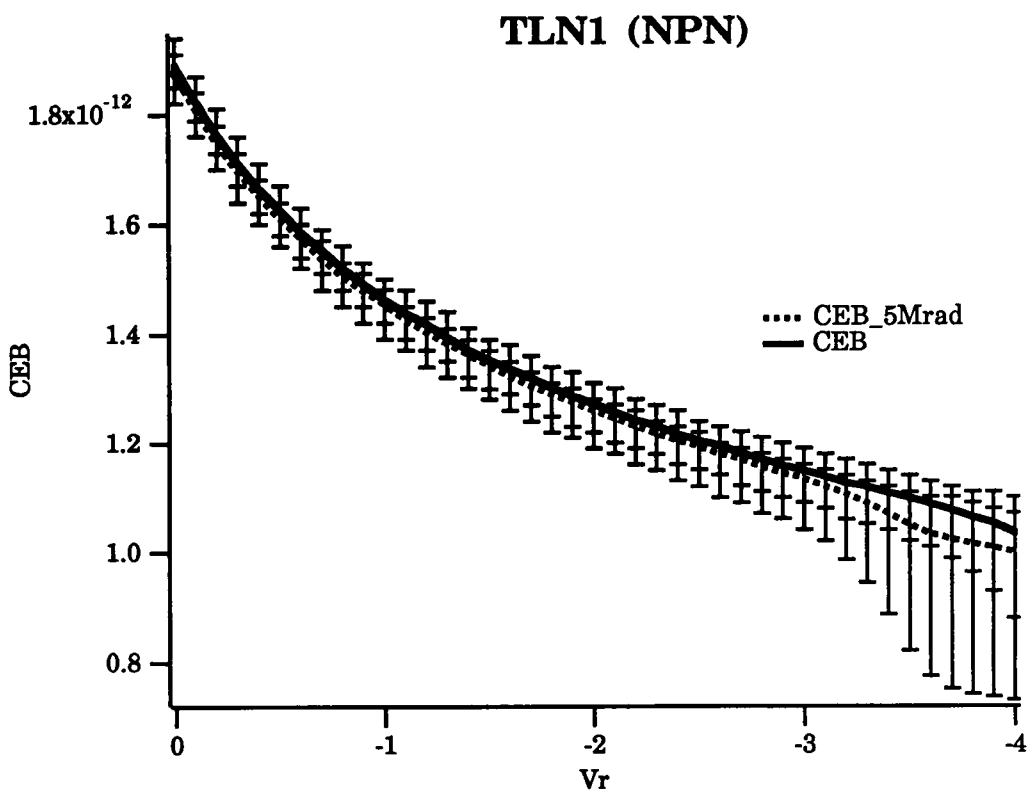


Figure 4.23. CEB vs Vr.

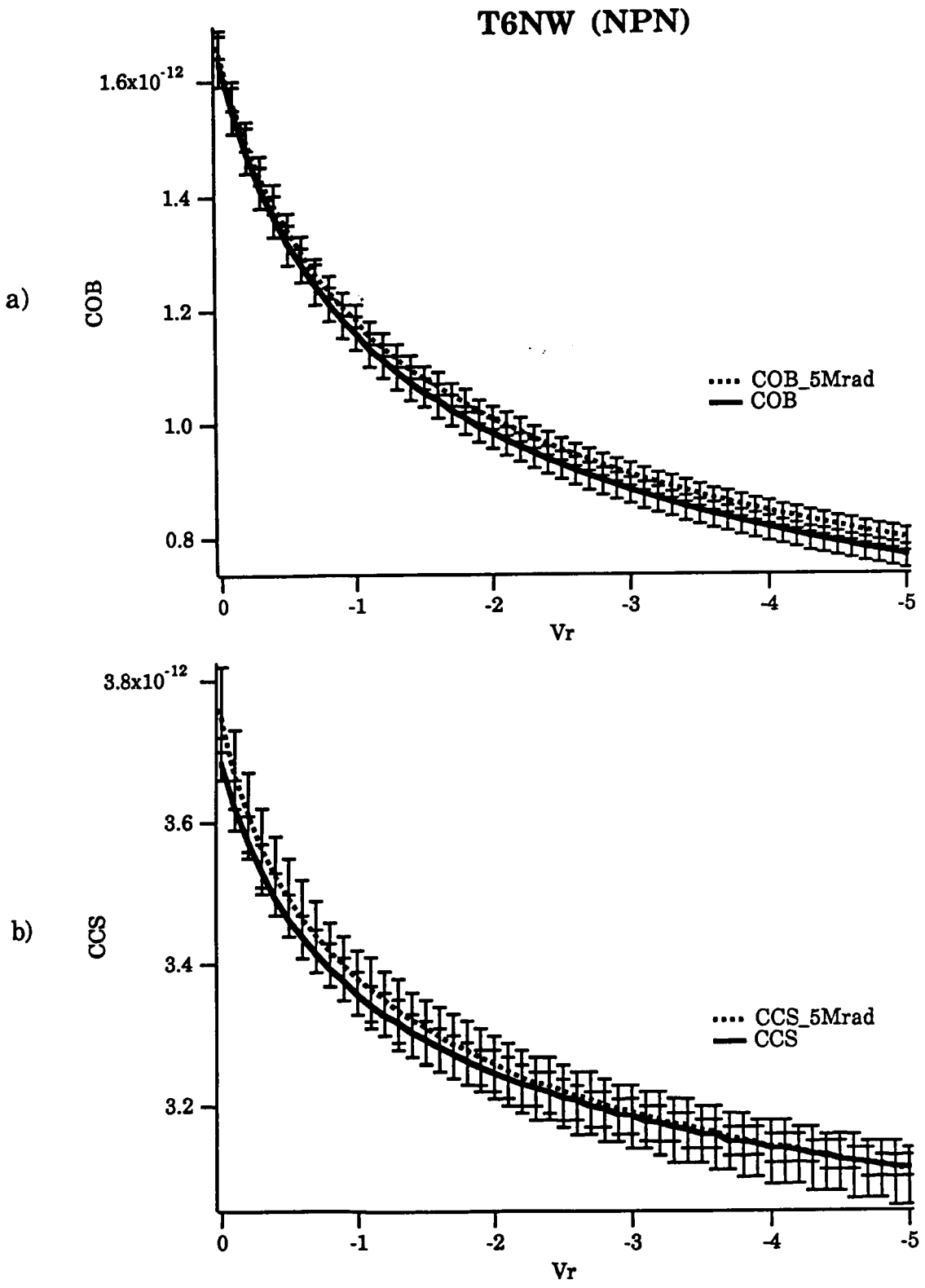


Figure 4.24. a) COB vs Vr and b) CCS vs Vr.

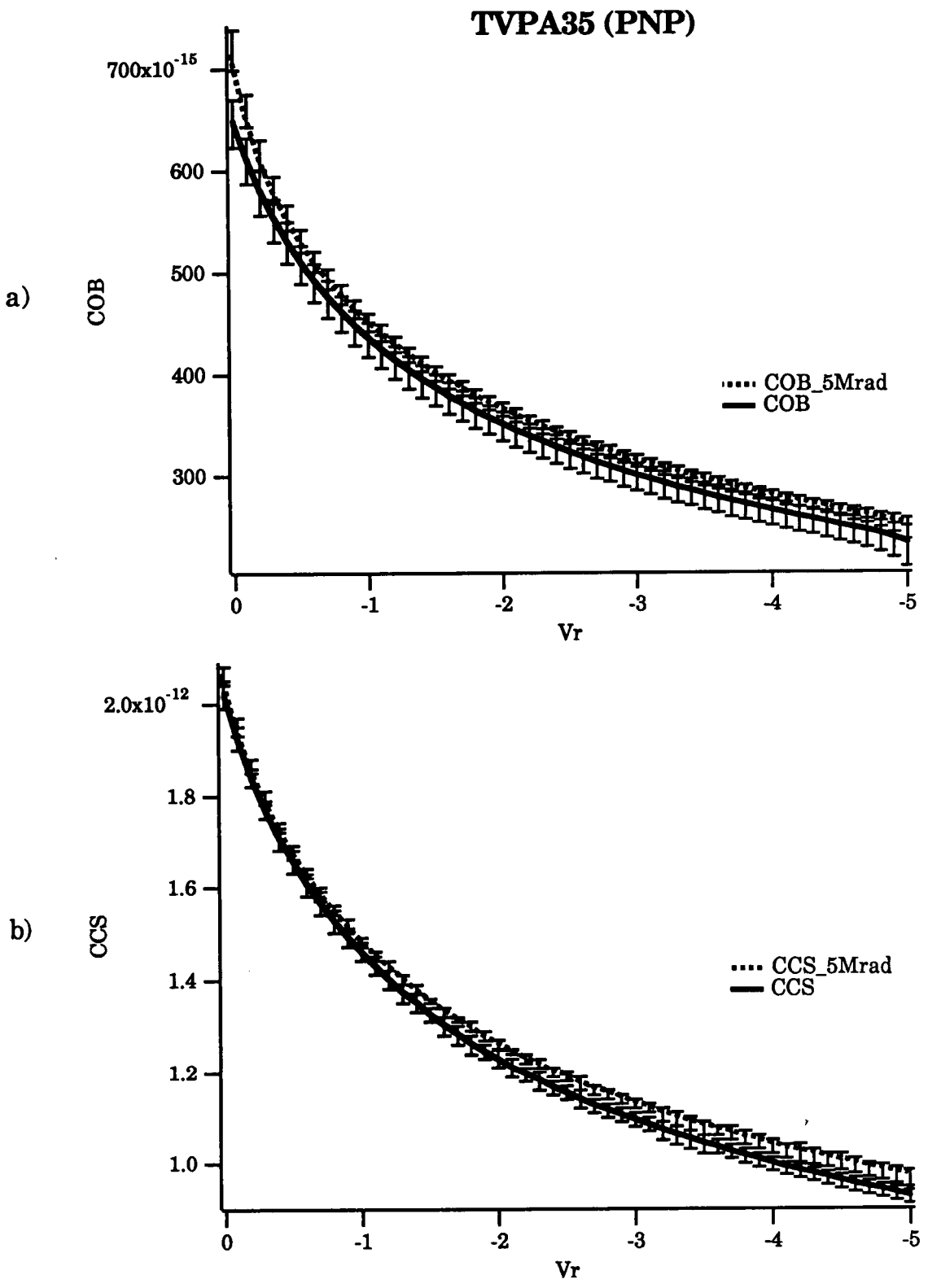


Figure 4.25. a) COB vs Vr and b) CCS vs Vr.

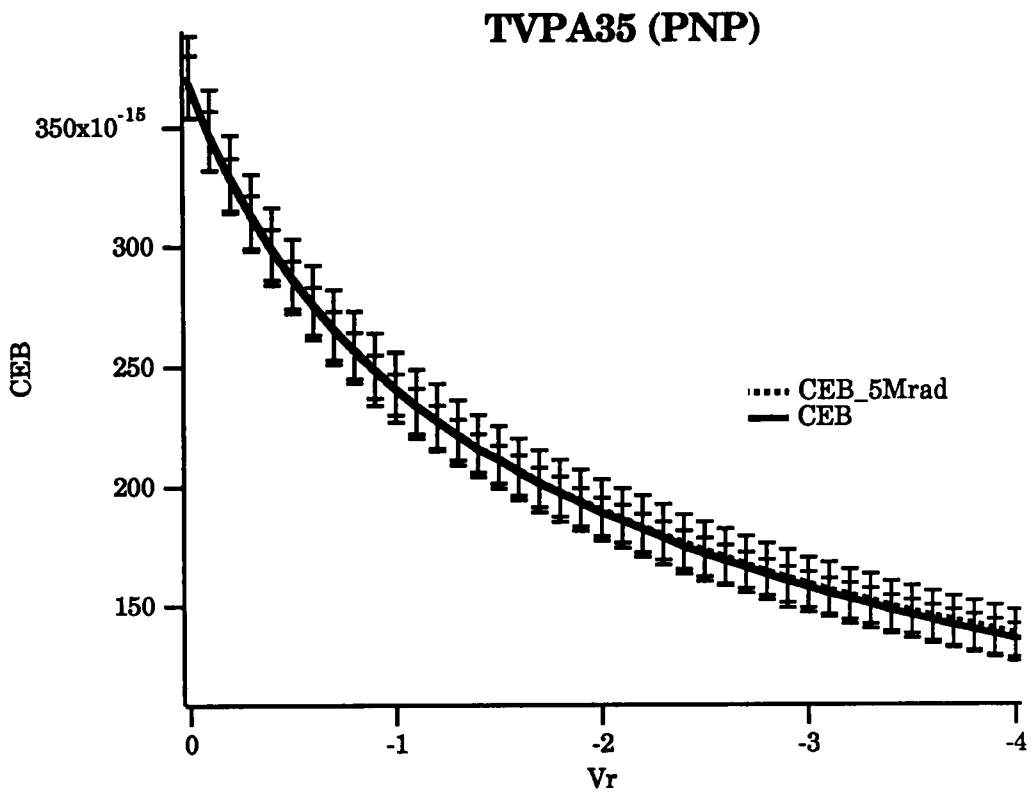


Figure 4.26. CEB vs Vr.

CHAPTER 5

CONCLUSIONS AND SUGGESTIONS FOR FURTHER STUDY

5.1 JFET Devices

As expected, the JFET's dc and ac parameters showed a good level of radiation hardness for 5Mrad, gamma. A useful parameter that was not presented earlier in the thesis is the transition frequency (f_T) for a JFET [29].

$$f_T = \frac{1}{2 \cdot \pi \left(\frac{1}{g_m}\right)(C_{GS} + C_{GD})} \tag{5.1}$$

The quantity f_T is defined as the frequency where the current gain is unity, and is a good basis for comparing devices. The different devices could be compared by finding the number of parallel devices that at the same total drain current give a chosen value of f_T. The device's parameters could then be scaled according to the number calculated. To find the number of parallel devices, based on f_T, one must consider several parameters that are very dependant on the devices operating conditions. Thus, an accurate equating of devices could only be achieved by iterating on the measurement data.

For the JFET devices, the parameters that were most affected by radiation damage were the low frequency noise characteristics and the gate leakage current. A summary of these key parameters along with f_T is shown in Table 5.1.

5.2 Bipolar Devices

The parameter that was commonly characterized for all bipolar devices was beta. From the results it can be seen that this parameter is sensitive to radiation damage and is a critical parameter for the circuit designer. The VTC process npn transistors along with RCA's CA3127 showed the most radiation hardness of the devices tested. For the pnp devices the A411 showed radiation hardness if operated in a higher current region. VTC's pnp performed poorly after exposure to radiation.

5.3 Suggestions for Further Study

The effects of radiation induced damage on silicon devices is a very interesting and yet not completely defined discipline. There are many opportunities for the exploration of these effects. A few topics that appear to need more attention are the following:

- The noise of the JFET devices showed a trend of increasing radiation hardness the more they were operated in the subthreshold region. It would be interesting to explore this characteristic further.

Table 5.1. Summary of critical JFET parameters. Id = 100uA and Vgs = 2.5V

Part	Rn	Pre-rad. f_n	Post-rad. f_n	Pre-rad. I_G	Post-rad. I_G	Pre-rad. f_T	Post-rad. f_T
NJ3600L	197	23	21K	285p	6.25n	1.31M	1.28M
NJ903L	310	220	89K	85.4p	25.6n	2.69M	2.80M
NJ1800DL	331	70	40K	.880p	3.70n	2.03M	1.96M
2N6451	336	25	73K	.120p	185p	23.3M	22.5M
2SK152A	380	3.6K	130K	.588p	.839n	52.9M	52.4M
2N4858	394	58	95K	.952p	716p	23.6M	23.4M
2N4416A	1.18K	710	300K	< .1p	377p	77.2M	60.7M
IMF5912	1.30K	49K	460K	.525p	75.7p	39.2M	34.2M
2N5432				61.8p	14.1n	2.93M	2.91M

- The noise characteristics of the bipolar devices measured at the same bias conditions as the JFET would be useful for comparison.

- A study of all devices both bipolar and JFET with the transition frequency (f_T) as the basis so that measurement results could be normalized. This would prove very interesting in not only the comparison of radiation hardness of similar device types, but also of different transistor types.

- A automated and more general noise measurement system.

BIBLIOGRAPHY

BIBLIOGRAPHY

[1] A. Wu, Title, "Gamma Irradiation Testing of Electronic Devices, and Evaluation of Irradiated CMOS Components on MOSIS Test Chips," *M. E. Thesis*, The University of Tennessee, Knoxville, Tennessee, 1990.

[2] E. J. Kennedy, C. L. Britton, and B. Bugg, to be presented.

[3] W. Buttler, B. J. Hosticka, G. Lutz, and P. F. Manfredi, "A JEFET-CMOS Radiation-Tolerant Charge-Sensitive Preamplifier," *IEEE Journal of Solid-State Circuits*, vol 25, pp. 1022-1024, 1990.

[4] E. Gatti, Ahrisoho, P. F. Manfredi, "Choice between FETs or Bipolar Transistors and Optimization of their Working Points in Low Noise Preamplifiers for Fast Pulse Processing. Theory and Experimental Results," *IEEE Transactions on Nuclear Science*, vol NS-30, pp. 319-323, 1983.

[5] J. H. Stephen, "Low Noise Junction Field Effect Transistors Exposed to Intense Ionizing Radiation," *IEEE Transactions on Nuclear Science*, vol NS-33, pp. 1465-1470, 1986.

[6] H. P. Orrick, E. J. Kennedy, T. V. Blalock, *The Effects of Gamma Radiation on Semiconductor Devices for High Temperature Electronics*, University of Tennessee, Knoxville, 1981.

[7] E. Vittoz and J. Fellrath, "CMOS Analog Integrated Circuits Based on Weak Inversion Operation," IEEE Journal of Solid-State Circuits, vol. SC-12, pp. 224-231, 1977.

[8] M. B. Barron, "Low Level Currents in Insulated Gate Field Effect Transistors," *Solid-State Electronics*, vol 15, pp. 293-302, 1972.

[9] R. J. Brewer, "The 'Barrier Mode' Behavior of a Junction FET at Low Drain Currents, " Solid-State Electronics, vol. 18, pp. 1013-1017, 1975.

[10] W. M. C. Sansen and C. J. M. Das, "A Simple Model of Ion-Implanted JFET's Valid in Both the Quadratic and Subthreshold Regions," *IEEE Transactions on Electron Devices*, vol 37, pp. 1773-1775, 1990

[11] W. W. Wong, J. J Liou, and J. Prentice, "An Improved Junction Field-Effect Transistor Static Model for Integrated Circuit Simulation," *IEEE Journal of Solid-State Circuits*, vol 25, pp. 1022-1024, 1990.

[12] R. C. Weast, *CRC Handbook of Chemistry and Physics*, Cleveland, Ohio: CRC Press, 1976.

[13] G. F. Knoll, *Radiation Detection and Measurement*, New York: John Wiley and Sons, 1989.

[14] E. J. Kennedy private communication.

[15] G. C. Messenger and M. S. Ash, *The Effects of Radiation on Electronic Systems*, New York: Van Nostrand Reinhold Company, 1986.

[16] J. A. Harrell, P. L. Manke, and J. E. Gover,"The Application of Remote Electronics in a Nuclear Fuel Reprocessing Environment: Radiation Effects and Design Guidelines," *Sandia Report*,SAND82-2151, January 1983.

[17] E. Klontz and K. Lark-Horovitz, "Electron Bombardment of Ge," *Physical Review*, vol 82, pp. 763, 1951.

[18] F. W. Sears, M. W. Zemansky, and H. D. Young, University Physics, Reading, Massachusetts: Addison-Wesley Publishing Company, 1983.

[19] GAMMACELL 200 INSTRUCTION MANUAL, edition 7, Atomic Energy of Canada, Ltd. Ottawa, Canada, 1970.

[20] D. K. Su, "The Effects of Gamma and Neutron Irradiations on Linear Integrated Circuits and Power Devices," *M. E. Thesis*, The University of Tennessee, Knoxville, Tennessee, 1988.

[21] SLICE Users Manual, HARRIS Semiconductor, 1989.

[22] W. Shockley, "A Unipolar 'Field-Effect' Transistor," *Proceedings of the IRE*, vol. 40, pp. 1365-1376, 1952.

[23] B. J. Sheu, D. L. Scharfetter, P. Ko, M. Jeng, "BSIM: Berkeley Short-Channel IGFET Model for MOS Transistors," IEEE Journal of Solid-State Circuits, vol. SC-22, pp. 558-566, 1987.

[24] C. D. Hartgring, "An Accurate JFET/MESFET Model for Circuit Analysis," Solid-State Electronics, vol. 25, pp. 233- 240, 1982.

[25] J. M. Rochelle private communication.

[26] E. S. Yang, *Microelectronic Devices*, New York: McGraw-Hill Book Company, 1988.

[27] A. Many, Y. Goldstein, and N. B. Grover, *Semiconductor Surfaces*, Amsterdam: North-Holland Publishing Company, 1965.

[28] R. S. Muller and T. I. Kamins, *Device Electronics for Integrated Circuits*. New York: John Wiley and Sons, 1986.

[30] A. van der Ziel, "Thermal Noise in Field-Effect Transistors," *Proceedings of the IRE*, vol. 50, pp. 1808-1812, 1962.

[31] T. V. Blalock, "Optimization of Semiconductor Preamplifiers for Use with Semiconductor Radiation Detectors," *Ph. D. Dissertation*, The University of Tennessee, Knoxville, Tennessee, 1965.

[29] P. R. Gray and R. G. Meyer,*Analysis and Design of Analog Integrated Circuits*, New York: John Wiley and Sons, 1984.

[32] M. B. Das and J. M. Moore, "Measurements and Interpretation of Low-Frequency Noise in FET's," *IEEE Transactions on Electron Devices*, vol ED-21, pp. 247-257, 1974.

[34] I. Getreu, *Modeling the Bipolar Transistor*, Beaverton, Oregon: Tectronix, Inc., 1979.

[33] C. D. Motchenbacher and F. C. Fitchen, *Low-Noise Electronic Design*, New York: John Wiley and Sons, 1973.

APPENDIXES

APPENDIX A

NOISE MEASUREMENT SYSTEM

The noise measurement system used for measuring JFET noise is shown in Figure A.1. Earlier attempts were made to automate the noise measurements using the HP4195A spectrum analyzer, but the time required for accurate measurements and a problem with repeatable results forced the use of a semi-automated system.

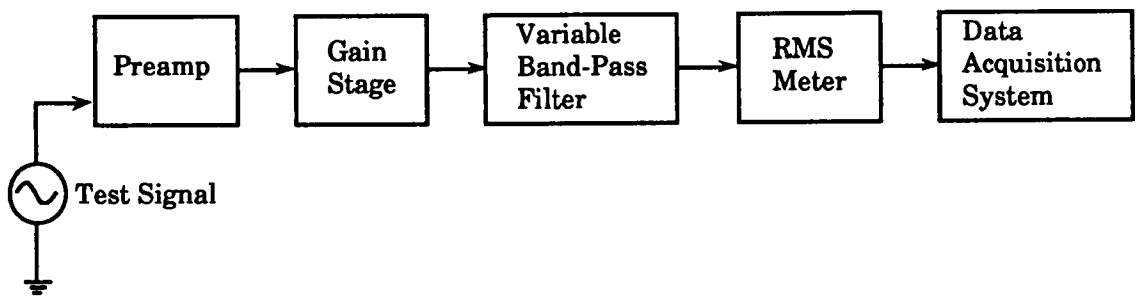


Figure A.1. Noise measurement system.

The preamplifier in Figure A.1 acquires the drain current noise of the JFET being tested and amplifies this signal so that it is dominate over the noise of the following gain stages. The gain stages of the noise measurement system simply amplify the noise signal so that the final signal measured by the RMS Voltmeter is at a measurable level. The variable band-pass filter allows a narrow section of the noise spectrum to pass through, which is then measured by the RMS Voltmeter as the output

noise. After the rms value of the noise for a particular frequency in measured, a test signal of the same frequency is then applied to the system to find the total noise gain. From this information the data acquisition system calculates the series noise resistance (R_n) of the JFET being tested and stores the result. This process is continued for all measured points in the spectrum.

A.1 Pre-amplifier

Several different configurations were explored before the preamplifier shown in Figure A.2 was chosen. Figure A.2 shows both a preamplifier and a gain stage. These were both placed in the same unit so the magnitude of the signal of interest would be large relative to any external noise sources or added gain stages.

The configuration in Figure A.2 was chosen because it allowed a large number of poles and zeros in the loop transmission of the preamplifier which was necessary due the broad differences in the JFETs tested.

One parameter that varied significantly was the transconductance of the JFETs tested. At a drain current of 1mA the transconductance of the devices ranged from 26.3mS to 2.41mS. For a drain current of 100uA the transconductance ranged from 3.42mS to 0.458mS, and for drain current of 10uA the transconductance ranged from 378uS to 64.3uS. These broad ranges in transconductance made it necessary to change the magnitude of the loop transmission to compensate.

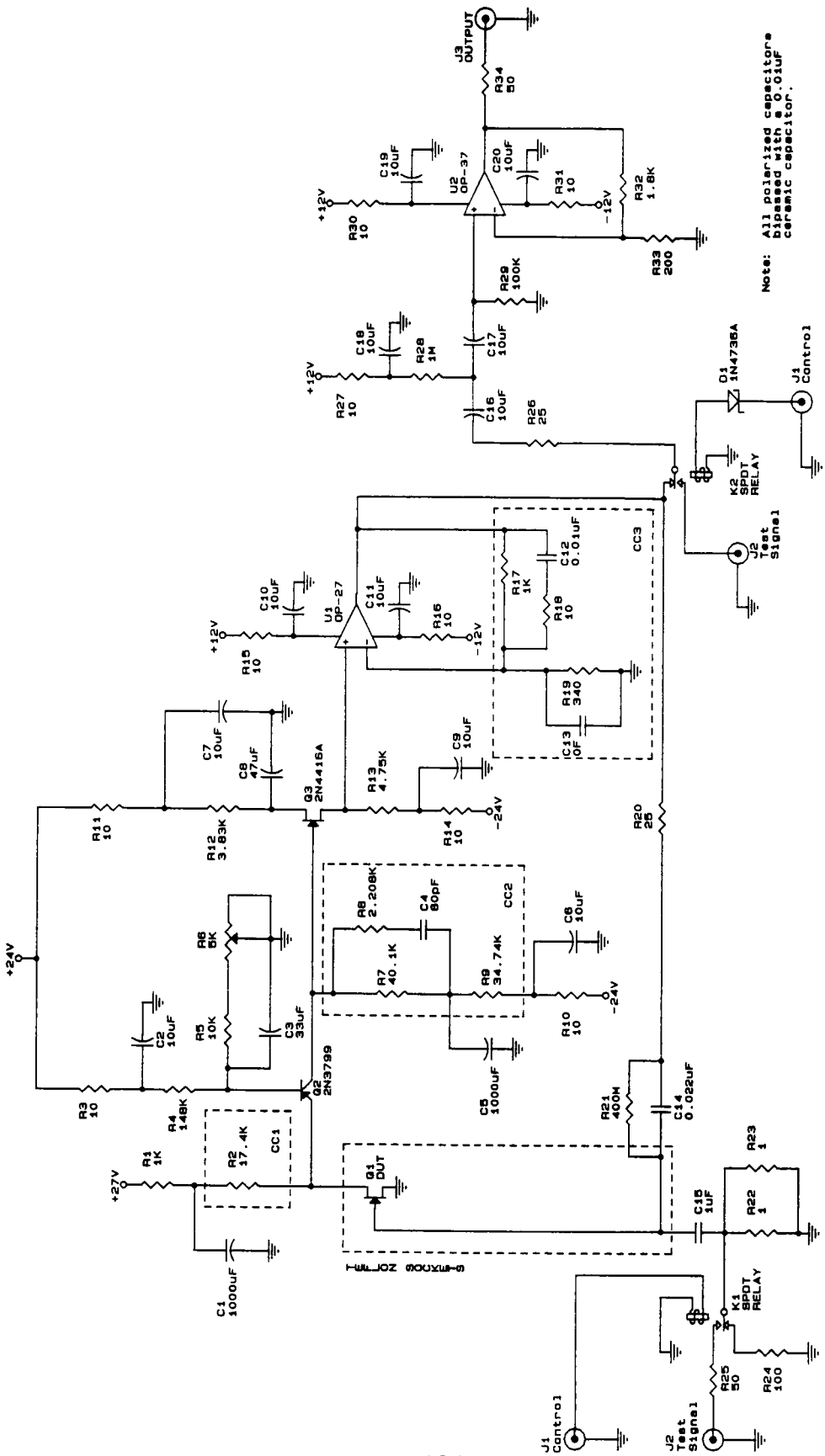


Figure A.2. Complete preamplifier schematic.

Another parameter that varied was the capacitance. The capacitance of the JFETs tested ranged from C_{ISS} = 330pF to C_{ISS} = 1.9pF. The broad range of capacitances required the poles and zeros of the loop transmission to be varied. Also the large value of capacitances of the devices measured made it necessary for the impedance "looking" into the emitter of Q2 to be small. This set a limit on the minimum collector current.

For all computer simulations that follow, the JFET of Figure A.2 was assumed ideal with a constant g_m of 23.4mS, a dc gate to source voltage of -1V, a C_{GS} of 246pF, and a C_{GD} of 145pF. These parameters are all similar to the NJ3600L device biased at a drain current of 1mA and a drain to source voltage of 2.5 volts. The computer simulations were performed by PSpice and a listing of the simulation file is shown at the end of this Appendix.

A.1.1 Characteristics

From a systems standpoint the preamplifier can be simplified as shown in Figure A.3. S_{FET} represents the series noise power of the JFET being tested. This generator is considered a signal generator (V_N) for the following gain calculations and it is assumed that Av approaches infinity.

The feedback network used allows an ac gain different from the dc gain. This was necessary because the JFET's had to be biased with the gate to source voltage in a range of 0 to -3V whereas an ac gain on the order of 50 was needed to amplify the noise of the JFET. R21 provides a unity dc gain between the output and the gate of the JFET.

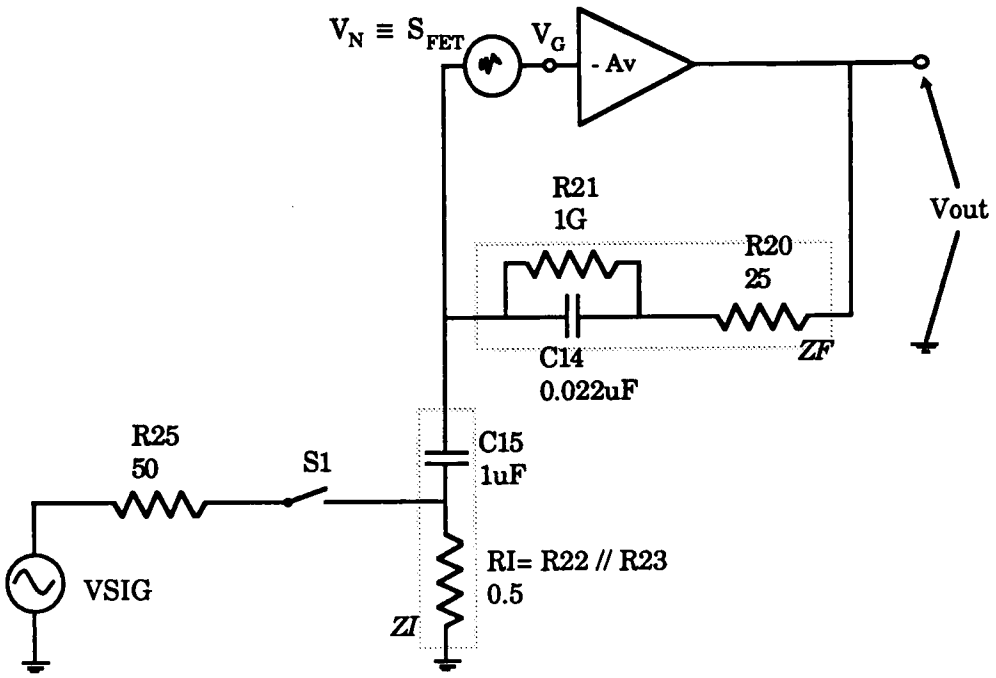


Figure A.3. Preamplifier system schematic.

The AC gain of the noise generator to the output (noise gain) can be expressed as

$$\frac{V_{out}}{V_N} = 1 + \frac{Z_F}{Z_I} \tag{A.1}$$

which in term of the component values is

$$\frac{V_{out}}{V_N} = 1 + \frac{C15}{C14}\left(\frac{1 + j\frac{f}{f_F}}{1 + j\frac{f}{f_I}}\right) \tag{A.2}$$

where

$$f_F = \frac{1}{2 \cdot \pi \cdot C14 \cdot R20}$$

$$f_I = \frac{1}{2 \cdot \pi \cdot C15 \cdot R_I}.$$

For $f << f_F$ or f_I the noise gain reduces to

$$\frac{V_{out}}{V_N} = 1 + \frac{C15}{C14}, \tag{A.3}$$

and is thus controlled by the capacitance values. As the frequency becomes greater than f_F and f_I the noise gain is determined by the feedback and feedforward resistors and equation A.2 simplifies to

$$\frac{V_{out}}{V_N} = 1 + \frac{R20}{R_I} \tag{A.4}$$

The noise gain was characterized by locating signal generator (VSIG) shown in Figure A.3. The optimum location would be to remove RI from ground and place the signal generator (VSIG') there. The signal gain for this case is

$$\frac{V_{out}}{VSIG'} = -\frac{Z_F}{Z_I} = \frac{C15}{C14}\left(\frac{1 + j\frac{f}{f_F}}{1 + j\frac{f}{f_I}}\right) \tag{A.5}$$

The noise gain could then be found by substituting equation A.5 into A.1 which yields

$$\frac{V_{out}}{V_N} = 1 - \frac{V_{out}}{VSIG'} \tag{A.6}$$

Unfortunately, the signal generator could not be placed at this location due to the change that occurred in bias points when VSIG' was switched in and out. This was a problem because the bias of the circuit took a long time to recover due to the long time-constant of the feedback network.

The location shown in Figure A.3 was chosen as an alternative location and provided stability for the bias points when the signal generator was added. The signal gain for this location can be expressed as

$$\frac{V_{out}}{VSIG} = - ATTEN \cdot \left(\frac{Z_F}{Z_I}\right) \cdot ERR \tag{A.7}$$

where

$$ATTEN = \frac{R_I}{R_I + R25}$$

$$ERR = \left(\frac{1 + j\frac{f}{f_1}}{1 + j\frac{f}{f_F}}\right)\left(1 + \frac{C14}{C15}\right)\left(\frac{1 + j\frac{f}{f_1}}{j\frac{f}{f_2}}\right)$$

$$f_1 = \frac{1}{2 \cdot \pi \, (R_I + R20)\left(\frac{C14 \cdot C15}{C14 + C15}\right)}$$

$$f_2 = \frac{1}{2 \cdot \pi \cdot R_I \cdot C15} .$$

Equation A.7 is the same as equation A.5 except for an attenuation coefficient (ATTEN) and an error term (ERR). The error term is not significant for the circuit of Figure A.2 in the frequency range used. and the magnitude of error due to the location of VSIG is discussed later in the system considerations section. The noise gain can be expressed by substituting equation A.7 (ERR = 1) in to equation A.1 which yields

$$\frac{V_{out}}{V_N} = 1 - \frac{1}{ATTEN}\left(\frac{V_{out}}{VSIG}\right). \qquad (A.8)$$

A.1.1.1 DC

All JFET's were tested at a drain to source voltage of 2.5V which was adjusted by potentiometer R6 in Figure A.2. The drain current was also set by this voltage, the value of R1+R2, and the collector current of Q2 which is relatively constant. R2 was placed in a component carrier so that it could be easily changed for different values of drain current.. The values of drain current used in the noise measurements presented were 1mA, 100uA, and 10uA. Adjusting the drain voltage to set the drain current worked well for the 1mA and 100uA levels but at 10uA, the bias current of Q2 (~300uA) varied too much from device to device for this method to be accurate. Thus, the current was sampled by placing a known value of resistance in series with the drain of the JFET and then R6 was adjusted until a drain current of 10uA was obtained.

The network formed by C16 and C17 was used to decouple DC signals from the next stage and also allows for bi-polar signals.

A.1.1.2 AC

The preamplifier section of Figure A.2 can be simplified for midband frequencies as shown in Figure A.4. The simplified circuit shown in Figure A.4 was used for all calculations presented, and the complete preamplifier of Figure A.2 was used for all simulation results presented.

The loop transmission of the preamp is shown in Figure A.5. As shown in this Figure the phase margin for this configuration is 80.64 degrees.

The magnitude of the noise gain from equation A.8 can be expressed as

$$\left|\frac{V_{out}}{V_N}\right| = 1 + \frac{1}{ATTEN}\left|\frac{V_{out}}{VSIG}\right| . \qquad (A.9)$$

This is shown in Figure A.6 where

$$\frac{1}{ATTEN} = 101$$
$$V_{out} = V(100)$$
$$VSIG = V(21) .$$

From Figure A.6 it can be seen the 3dB point occurs at 1.68MHz.

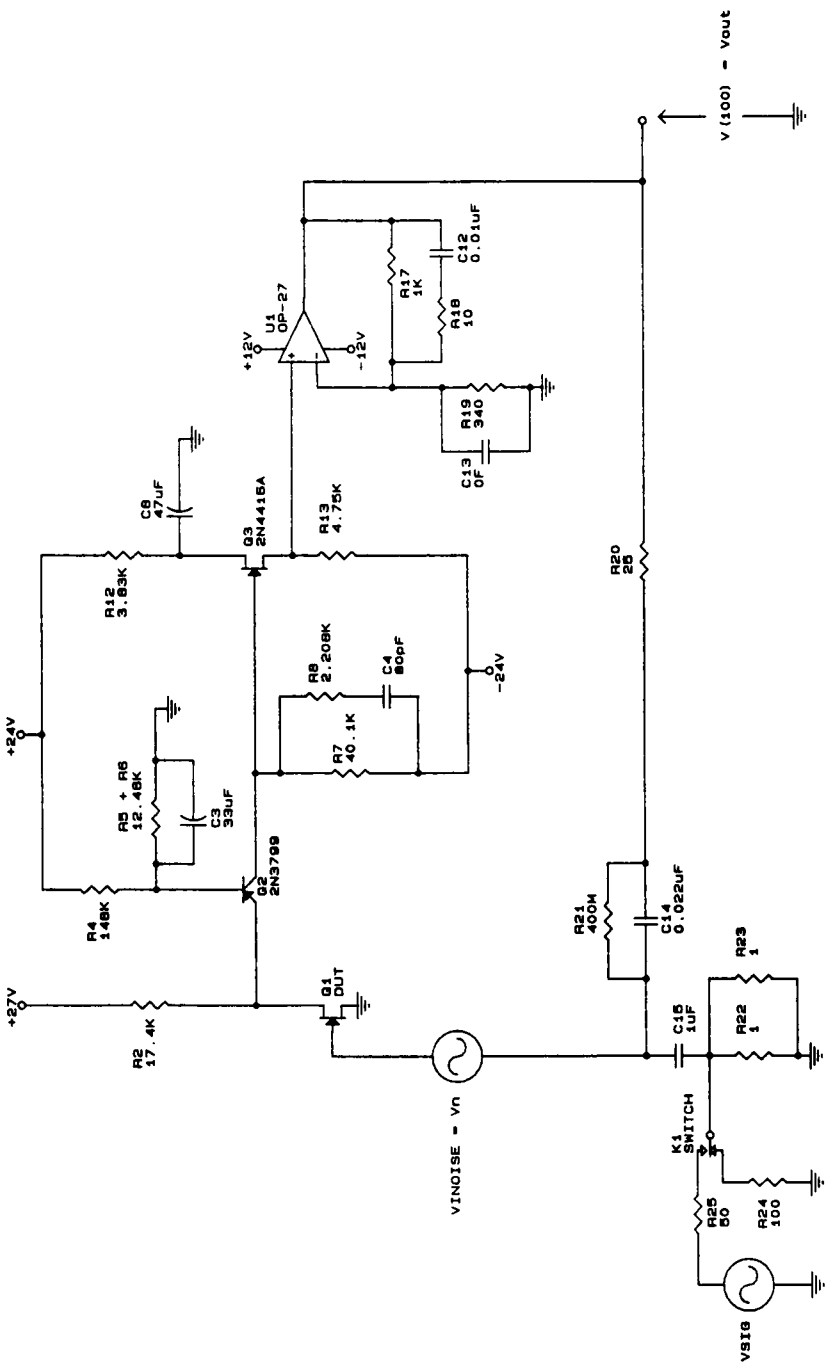


Figure A.4. Simplified preamplifier schematic.

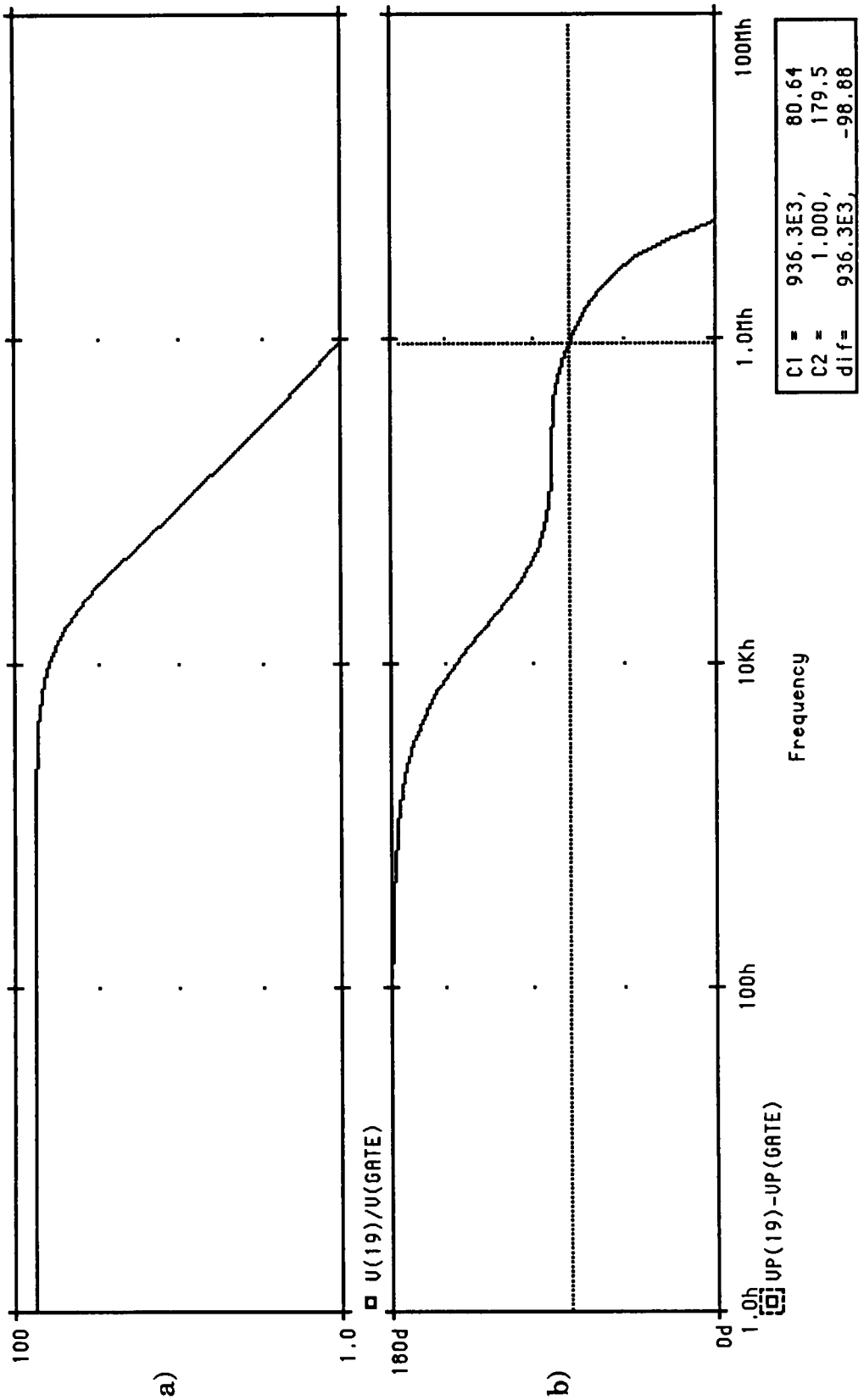


Figure A.5. Loop transmission versus frequency a) Magnitude b) Phase.

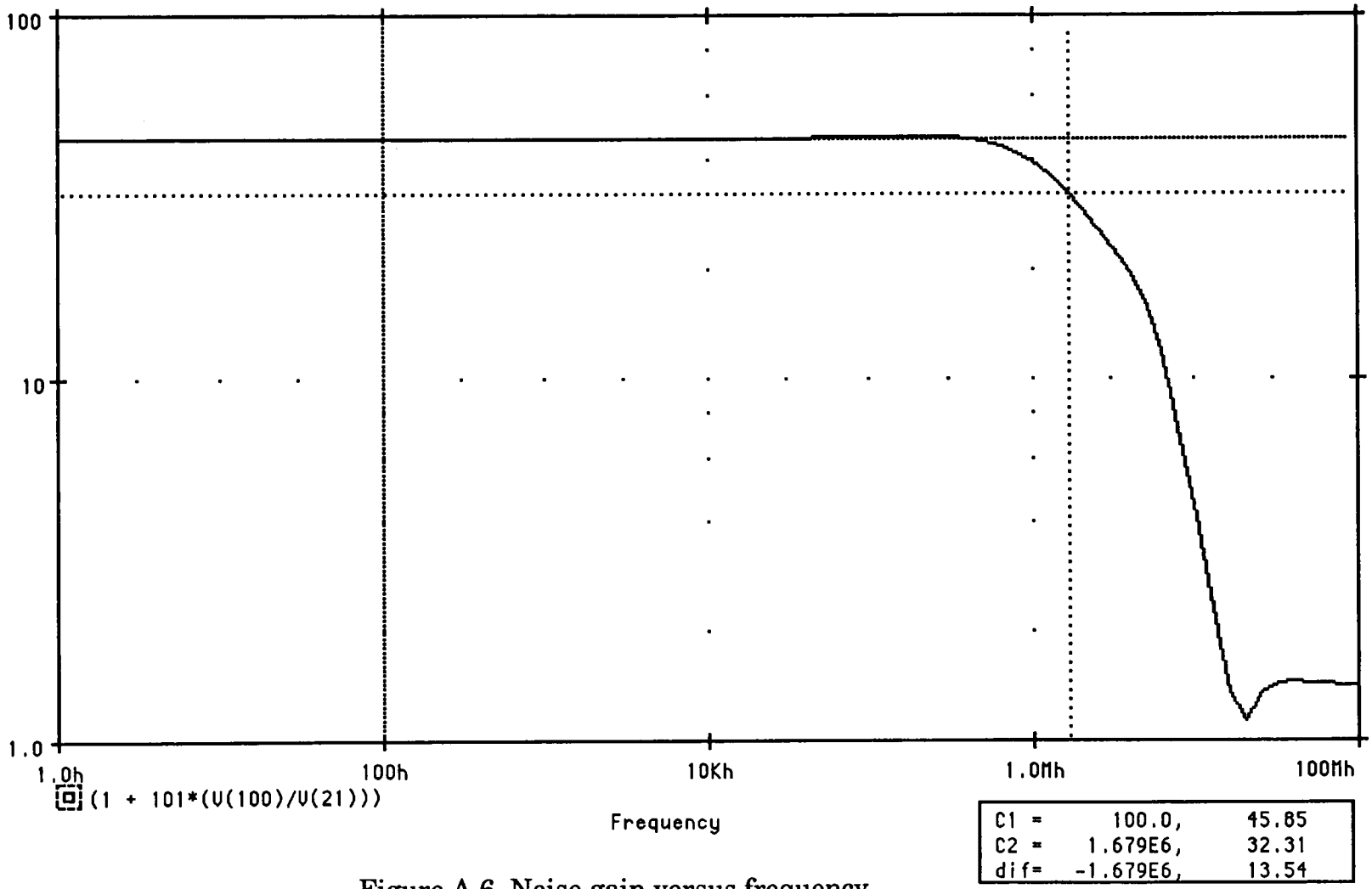


Figure A.6. Noise gain versus frequency.

A.1.1.3 Noise

For the preamp of Figure A.4 the noise at midband frequencies can be expressed as

$$R_n = \underbrace{\frac{1}{R2 \cdot gm^2}}_{\text{R2 component}} + \underbrace{\frac{2 \cdot q}{4 \cdot K \cdot T}\left(I_B + \frac{I_C}{Beta^2}\right)\left(\frac{1}{gm^2}\right)}_{\text{Q2 component}} + \underbrace{\frac{1}{R7}\left[\frac{1}{gm}\left(1 + \frac{r_e}{R2}\right)\right]^2}_{\text{R7 component}}$$

$$+ \underbrace{R_I\left(\frac{C15}{C14 + C15}\right)^2}_{R_I \text{ component}} + \underbrace{R20\left(\frac{C14}{C14 + C15}\right)^2}_{\text{R20 component}} \qquad \text{(A.10)}$$

where only the dominate noise elements have been shown. Using the dc bias point information from the PSpice simulation

$$Beta = 505$$

$$I_C = 306\mu A$$

$$I_B = \frac{I_C}{Beta} = -.606\mu A$$

$$r_e = \frac{V_T}{I_C} = 85\Omega$$

$$gm = 23.2mS$$

and applying these values and the component values shown in Figure A.4 to equation A.10 yields

$$R_n = \underbrace{0.17}_{\text{R2 component}} + \underbrace{0.0218}_{\text{Q2 component}} + \underbrace{0.0468}_{\text{R7 component}} + \underbrace{0.479}_{R_I \text{ component}} + \underbrace{0.0116}_{\text{R20 component}}$$

$$= 0.666\Omega \ . \qquad \text{(A.11)}$$

The result in equation A.11 compares well to the results obtained in the simulation of the complete preamplifier as shown in Figure A.7. The value of the midband noise resistance from this simulation is 0.6702 ohms.

A.1.1.4 Power Supply Noise

A nuclear instrumentation module bin (NIMBIN) was used to supply the +/- 24 and the +/- 12 voltages. The drain node was very sensitive to noise injected from the supply so a regulated battery system was used to supply 27 volts and was also filtered by R1 and C1. The base of Q2 is also sensitive to power supply noise but was not difficult to filter due to the large impedances used. The node formed by R9 and R7 was also critical and the combination of C5 and R9 was used to filter the bias for this node that supplyed from the -24V supply.

Sixty-cycle (60 Hz) pickup from external sources and ground loops in the system posed quite a problem for the most sensitive noise measurements. The circuit was placed in a steel box and the box was connected to the circuit ground near the output. Special consideration had to be made for location of any external instruments that generated significant magnetic fields, which were easily coupled into the system.

A.1.2 Physical Considerations

The broad range of JFET's tested was accommodated by the use of component carriers (CC) used for the compensation networks in the

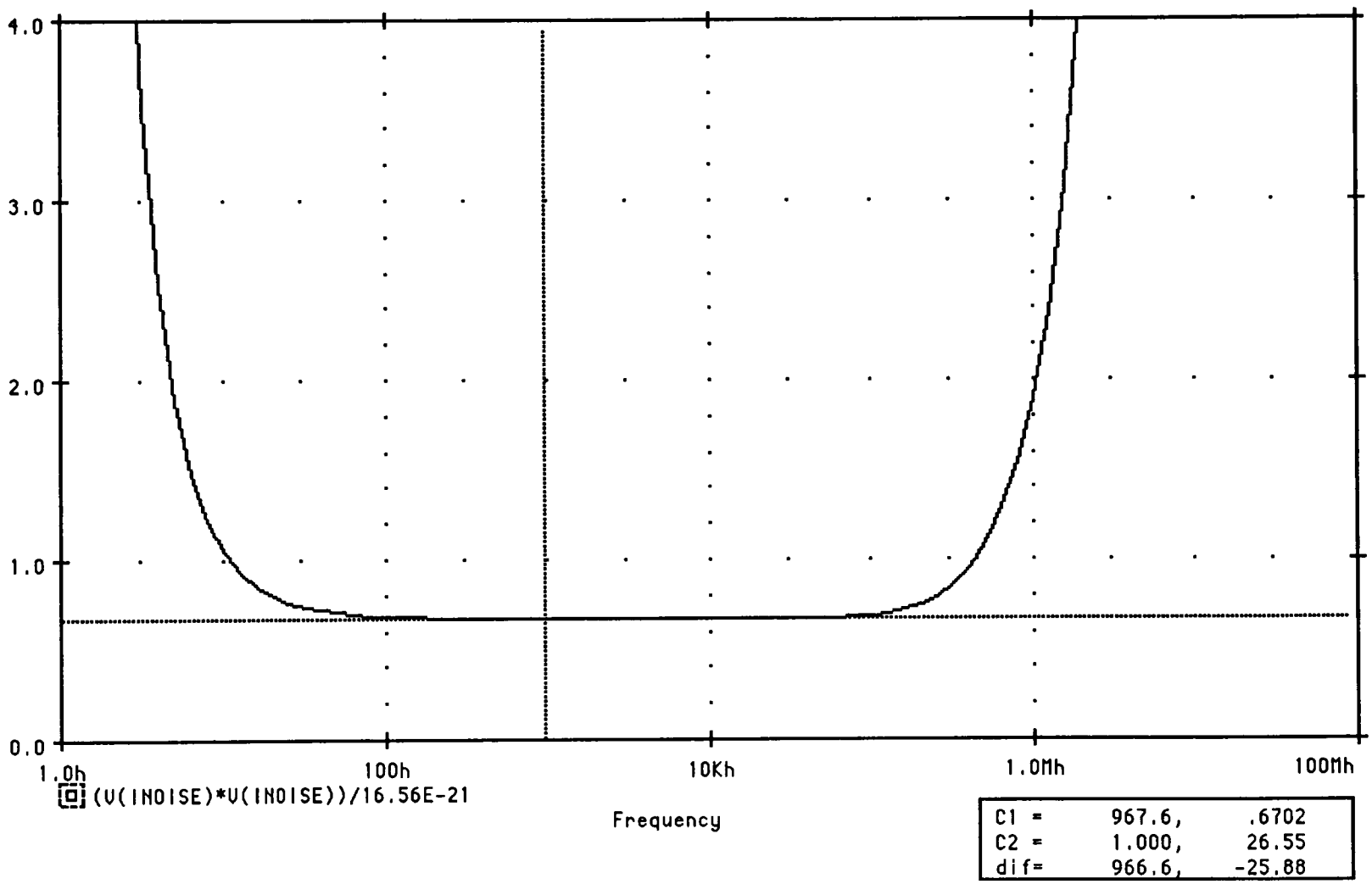


Figure A.7. Noise resistance (Rn) vs frequency.

preamplifier. R2 was placed in one carrier (CC1) and was used to set the desired drain current. R7, R8, R9, and C4 were placed together in another carrier (CC2) and set the collector current for Q2 and also provided a pole-zero network. R17, R18, R19, C12, and C13 were grouped together in a component carrier (CC3), and set the gain of the operational amplifier while providing another pole-zero network with a compensation pole (C13 and R19) for the op-amps loop transmission. The op amp was selected based on the frequency and noise requirements of the measurement. A list of the networks and their values is shown in the tables A.1 through A.6.

Table A.1. CC1 values.

Carrier #	R2	I_D
1	17.4K	1mA
2	58.5K	100uA
3	59.7K	100uA
4	114K	10uA

Table A.2. CC2 values.

Carrier #	R7	R8	R9	C4	$I_C(Q_2)$
1	40.1K	2.21K	34.7K	80pF	306uA
2	73.0K	8.23K	1.83K	20pF	312uA
3	100.4K	0	15.4K	*	203uA

* Note: C4 varies with the device being tested and is displayed in Table A.6.

Table A.3. CC3 values.

Carrier #	R17	R18	R19	C12	C13
1	1.00K	10.0	340	0.01uF	0pF
2	16.2K	162	499	680pF	0pF
3	64.0K	0	200	26nF	0pF
4	100K	2.00K	200	15.7nF	0pF

Table A.4. Set-up for I_D = 1mA.

Part	CC1	CC2	CC3	U1 OP-AMP	K2
NJ3600L	1	1	1	OP-27	55
NJ903L	↓	1	↓	↓	55
NJ1800DL	↓	1	↓	↓	55
2N6451	↓	2	↓	↓	55
2SK152A	↓	2	↓	↓	10
2N4858	↓	2	↓	↓	10
2N4416A	↓	2	2	OP-37	10
IMF5912	↓	1	2	OP-37	10

Table A.5. Set-up for I_D = 100uA.

Part	CC1	CC2	CC3	U1 OP-AMP	K2
NJ3600L	2	1	1	OP-27	55
NJ903L	↓	1	↓	↓	55
NJ1800DL	↓	1	↓	↓	55
2N6451	↓	1	↓	↓	55
2SK152A	↓	2	↓	↓	10
2N4858	↓	2	↓	↓	10
2N4416A	3	2	↓	↓	10
IMF5912	3	2	↓	↓	10

Table A.6. Set-up for I_D = 10uA.

Part	CC1	CC2	C4	CC3	U1 OP-AMP	K2
NJ3600L	4	3	33pF	3	HA-2541	55
NJ903L	↓	↓	10pF	↓	↓	↓
NJ1800DL	↓	↓	10pF	↓	↓	↓
2N6451	↓	↓	25pF	↓	↓	↓
2SK152A	↓	↓	10pF	↓	↓	↓
2N4858	↓	↓	10pF	↓	↓	↓
2N4416A	↓	↓	39pF	4	HA-2540	10
IMF5912	↓	↓	18pF	4	HA-2540	10

The components of the feedback network changed for both the value of I_D and the increase in gate leakage current after exposure to radiation. R21 was 400M for pre-radiation testing and was changed to 44.4M for post-radiation testing due to the increase in gate leakage current. For I_D = 1mA the following values were used

R20 = 25
C14 = 0.022uF
R_I = 0.5
C15 = 1uF .

For I_D = 100uA

R20 = 6
C14 = 0.0833uF
R_I = 0.5
C15 = 1uF .

For I_D = 10uA

R20 = 25
C14 = 200nF
R_I = 4.976
C15 = 1uF .

A.2 Gain Stages

The first gain stage is shown in Figure A.2 and provided a gain of 10. A Precision Monolithics OP-37 was used in this stage.

The next gain stage was external to the preamplifier and provided gains of both 10 and 55, the value of which was set based on the magnitude of noise generated by the JFET being tested. This amplifier is shown in Figure A.8. This stage used the HA-2536 which has a very high gain-bandwidth product (600MHz) making it sensitive to layout. Thus the gain stage in Figure A.8 was built on a copperclad protoboard and placed in a steel box.

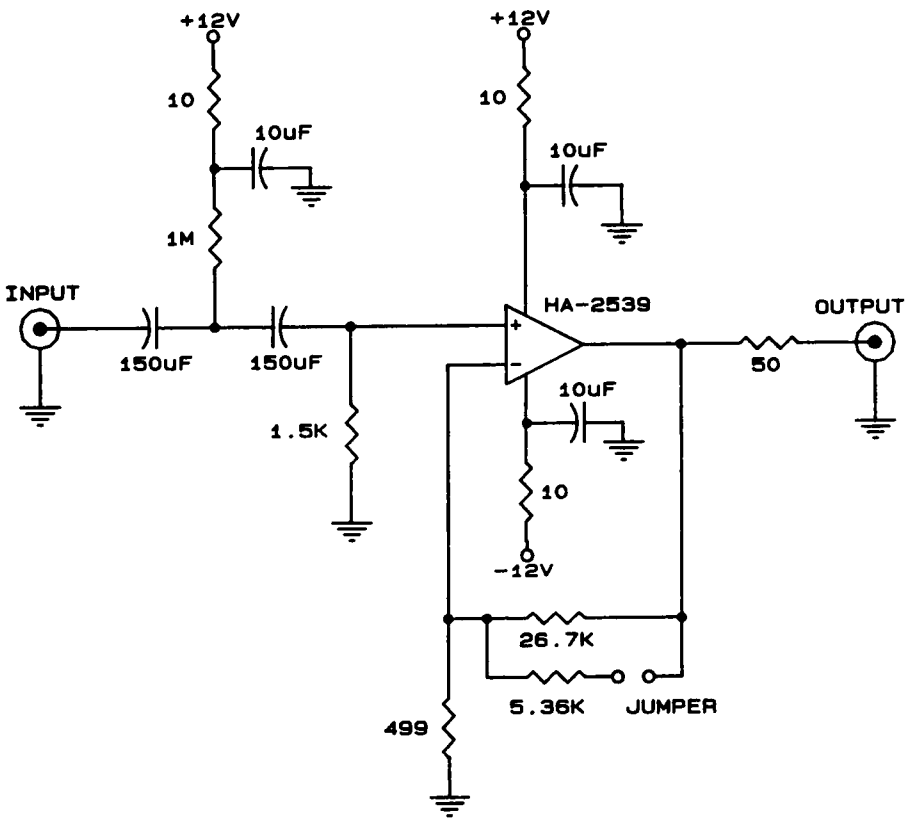


Figure A.8. K2 Gain stage.

A.3 Filter System

The filter system used in these measurements was an amplifier with Twin-T network [14]. This amplifier provided a bandpass characteristic about a center frequency f_o, where the noise bandwidth could be approximated by equation A.12 [14].

$$\Delta f_N = \frac{2 \cdot \pi \cdot f_0}{A} \tag{A.12}$$

where A is the closed loop gain of the Twin-T filter. Table A.7 is a listing of the characteristics of the filters used.

Table A.7. Twin-T filter parameters.

f_0	A	$\sqrt{\Delta f_N}$
10.44	39.08	1.30
21.07	37.31	1.88
46.17	38.76	2.74
100.25	38.31	4.05
212.25	39.68	5.80
463.23	36.90	8.88
1,009.40	40.05	12.58
2,125.00	39.26	18.44
5,035.50	38.31	28.74
10,140.00	39.84	39.99
20,688.00	38.31	58.25
47,121.00	38.31	87.91
100,947.00	37.74	129.65
210,880.00	38.61	185.25
462,990.00	36.63	281.81

A.4 Data Acquisition

The output of the Twin-T filter system was measured using the HP3400A true RMS Voltmeter. This meter provides an output dc level which corresponds to the front panel scale. This dc level was acquired using a HP3478A multimeter and the result read and converted with an IBM PC having a HPIB bus controller. Thus, all measurements were averaged and logged on a personal computer.

A.5 System Overview

The system defined in Figure A.1 is shown in terms of its gain in Figure A.9.

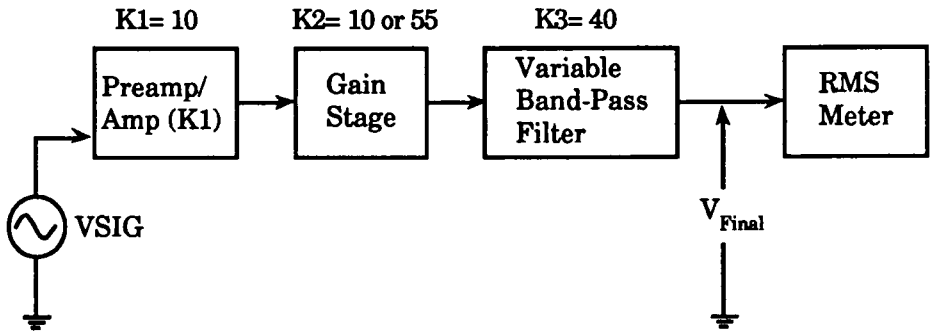


Figure A.9. Noise measurement system gain diagram.

From Figure A.9, Figure A.2 and the analysis system analysis presented in the preamp section, the magnitude of the true noise gain can be expressed as

$$NG^{ACT} = \frac{V(100)}{VINOISE} K1 \cdot K2 \cdot K3 \ . \tag{A.13}$$

The magnitude of the noise gain as measured by applying the test signal generator (VSIG) is

$$NG^{MEAS} = \left(1 + \frac{1}{ATTEN} \frac{V(100)}{VSIG}\right) K1 \cdot K2 \cdot K3 \ . \tag{A.14}$$

The series noise resistance measured can then be expressed as

$$R_n = \frac{1}{4 \cdot K \cdot T} \left(\frac{V_{final}}{\Delta f_n} \frac{1}{NG}\right)^2 = const \left(\frac{1}{NG}\right)^2 . \tag{A.15}$$

The error in the measurement of the noise resistance due to the location of the test signal source is

$$\%Error = \frac{R_n^{ACT} - R_n^{MEAS}}{R_n^{ACT}} \cdot 100 = \frac{\left(\frac{1}{NG^{ACT}}\right)^2 - \left(\frac{1}{NG^{MEAS}}\right)^2}{\left(\frac{1}{NG^{ACT}}\right)^2} \cdot 100 \ . \tag{A.16}$$

A plot of this error as a function of frequency was produced using a PSpice simulation of the preamp of Figure A.2 and is shown in Figure A.10.

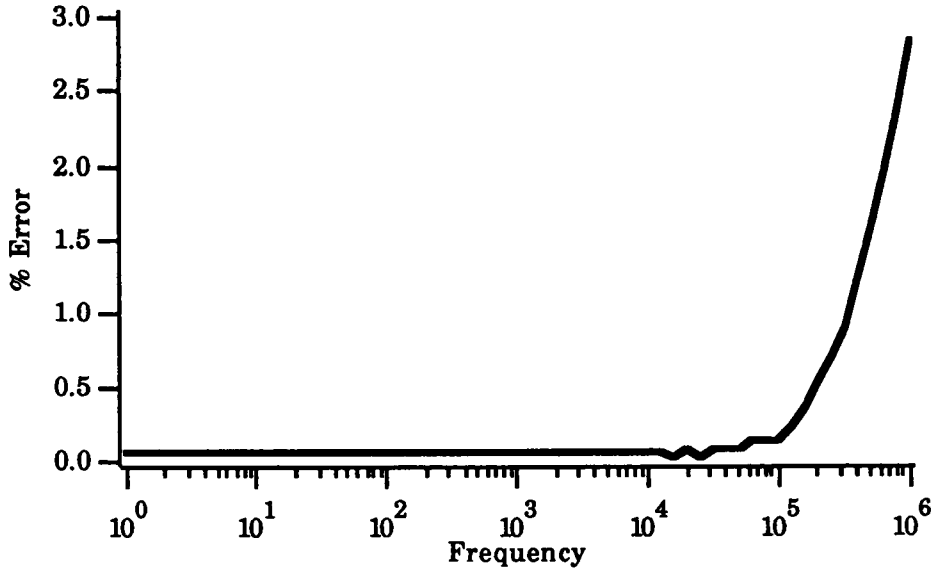


Figure A.10. Error in noise resistance measurement due to signal location.

It can be seen that this error is not significant for the frequency range of the data presented.

A.6 PSpice Simulation File

The PSpice simulation file for the preamplifier presented in Figure A.2 follows.

```
* Fet Noise Ckt. (NM1.CIR)

* Parameter Definitions *
.PARAM VDC=-1, ID=1m, GM= 23.2m, CGD= 145P, CGS= 246P
```

```
* Voltage Sources *
VPLUS VCC 0 24V
VMINUS VEE 0 -24V
VAMPP VAP 0 12V
VAMPM VAM 0 -12V
VBATT VBAT 0 27.01V

* Signal Sources *
 *--NOISE SIGNAL
 R24 20 0 100
 VINOISE GATE 19 AC 1
 *--TEST SIGNAL
 *R25 21 20 50
 *VINOISE GATE 19
 *VSIG 21 0 AC 1

* Feedback *
R20 100 18 25
R21 18 19 1G
R22 20 0 1
R23 20 0 1
C14 18 19 0.022uF
C15 19 20 1uF

* Resistors *
R1 VBAT 1 1K
R2 1 DRAIN 17.4K
R3 VCC 2 10
R4 2 3 148K
R5 3 4 10K
R6 4 0 2.484K
R7 5 7 40.1K
R8 5 6 2.208K
R9 7 8 34.74K
R10 8 VEE 10
R11 VCC 9 10
R12 9 10 3.83K
R13 11 12 4.75K
R14 12 VEE 10
R15 VAP 13 10
R16 14 VAM 10
R17 15 100 1K
R18 15 17 10
R19 15 0 340
R26 100 22 25
R27 VAP 24 10
R28 24 23 1MEG
```

```
R29 25 0 1OOK

* Capacitors *
C1 1 0 1000uF
C2 2 0 10uF
C3 3 0 33uF
C4 6 7 80pF
C5 7 0 1000uF
C6 8 0 10uF
C7 9 0 10uF
C8 10 0 47uF
C9 12 0 10uF
C10 13 0 10uF
C11 14 0 10uF
C12 17 100 0.01uF
*C13 15 0
C16 22 23 10uF
C17 23 25 10uF
C18 24 0 10uF

* Noiseless FET *
XFET DRAIN 0 GATE IDEAL_FET

* Operational Amplifier
XAMP 15 11 VAM 100 VAP OP-27

* Transistors *
Q2 5 3 DRAIN Q2N3799
J3 10 5 11 J2N4416A

* Simulation Cards *

*[DC Analysis]
*.OP

*[Noise Table]
*.AC LIN 3 100 1K
*.NOISE V(100) VINOISE 2

*[AC Analysis]
.AC DEC 10 1 100MEG
.PROBE

*[Noise analysis]
.NOISE V(100) VINOISE
```

```
* Models *
.model Q2N3799  PNP(Is=6.734f Xti=3 Eg=1.11 Vaf=45.7 Bf=478.3 Ne=1.841
+          Ise=6.734f Ikf=.2117 Xtb=1.5 Br=2.619 Nc=2 Isc=0 Ikr=0 Rc=1.67
+          Cjc=6.2p Mjc=.301 Vjc=.75 Fc=.5 Cje=7.5p Mje=.2861 Vje=.75
+          Tr=9.778n Tf=569.5p Itf=.17 Vtf=5 Xtf=8 Af=1 Kf=16.15e-18 Rb=300)
*          National  pid=62          case=TO18

.model J2N4416A NJF(Beta=989.4u Betatce=-.5 Rd=1 Rs=1 Lambda=5.5m
+              Vto=-3.06 Vtotc=-2.5m Is=33.57f Isr=322.4f N=1 Nr=2 Xti=3
+              Alpha=311.7 Vk=243.6 Cgd=1.6p M=.3622 Pb=1 Fc=.5
+              Cgs=2.414p Kf=7.445E-18 Af=1)
*              88-08-01 rmn        BVmin=35

.SUBCKT IDEAL_FET DRAIN SOURCE GATE

* SIMPLE FET MODEL
*
*   Characteristics: no noise, constant gm, dc offset on input

VOFF GATE G1 {VDC - (ID/GM)}
C_GS G1 SOURCE {CGS}
C_GD G1 DRAIN {CGD}
G_GMV DRAIN SOURCE VALUE= {(V(G1) - V(SOURCE)) * GM}
.ENDS IDEAL_FET

.SUBCKT OP-27   2   3   4   6   7
*         -IN  +IN  VEE  OUT  VCC
* DEVICE CHAR:  AOL=1.5E6, ZIN=4MEG// 8PF, IB= 15NA, IOS=12NA,
*                       RCM=2E9, RO=70, GB=8MHZ,SR=2.8V/US, VOS=30UV,
*                        CMRR=120DB,PSRR=2UV/V, VINCM=+-12.5V,
*                        VO=+-13.5V, IO(LIMIT)= +35MA,-42MA; POLES AT
*                       5.3HZ;0.8,12,20,30 MHZ; ZEROES AT 0.9,6.5 MHZ.
*                        EN=3NV/RTHZ. IN=0.4PA/RTHZ, FB(IN)=140 HZ.
*                      LAST NODE=31
*
VOS 2 23 30U
ECMRR 23 24 POLY(2) 22 0 3 0 0 0.5U 0.5U
EPSRR 24 22 POLY(2) 7 0 4 0 60U -2U 2U
IOSI 0 2 479NA
RCMI 2 0 4000MEG
CIN 2 3 8PF
RCMN 3 0 4000MEG
IOSN 0 3 491NA
VP 11 0 42.6
R1 11 5 3.36K
R2 11 10 3.36K
CC 5 25 25.94PF
```

```
RZ1 25 10 943.2
Q1 5 22 1 N1
Q2 10 3 9 N1
RE1 1 8 109
RE2 8 9 109
ICS 8 14 17.94MA
VN 0 14 15
D1 12 8 DA
R3 12 13 100
V1 13 14 1.4
G1 0 15 5 10 10M
R4 15 0 5MEG
D2 15 17 DB
D3 17 15 DB
E1 17 0 16 0 1
R5 15 16 50
C1 16 0 5.963NF
E3 26 0 16 0 1
RA1 26 27 1.325K
CA1 27 0 10PF
E4 28 0 27 0 1
RA2 28 29 795
CA2 29 0 10PF
E5 30 0 29 0 33.33
RA3 30 31 3.233K
CA3 30 31 54.64PF
RA4 31 0 100
G2 0 18 31 0 0.02
R6 18 0 50
D4 18 19 DA
D5 19 18 DC
E2 19 0 6 0 1
R7 18 6 20
D6 6 20 DA
D7 21 6 DA
V3 7 20 2.2
RPS 7 4 26K
IPS 7 4 1.9MA
V2 21 4 2.2
.MODEL DA D(IS=5.73E-14)
.MODEL DB D(IS=1.47E-16)
.MODEL DC D(IS=3.07E-16)
.MODEL N1 NPN(IS=1FA BF=1.79E4 RB=150 KF=4.5E-17)
*
.ENDS OP-27

.END
```

APPENDIX B

DEVICES TESTED

Table B.1 is a list of the n-channel JFET devices tested.

Table B.1. N-channel JFET devices tested.

Part	Total Units	Manufactuer
NJ3600L	4	InterFET
NJ903L	2	InterFET
NJ1800DL	4	InterFET
2N6451	4	InterFET
2SK152A	4	Sony
2N4858	2	InterFET
2N4416A	4	Siliconix
IMF5912	4	Intersil
2N5432	4	Intersil

Table B.2 is a listing of the bipolar devices tested.

Table B.2. Bipolar devices tested.

Part	Total Units	Manufactuer
NPN		
MPSH10	3	Motorola
A401	2	Amperex
CA3127	2	RCA
MRF951	1	Motorola
TLN1	5	VTC
T6NW	5	VTC
PNP		
MPSH81	3	Motorola
A441	2	Amperex
TVPA35	5	VTC

VITA

Ronald Bryce Gray III, was born in Fort Lauderdale, Florida on January 26, 1965. He attended secondary schools in Fort Lauderdale and graduated from Nova High School in June, 1983. The following September, he attended Taylor University in Upland, Indiana. In January, 1985 he transferred to The University of Tennessee in Knoxville, Tennessee where in June, 1988 he received the Bachelor of Science degree in Electrical Engineering. The following August he began study toward a Master's degree.

Mr. Gray will be employed by Battelle of Columbus, Ohio after graduation.